Film Formation and Thermal Transitions of Polymers Studied by Atomic Force Microscopy

By

Martina Meincken

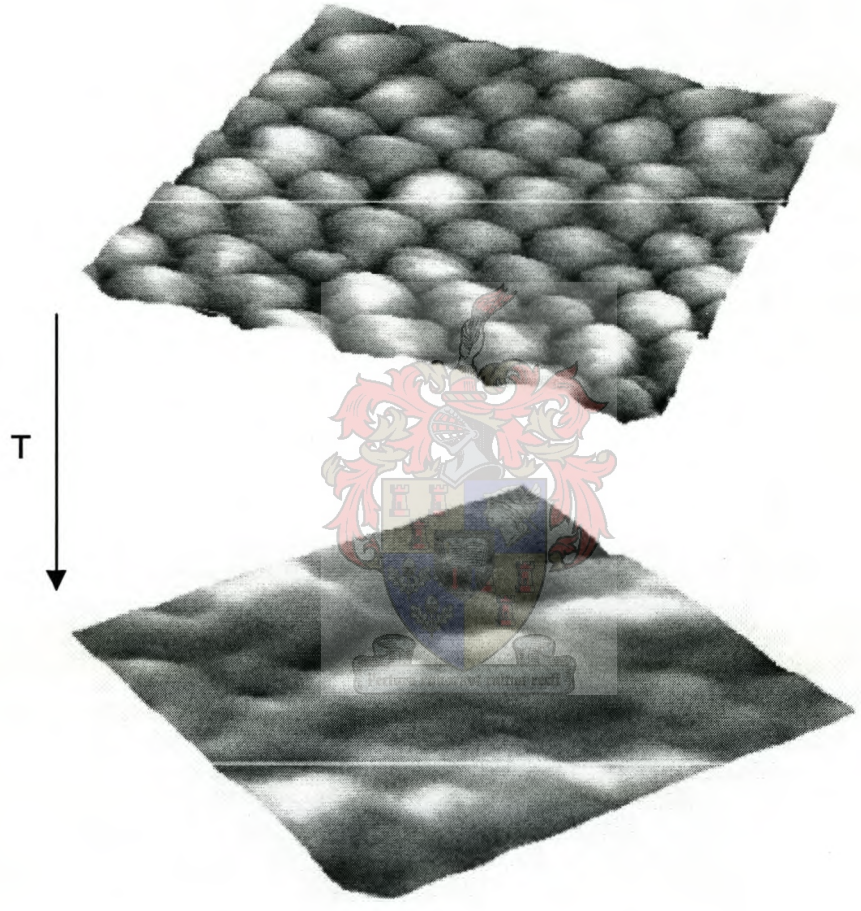

Dissertation presented for the degree of

Doctor of Philosophy (Polymer Science)

at the
University of Stellenbosch

Promoter: R.D. Sanderson

March 2002

I, the undersigned, hereby declare that the work contained in this dissertation is my own original work and that I have not previously in its entirety or in part submitted it at any university for a degree.

Signature: Date:

CHAPTER 1: Abstract

The kinetics of drying and film formation of different polymeric latices were studied. Various theoretical models predict a strong dependency of the film formation characteristics on the particle size and morphology. This could be confirmed by experimental studies.
The influence of particle size and morphology of differently structured latices on the film formation process was investigated by Atomic Force Microscopy (AFM) and Ultrasonic shear wave reflection. These two methods allow a comprehensive characterization of the drying and film formation process of emulsions. The studies confirmed the theoretical model, that the film formation behavior is influenced by the particle size and particle morphology.
Furthermore the influence of different additives, such as coalescent solvents and rheology modifiers on the film formation behavior was investigated.

As a second part of the studies, a novel technique was developed to measure thermal transitions of polymers with the AFM in the non-contact mode, using it as a Dynamic Mechanical Analyzer (DMA) on a local scale. The resonance frequency of the AFM cantilever was measured as a function of the temperature and thermal transitions of a polymer were clearly visible as changes in the resonance frequency / temperature response curve. Using the AFM in this mode allows the determination of the thermal properties of a material at a specific position on a sample, thereof on a macromolecular scale. A simple model was developed to explain the response of the cantilever caused by the transitions in the polymer and the related form of the frequency/temperature curves.
This new technique adds a new dimension to standard thermal analysis techniques. It is now possible to resolve the individual thermal transitions of different polymer phases, for example in structured multiphase polymers.

Opsomming

Die kinetika van droging en filmvorming van verskeie polimeriese lateksverbindingse is ondersoek. Verskeie teoretiese modelle voorspel 'n sterk afhanklikheid tussen die filmvormingseienskappe, partikelgrootte en morfologie. Hierdie afhanklikhede is eksperimenteel bevestig. Die invloed van partikelgrootte en morfologie van verskillende lateksstrukture op die filmvormingsproses is deur atoominteraksiemikroskopie (Eng: Atomic Force Microscopy, AFM) sowel as ultrasoniese skuifweerstandgolfrefleksie ondersoek. Hierdie twee metodes bied 'n deurslaggewende karakterisering van die droging en filmvormingsproses van emulsies. Resultate bevestig die teoretiese model, nl. dat filmvorming deur partikelgrootte en morfologie beïnvloed word.
Die invloed van verskillende bymiddels, insluitend reologie-modifiseerders op filmvorming, is ook ondersoek.

Vervolgens is 'n nuwe tegniek ondersoek om die termiese oorgange van polimere met behulp van die AFM in nie-kontak modus (deur dit as 'n dinamiese meganiese analiseerder (DMA) te gebruik) te bestudeer. Die resonansie-frekwensie van die AFM-hefboom is bepaal as 'n funksie van temperatuur. Termiese oorgange van 'n

polimeer is duidelik waarneembaar as veranderinge in die resonans-frekwensie/temperatuur responskurwe. Deur gebruik te maak van die AFM in hierdie modus kan die termiese eienskappe van 'n materiaal by 'n spesifieke posisie op die monster op molekulêre skaal bepaal word. 'n Eenvoudige model is ontwikkel om die oorgange in die polimeer, en gevolglik die vorm van die frekwensie/temperatuur kurwes, dmv. die respons van die hefboom, te verduidelik

Hierdie nuwe tegniek gee 'n nuwe dimensie tot die standaard tegnieke van termiese analise tegnieke. Dit is nou moontlik om individuele termiese oorgange van verskeie polimeerfases, byvoorbeeld in gestruktureerde multifase polimere, te ondersoek en op te los

TABLE OF CONTENTS:

LIST OF FIGURES:

LIST OF TABLES:

Abbreviations:

AFM	Atomic Force Microscope
BA	Butyl Acrylate
CS	Core Shell
DMA	Dynamic Mechanical Analysis
DSC	Differential Scanning Calorimetry
EGDMA	Ethylene glycol dimethacrylate
EGMBEBE	Ethylenglycol monobutylether 2 butoxyethanol
ESEM	Environmental Scanning Electron Microscope
FCC	Face Center Cubical
HASE	Hydrophobically Modified Alkali Soluable
MAA	Methacrylic Acid
MMA	Methyl Methacrylate
MFT	Minimum Film-Formation Temperature
μTA	Micro Thermal Analysis
M_W	Molecular Weight
PCS	Particle Correlation Spectroscopy
PE	Polyethylene
RFM	Resonance Frequency Measurement
RF	Resonance Frequency
S	Styrene
SDS	Sodium Dodecyl Sulfonate
SEM	Scanning Electron Microscope
SPM	Scanning Probe Microscopy
STM	Scanning Tunneling Microscope
SThM	Scanning Thermal Microscope
T_g	Glass Transition Temperature
T_m	Melting Temperature
UL	Unstructured Latex
US	Ultrasonic
WLF	Williams-Landel-Ferry

Units:

nm	Nanometer (10^{-9}m)
Å	Angstrom (10^{-10}m)
^{o}C	Degree Celsius
N	Newton
Hz	Herz
Pa	Pascal

Some polymer related definitions:

Dispersion	Colloidal Particles in Water
Emulsion	Dispersion of Liquid Droplets in a Liquid
Latex	Polymer Particles Dispersed in Aqueous Solution (pl. Latices)
Monodisperse	Narrow Particle Size Distribution
Polydisperse	Wide Particle Size Distribution
Gyration Radius	Radius of the "Sphere" Formed by the Coiled Polymer Chain

CHAPTER 1: Introduction

One of the most important characteristics of a latex is the ability to form a solid, non-porous, elastic film after drying. This valuable property is used to manufacture adhesives, paints and other composites, because it happens at ambient conditions and is an irreversible process. The coalescence of the particles is too strong to resist disruptive forces, therefore addition of water does not redisperse the latex.

Many theories have been developed to understand the process of drying and film formation in a latex, to explain why the particles form a smooth flat film and do not dry as a powder or a porous gel [1-3]. These studies indicate that the process consists of three steps:

1) water evaporation from the latex [4-8]
2) particle deformation and interstitial water diffusion [9-11]
3) particle coalescence and formation of a film [12-17]

The Atomic Force Microscope (AFM), due to its resolution of a few nanometers and the non-destructive operation mode, is a versatile and powerful tool with which it is possible to monitor all three of the above mentioned steps and visualize the process of particle deformation and coalescence.

For a latex emulsion to form a smooth, continuous film at ambient conditions, the latex particles must be soft enough to deform and possibly interdiffuse. The glass transition temperature (T_g) is the temperature at which chain segments can start to move and the particles can interdiffuse. Thus the T_g is a particularly useful parameter to describe a polymer's ability to form a film.
A common way to manipulate the T_g of a latex is by the addition of coalescent aids or plasticizers, which lower the T_g of the latex in its wet state and allows film formation at a lower temperature. After the film has dried, the solvents evaporate and leave a high T_g film which is fairly stable.

A possible way to avoid the evaporation of these volatile plasticizers, while combining the properties of a low T_g, easily film-forming latex with a stabilizing high T_g component, is to use polymer blends, or structured latices, such as core-shell particles. Core-shell particles can, for example, consist of a more hydrophobic core polymer with a high T_g polymer, surrounded by a more hydrophilic shell polymer with a low T_g polymer.

The thermal parameters of a polymer, such as the T_g, can be determined by a variety of experimental methods. The most common are the Differential Scanning Calorimetry (DSC) and the Dynamic Mechanical Analysis (DMA). The disadvantage of both methods is that they determine an average T_g of the entire sample. The T_g cannot be measured locally on molecular scale.
If polymer blends or structured polymers are used in a latex, however, then it will be most interesting and useful to be able to determine the thermal parameters of all polymer phases locally, to ensure that the particles do in fact have the desired structure.

A new measurement method was developed to determine such thermal transitions of a polymer locally. It entails the use of the AFM in a probing mode. With this new technique it is now possible to determine, for example, the T_gs of the core and the shell individually for core-shell polymers.

1.1 Objectives

The overall aim of this research was twofold. On the one side was the comprehensive characterisation of different polymers with the AFM. The emphasis lay on latices with different polymer structures, different particle sizes and different core-shell ratios, but different polyolefins and ultra-thin polystyrene films were also investigated.

The film-formation behavior of latices with different polymer structure, particle size and different additives were investigated by AFM and the acquired image sequences compared. The results provided information on which polymer properties are most suitable for film formation at ambient conditions, as specifically required by the coatings industry.

The second aim of the research was the development of a new experimental method to determine thermal transition temperatures of polymers by AFM using it in a stationary probing mode. The results obtained by this mode of the AFM were compared to DSC and DMA results and the AFM evaluated for its abilities and accuracy as a technique to determine thermal transitions. The limits of the AFM as a tool to determine thermal transitions were evaluated with nano-morphologies, ultra-thin films and structured latices.

Layout of the thesis:

The first part of the thesis describes the mechanical properties of polymers and introduces different theories on the film-formation process.

The second part gives a short overview over different variants of Scanning Probe Microscopes (SPM), with special emphasis to the AFM, followed by the synthesis of the investigated polymers and the experimental setup used for the measurements

The results are presented in different sections. The first describes the film-formation behavior of different latices. Here the AFM was used to image polymer surfaces and give information about kinetic processes that happen while a film is formed.
The second section shows a few results obtained by Scanning Thermal Microscopy and the third section describes the determination of thermal parameters of polymers using the AFM in a stationary mode. Like the DMA it is used to excite the underlying molecules and measures their response, only here the response is measured locally on a molecular scale.

1.2 Bibliography:

[1] Dobler,F., Holl,Y., *Trends in Polymer Science*, 1996, **4**, 145
[2] Winnik,M., *Emulsion Polymerization and Emulsion Polymers, John Wiley, New York*, 1997,
[3] Keddie,J., *Materials Science*, 1997, **9**, 101
[4] Sheetz,D., *Journal of Applied Polymer Science*, 1965, **9**, 3759
[5] Vanderhoff,J., Bradford,E., Carrington,W., *Journal of Polymer Science: Symposium*, 1973, **41**, 155
[6] Croll,S., *Journal of Coatings Technology*, 1986, **58**, 41
[7] Croll,S., *Journal of Coatings Technology*, 1987, **59**, 81
[8] Winnik,M., Feng,J., *Journal of Coatings Technology*, 1996, **68**, 39
[9] El-Aasser,S., Robertson,A., *Journal of Paint Technology*, 1975, **47**, 50
[10] Frenkel,J., *Journal of Physics*, 1945, **9**, 385
[11] Dillon,R., Matheson,L., Bradford,E., *Journal of Colloid Science*, 1951, **6**, 108
[12] Mason,G., *British Polymer Journal* , 1973, **5**, 101
[13] Voyutsii,S., *Journal of Polymer Science*, 1958, **32**, 528
[14] Hahn,K., Ley,G., Oberthuer,R., *Colloid and Polymer Science*, 1991, **266**, 631
[15] deGennes,P., *Journal of Chemical Physics*, 1971, **55**, 572
[16] Wang,Y., Winnik,M., *Macromolecules*, 1993, **26**, 3147
[17] Linne,M., Klein,A., Sperling,L., Wignall,G., *Journal of Macromolecular Science: Physics*, 1988, **27**, 217
[18] Yoo,J., Sperling,L., Glinka,C., Klein,A., *Macromolecules*, 1991, **24**, 2868

CHAPTER 2: Theoretical Background

This chapter will give a background on the properties of polymers and introduce characteristic terms and quantities to describe the behavior of polymers.

2.1 Mechanical and Thermal Properties of Polymers

2.1.1 Mechanical Properties of Polymers

The mechanical properties of a polymer can be deduced from the response to a mechanical force, for example deformation. The mechanical properties of materials are usually divided into two groups. Solids, like metal or glass, are elastic for small deformations and the strain is proportional to the elongation, according to the Hookean law. Liquids, however, are viscous and the strain is proportional to the change of the elongation, according to Newton's law. The properties of polymers are a combination of both states – polymers are viscoelastic.

Linear, purely elastic behavior under deformation stress is described by the Hookean law:

$$\sigma_{ij} = c_{ijkl}\varepsilon_{kl} \tag{2.1}$$

where σ_{ij} is the stress tensor, ε_{kl} is the deformation tensor, and the elastic moduli are described by c_{ijkl}.

If the material shows certain symmetries, the number of linearly independent components of c_{ijkl} is reduced. In the case of the isotropic elastic solid only two linear independent moduli exist. The Hookean law can then be written as:

$$\sigma_{ij} = 2\mu\varepsilon_{ij} + \lambda\delta_{jl}\varepsilon_{ll} \tag{2.2}$$

with the Lamé moduli λ and μ and the Kronecker tensor δ_{ij}. The more commonly used moduli E (elastic modulus), C (compressibility modulus), G (shear modulus) and L (bulk modulus) can be calculated from the Lamé moduli using the following relationships [1]:

$$E = (3\lambda+2\mu)/(\lambda/(\mu+1)) \tag{2.3}$$
$$C = \lambda+2\mu/3 \tag{2.4}$$
$$G = (L-\lambda)/2 \tag{2.5}$$
$$L = \lambda+2\mu \tag{2.6}$$

Most polymers are neither purely elastic nor purely viscous. Due to the chain structure and possible side chains, the polymers show characteristics of both cases – this is called viscoelastic behavior.

The response of a polymer to a mechanical excitation is not immediate, but happens with a certain time delay. Relaxation, creeping processes and viscous flow of the polymer chains determine the viscoelastic properties of a polymer.
Taking these processes into consideration, the constant elastic moduli from the Hookean law can be replaced by time dependent moduli. For example shear deformation can be written as:

$$\sigma(t) = \int_{-\infty}^{t} G(t-t')\frac{d\varepsilon}{dt'}dt' \tag{2.7}$$

with the shear modulus G(t-t').
If the polymer is deformed periodically, as for example by torsion or elongation, then the observed mechanical stress will show a phase shift δ. With a sinusoidal excitation $\varepsilon = \varepsilon_0 \sin\omega t$, the mechanical response is $\sigma = \sigma_0 \sin(\omega t+\delta)$. Using the addition theorem this can be written as:

$$\sigma = \varepsilon_0 G' \sin\omega t + \varepsilon_0 G'' \cos\omega t \tag{2.8}$$

with $G' = \sigma_0/\varepsilon_0 \cos\delta$ and $G'' = \sigma_0/\varepsilon_0 \sin\delta$.

The periodical stress can be divided into a part in phase with the deformation and a part that is shifted 90°. Therefore the shear modulus can be written in a complex form as:

$$G^* = G' + iG'' \tag{2.9}$$

The real part G' is a measure of the stored energy and is referred to as the storage modulus. The imaginary part G'' is related to the dissipated energy:

$$\Delta E = \pi\varepsilon_0^2 G'' \tag{2.10}$$

and is referred to as the loss modulus. Both components depend on the frequency of the excitation [2]. The ratio of the loss modulus to the storage modulus is the loss factor

$$\tan\delta = \frac{G''}{G'} \tag{2.11}$$

which is a measure of the damping, or the internal friction of the polymer.

2.1.2 Polymer Dynamics

If a solid is elongated, the atoms or molecules move and settle to a new equilibrium position. A macroscopic deformation of a polymer leads to complex rearrangements of molecules. The length scale of these rearrangements ranges from lengths in the order of 1Å, if a single bond is involved, to the nanometer range for the entire

molecule. The time scale of these processes varies from 10^{-11}s to macroscopic times of several seconds [3].
The most common models to describe the movement of polymer chains are briefly introduced:

2.1.2.1 Rouse-Zimm Model

In this simple molecular model, the polymer chain is regarded as a chain of hard spheres connected by springs. The springs represent the entropic forces acting between the individual segments and show no interaction with the surrounding element. The Brownian motion of the chain segments without interaction forces can be calculated. The forces acting on the spheres, according to the Rouse model [4], are inertia forces, entropic spring forces, friction, and stochastic forces due to thermal movement and collisions.
The Brownian molecular movement excites cooperative relaxation motions (Rouse modes) in the polymer chain with the relaxation time $\tau_p = \tau_R/p^2$ (τ_R is a characteristic time, $p = 0,1,2,...$).
All modes show the same temperature dependence, which is a theoretical justification for the time-temperature superposition principle mentioned later in section 2.1.4 (equation 2.16) on which the Williams-Landel-Ferry (WLF) equation is based. The Rouse model becomes invalid for high molecular weight polymers, where entanglements start to influence the chain movement.

The Zimm model [5] is an extension of the Rouse model and takes hydrodynamic interaction forces into consideration as well. A moving chain segment of a polymer in solution causes a flow, which leads to the movement of other chain segments. The expression for the relaxation time under these circumstances changes to:
$\tau_p = \tau_R/p^{3/2}$.

2.1.2.2 Reptation Model

The reptation model was developed by de Gennes [6] and takes molecular interactions between the chain segments into consideration. The chains are hindered in their movement by other polymer chains. Eventually they move along the chain axis, as if locked into a pipe. The movement can be visualized as a twisting along the axis, like a snake – this is why it is called reptation. The relaxation time depends on the diameter of the pipe d: $\tau_e = \pi/12 \cdot d^4 \xi/kTa^2$
ξ is a measure for the friction of the chain, T is the temperature and a is the length of one chain segment.

2.1.3 Crystallization and Melting of Polymers

The crystallization of polymers is a rather complicated process. Entanglements and side groups of the polymer chains hinder the formation of ordered structures. Furthermore, a large number of configuration possibilities lead to a higher formation

entropy for polymers than, for example, for lower molecular substances. This leads to a high entropy difference between the amorphous and the crystalline phase, which is the reason, why polymers crystallize only partly.
One condition for the ability to crystallize is the regularity in chemical structure of the polymer chains over a long distance. An example of a well crystallizing polymer is polyethylene (PE), which consists of a simple, saturated carbon chain backbone without any pendant side groups. Statistical copolymers or atactic polymers usually do not crystallize, since order on a sufficient length scale is not present.

Polymer crystals are highly anisotropic because of the different bonding forces. The covalent bonds along the chain are about 10 to 50 times stronger than the secondary bonds (van der Waals bonds) between neighboring molecules within the crystal.
The crystals are also never perfect. Apart from defects typical to low molecular mass crystals, such as vacancies, impurity atoms and dislocations, polymer crystals have defects due to chain ends folding or conformational defects. The number of defects influences the melting point of a polymer crystal; it is lowered proportionally to the number of defects in the crystal. Beyond a critical number of defects the long-range order disappears entirely.

According to the Ehrenfest theory, [7] the crystallization- and melting-processes of polymers are regarded as a first order transition, but the transition region is usually wider than for low molecular crystals. In the case of PE the transition happens over a range of about 30 - 50°C. This effect is due to polymer chains of different lengths and more importantly to a certain distribution of the thickness of the crystal lamellae (see Figure 2.1).

The starting point for crystallization is the formation of nuclei from the amorphous melt. These are formed from bundles of parallel polymer chain segments. According to Hoffman [8] the maximum rate of crystal nucleation takes place between the glass transition temperature (T_g) and the melting temperature (T_m) of the polymer.
The growth of the crystals is dominated by secondary nucleation. The secondary nuclei are deposited in layers in the lateral direction on the primary nucleus, forming a lamellar crystal structure, separated by amorphous areas. Figure 2.1 illustrates the lamellar growth of a polymer crystal. The polymer chain folds into a lamellar structure but it also connects different lamellae and forms entanglements, which prevent the formation of a perfect polymer crystal.

Due to the branching of lamellae, two- or three-dimensional superstructures, which are commonly round or spherical, are formed. These crystal structures are called spherulites.

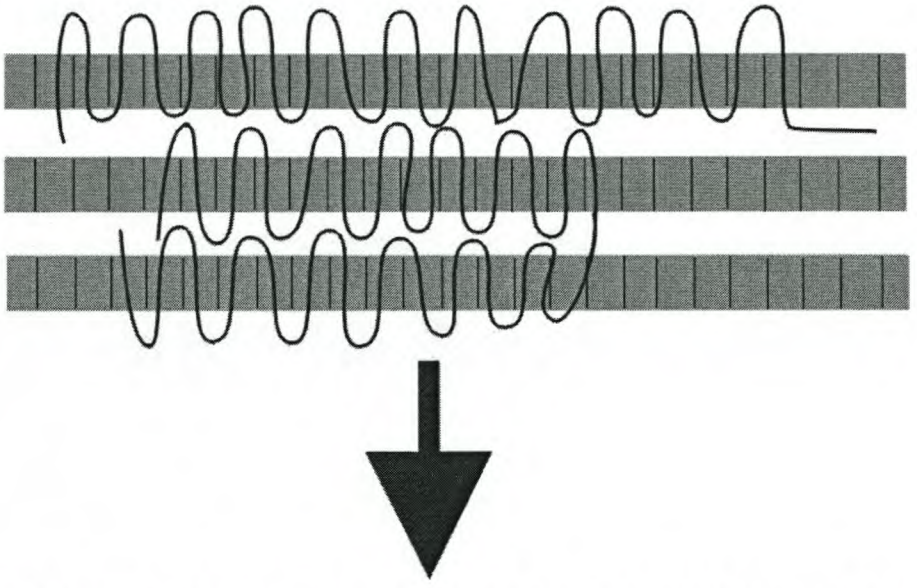

Figure 2.1: Crystal growth of a polymer crystal. The chains crystallise into lamellae, separated by amorphous areas.

The ratio of the lamellar thickness to its width is always considerably smaller than the theoretical value calculated from the surface energy. This means that the polymer crystals are not in a thermodynamic equilibrium and the crystal growth is not controlled by equilibrium thermodynamics. There is evidence that the crystals growing with greater velocity are favored in the crystallization process. This would confirm that the folding of polymer chains is a kinetic process. The kinetic crystallization theory of Hoffman and Lauritzen [9] expresses the thickness of a crystal as:

$$L_K = \frac{2\sigma_D T_m^0}{\Delta h_m \rho_K \Delta T} + \delta L = L_K^* + \delta L \qquad (2.12)$$

Where Δh_m is the melting enthalpy, σ_D is the surface energy of the folded area and ρ_K the density. δL takes into consideration that the average lamellae thickness L_K is usually greater than the minimum possible thickness L_K^*. This is the reason why the melting point of a polymer crystal is higher than its crystallization point.
The melting temperature T_m is a function of the lamellar thickness and is described by the Thompson-Gibbs equation:

$$T_m = T_m^0 \frac{1 - 2\sigma_D}{L_K \rho_K \Delta h_m} \qquad (2.13)$$

where T_m^0 is the melting temperature of a crystal of infinite size. Real polymer crystals with a thickness of about 10nm have according to equation 2.12, a lowering of their melting point of about 10 to 30K. The amount of the lowering depends on σ_D.

2.1.4 Glass Transition of Polymers

Besides thermodynamic transitions polymers show different relaxation processes, denoted by the greek letters, α, β, γ, etc., beginning at higher temperatures. The reason for the relaxation processes is molecular rearrangement and diffusion. The most important relaxation process is the α-relaxation, also called the glass transition of a polymer. In simple terms, the glass transition is the transition from a hard, glassy state, in which the macromolecules are frozen in an amorphous or semi-crystalline state, into a soft, rubbery state, in which the molecules can move and interdiffuse. All polymers have a glass transition.

The mechanical behavior of a polymer can be described as passing through four distinct regions, as illustrated in Figure 2.2 [12]. Figure 2.2 displays the complex shear modulus as a function of the temperature for higher molecular weight polymers.

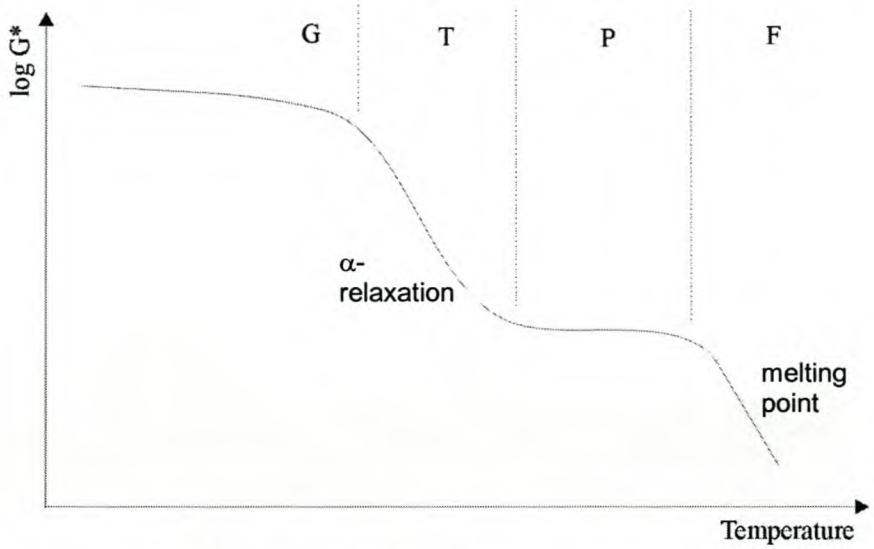

Figure 2.2: The complex shear modulus of a polymer as a function of the temperature.

In the hard, glassy state (G) the shear modulus reaches values of about one GPa. The molecular chains without order are in an amorphous state, and cannot move.
In the transition phase (T) the modulus decreases drastically and the polymer shows viscoelastic behavior, it becomes rubbery. The applied thermal energy may activate movement of chain segments, but most molecules remain in their initial position. The width of the transition phase depends on the molecular weight and structure of the polymer. The plateau phase (P) exists for higher molecular weight polymers (> 10^4 g/mol) and lies between the transition phase and the flow phase. In this region the polymer shows rubber-elastic behavior. The large molecule chains can move and interdiffuse but chain entanglements prevent irreversible flow. In the flow phase (F) the molecular chains are irreversibly shifted as entanglements slip more easily.

To activate the movement of chain segments, thermal or mechanical energy is required to overcome the potential barrier ΔE. The probability for overcoming this

energy barrier, given by the Boltzman factor k_BT, is increasing with increasing temperature and the relaxation time τ decreases, according to an Arrhenius-type law:

$$\tau = \tau_0 e^{-\Delta E / k_B T} \tag{2.14}$$

The frequency of the conformation changes in the polymer chains can then be expressed accordingly:

$$\nu = \nu_0 e^{-\Delta E / k_B T} \tag{2.15}$$

The ability of the chain segments to move is thus decreasing with decreasing temperature, while the relaxation time τ, and with it the viscosity $\eta = \tau G$, increase drastically.
Using equation 2.15 in relation for two different temperatures, leads to:

$$\log \nu_1 - \log \nu_2 = \log a_T = \frac{\Delta E}{k_B}(1/T_1 - 1/T_2) \tag{2.16}$$

The factor a_T is called shift factor. This means, that the temperature dependency of viscoelastic materials can be converted into a frequency dependency. Spectra measured at different temperatures can be superposed by shifting them along the logarithmic time-/frequency axis and added to a "master-curve".

For most polymers, however the Arrhenius law becomes invalid in the region of the glass transition and beyond (T_g +100K) and the relaxation time τ or the viscosity η are better described by the Vogel-Fulcher law [10,11]:

$$\eta = \eta_0 e^{C/T - T_{VF}} \tag{2.17}$$

with the Vogel-Fulcher temperature T_{VF}, which for most polymers is about 50K below the glass transition temperature T_g. At high temperatures the Vogel-Fulcher law approaches the Arrhenius law, as displayed in Figure 2.3.

While the temperature dependency of the glass transition can be described by the Vogel-Fulcher law, the secondary transitions (β,γ...) are better described by an Arrhenius law. The relaxation times of the different relaxation processes are related to the frequency at which the maximum of the loss modulus appears, according to $f_{max}=1/(2\pi\tau)$. Figure 2.3 shows a typical Arrhenius plot for the α- and β-transitions, in which the frequency f_{max} is plotted as a function of the inverse temperature. At high temperatures the two relaxation processes merge into an Arrhenius curve.

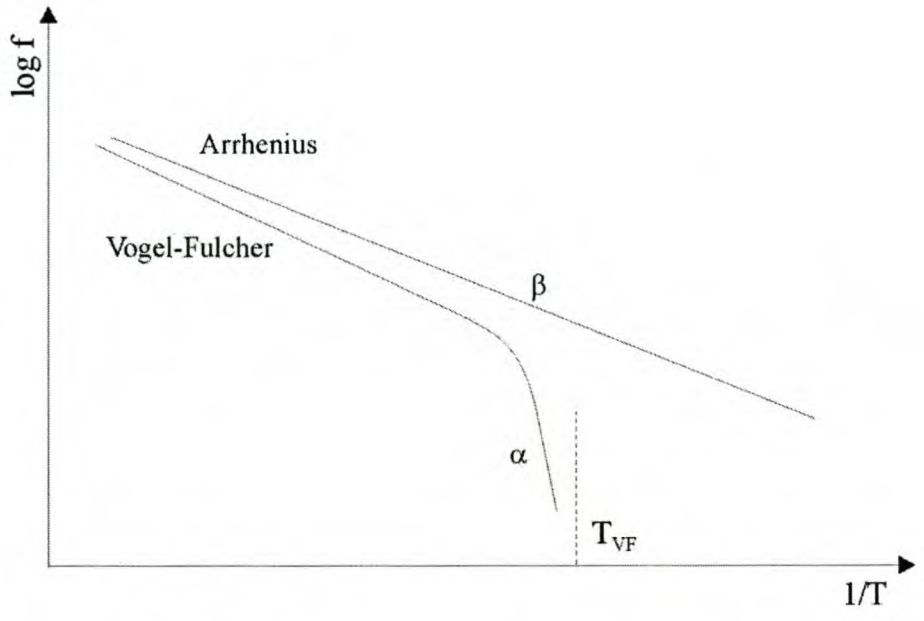

Figure 2.3: Arrhenius plot of the frequency maxima for the α-and β-relaxations.

Around the Vogel-Fulcher temperature T_{VF}, the glass transition (α-relaxation) temperature shows a greater frequency dependency than the secondary transitions. Depending on the polymer structure the T_g is raised about 7 to 10K every 10Hz.
In other words, the measured glass transition temperature depends strongly on the measurement method and the frequency used to deform the polymer.

In the region of the glass transition not only the mechanical properties are changed. The heat capacity, the compressibility and the thermal expansion coefficient also change rapidly at T_g, in accordance to a second order phase transition. The glass transition is, however not a second order phase transition, since the glassy state is not an equilibrium in the thermodynamic sense. The system is not at the absolute minimum of the Gibbs potential, but only at a local minimum. Depending on the cooling rate to the glassy state, there are numerous different local energy minima in which the polymer can exist. Thus, the thermal history of the polymer influences the characteristic of the glass transition.

Despite intensive research and different theoretical models [13], there is as yet no satisfactory microscopic theory to describe the glass transition correctly. The existing theories can be divided into three categories: the free volume theory [14,15], kinetic theories [16] and thermodynamic theories [17]. Mostly used and sufficient to explain the glass transition is the free volume theory:

2.1.4.1 Free Volume Theory

When the polymer chains are "packed" there will be free volume between them, due to the complex structure, and the resulting inability to fill available volume. This free volume is needed to enable the chain segments to move. The molecular mobility

and, with it, the viscosity depend on the free volume. The main premise of the free volume theory is that at the glass transition the movement of the chain segments freezes below a critical value of the free volume. In the glassy state the free volume is not temperature-dependent, but remains at a constant value reached at T_g. The overall volume V_g of the polymer in the glassy state is the sum of the occupied glass volume at 0K V_0, the free volume V_f and the temperature dependent volume for high frequency oscillations:

$$V_g = V_0 + V_f + \left(\frac{dV}{dT}\right)_g T_g \tag{2.18}$$

Above T_g, the oscillating volume and the free volume increases with increasing temperature. In this rubbery state the volume of the polymer is described by:

$$V_r = V_g + \left(\frac{dV}{dT}\right)_r (T - T_g) \tag{2.19}$$

According to Simha and Boyer [15], the relative free volume fraction f_g can be determined by the difference in the expansion coefficient above (α_r) and below (α_g) the glass transition:

$$f_g = \frac{V_f}{V_g} = T_g(\alpha_r - \alpha_g) \tag{2.20}$$

The free volume V_f depends strongly on the structure of the polymer and is typically in the range of a few percent of the overall volume.

From the free volume theory the empirical WLF-equation (Wiliams-Landel-Ferry) can be derived [18]. It describes the temperature dependence of relaxation times in polymers above their T_g.

The basis of the WLF equation is the Doolittle-equation for the viscosity:

$$\eta = Ae^{B/f_g} \tag{2.21}$$

A and B are empirical constants with values in the order of unity and f_g is the relative fraction of the free volume.
The ratio of a mechanical or dielectric relaxation time, τ_m or τ_d, at a temperature T, to its value at an arbitrary reference temperature T_0 can be represented by a simple empirical, but nearly universal function. The ratio a_T is:

$$a_T = \frac{(\tau_m)_T}{(\tau_m)_{T0}} = \frac{(\tau_d)_T}{(\tau_d)_{T0}} = \frac{(\eta_m)_T}{(\eta_m)_{T0}} \tag{2.22}$$

Substituting equation 2.21 in equation 2.22, the ratio can be expressed as:

$$a_T = e^{B/1/f - 1/f_R} \tag{2.23}$$

Selecting T_g as the reference temperature T_0 and replacing f by $f_g + \alpha_f(T-T_g)$, with the expansion coefficient α_f of the free volume, and taking the logarithm leads to:

$$\log a_T = -\frac{B/f\,(T - T_g)}{f_g/\alpha_f + T - T_g} \tag{2.24}$$

Comparing this to the empirical WLF-equation:

$$\log a_T = C_1 \frac{(T - T_R)}{C_2 + T - T_R} \tag{2.25}$$

leads to the following values for the coefficients:

$$C_1 = -B/2.303f_g \approx -17.4 \quad \text{and} \quad C_2 = f_g/\alpha_f \approx 51.6K$$

A significant conclusion of the WLF analysis is that the free volume fraction at T_g is nearly a constant value of $f_g = 0.025$.
If the free volume fraction is constant at T_g, it follows that the glass transition temperature for a polymer can be changed by altering its free volume fraction at a fixed temperature. One way to achieve this is to mix the polymer with another molecular unit, which has a larger free volume fraction at the same temperature. Chain ends have larger free volumes since they are only attached by one bond to the rest of the macromolecule. If the extra free volume of a chain end is θ, then the extra free volume per cm^3, due to chain ends in a sample with the bulk density ρ and the molecular weight M is:

$$\Delta V_f = (2\rho N_A/M)\theta \tag{2.26}$$

with the Avogadro number N_A. To compensate for the extra free volume by cooling due to thermal contraction a polymer of finite molecular weight M_n must be cooled below the T_g of an infinite molecular weight polymer with T_g^∞.

$$(2\rho N_A/M)\theta = \alpha_l(T_g - T_g^\infty) \tag{2.27}$$

with α_l the expansion coefficient of the melt. From this the Flory-Fox equation [19] can be derived:

$$T_g = T_g^\infty - K/M \quad \text{with} \quad K = 2\rho N_A\theta/\alpha_f \tag{2.28}$$

Random copolymers and compatible polymer blends show also a single T_g, usually between the T_gs of the corresponding pure homopolymers. A number of empirical

relationships have been proposed to relate the glass transition temperature of random copolymers and polymer blends to their composition, for example the Gordon-Taylor equation [20]:

$$T_g = (W_A T_{gA} \Delta\alpha_A + W_B T_{gB} \Delta\alpha_B)/(W_A \Delta\alpha_A + W_B \Delta\alpha_B) \quad (2.29)$$

or the Fox equation [21]:

$$1/T_g = W_A/T_{gA} + W_B/T_{gB} \quad (2.30)$$

where W_A and W_B are the weight fractions of the polymer components. The Fox equation was used to calculate the theoretical T_g of all copolymers used for the experiments.

2.1.4.2 Glass Transition Temperature of Surfaces and Interfaces

The glass transition temperature is affected by many factors, for example, the molecular structure. It was found that a single chain influences T_g through its stiffness and tacticity. Interactions between chains such as cohesive or dipole attraction, and H-bonding also modify T_g. Other structural effects, which alter T_g are molecular symmetry, copolymerization, molecular weight, branching and cross-linking.
The polymer structure from the bulk is not necessarily the same near the surface; here the segmental distribution of polymer chains might differ strongly. Reflectivity studies by Wu et al. [22] suggest that the crystallinity of some polymers is enhanced at the surface. These results are significant with respect to the difference in properties between the crystalline and amorphous phases of semicrystalline polymers.
In the case of purely amorphous polymers, Monte Carlo simulations [23-25] predict an excess of chain ends close to the free surface. These would have a marked influence on the thermal properties of the surface, for example a significant depression of the glass transition temperature.

Using simple scaling analysis, Mayes et al [26] calculated the theoretical depression of the surface T_g.
Considering a monodisperse system of polymer chains, each having N statistical segments of the length a, the characteristic diameter of the molecule is roughly equivalent to the root-mean-square end-to-end distance $R_0 = N^{1/2}a$. De Gennes [27] argued that the extent of chain-end segregation is controlled by the difference between the surface tension of an infinite polymer chain and that of the end groups: $\delta = \gamma_\infty - \gamma_e$. If $\delta a^2/kT$ is of the order of unity, all chain ends within a distance R_0 from the surface will be localized at the surface. Calculating the concentration of chain ends and a new effective degree of polymerization N, which gives the molecular weight equivalent for the same fraction of chain ends in bulk, leads to the following expression for the variation in T_g with molecular weight:

$$T_{g\sigma} = T_{g\infty} - C/N \quad (2.31)$$

with the material constant C. The 1/N dependence arises according to the free volume model from the enhanced contribution of chain ends to the total free volume of the system.
The magnitude of the depression of T_g, for example for a system of polystyrene chains of $1x10^5$ molecular weight, or N = 960, $T_{g\infty}$ = 373K and C = $1.1x10^3$ is 36K. The surface glass transition temperature is then $T_{g\sigma}$ = 337K.
For lower molecular weight materials the effect is even more pronounced. For a $2x10^4$ molecular weight polystyrene the surface T_g is lowered by about 79K, to $T_{g\sigma}$ = 294K.

Kajiyama et al. [28,29] measured the glass transition of the surface of low molecular weight polystyrene films with a lateral force microscope. They found a significant lowering of the T_g at the surface. The glass transition started already at 293K, due to an enrichment of chain ends at the surface.

The theoretical model is also in agreement with recent experimental results obtained by Zhao et al. [30]. They observed an enhanced segregation of chain ends to the surface by neutron reflection experiments.
Forrest et al [31] performed measurements using Brillouin light scattering and ellipsometry and observed not only a depression of the surface T_g, but also an increase in T_g at the substrate interface. An attractive interaction between the polymer chains and the hard wall (the substrate surface) will increase the number of contacts between the chains and the wall. Thus the chain mobility and the segmental motion of the polymers is decreasing, which leads to an increase the glass transition temperature.

2.1.4.3 The Minimum Film Formation Temperature

The minimum film formation temperature (MFT) is not a thermal transition such as T_g or T_m. It is the temperature at which a water-borne synthetic latex or emulsion will coalesce when cast on a substrate as a flat film. When this occurs, a clear transparent film is formed. At temperatures lower than the MFT a white, powdery, cracked film will result after the water has evaporated.
The MFT is usually closely related to the T_g, but not synonymous with it. While T_g can be determined by calculations, MFT can best be determined experimentally by using a MFT bar. This is a metal bar with a linear temperature gradient on which the latex is cast. The temperature at which the film becomes transparent is the MFT.
Depending on the polymer type and structure, the MFT is a few degrees below or above T_g.

2.2 Film Formation of Latex

The film formation behavior of latices is an important property affecting many applications, for example, in coatings. A better understanding of the fundamental mechanism of film formation is important for the design of optimal coating systems.

Latices with different glass transition temperatures are used for different applications. High T_g latices are used when a hard film is required, whereas low T_g latices are used in order to achieve coalescence at ambient temperature. Core-shell polymers allow the combination of the desirable properties of a stabilizing high T_g polymer with an ambient film-forming low T_g polymer.
The film formation of latices has been extensively studied. Dobler and Holl [32], Winnik [33] and Keddie [34] have reviewed the literature on latex film formation. The following description of the film formation process is a short summary of their findings.

The film formation process for a system of monodisperse latex particles is commonly described in three stages:

1) Evaporation of water (drying) and particle ordering: change from a colloidal dispersion into a hexagonal packed array.
2) Particle deformation - the particles are deformed into hexagons, interstitial voids disappear.
3) Interdiffusion of polymers across particle boundaries causing a change into a continuous material.

2.2.1 Water Evaporation and Drying

The process of drying generally refers to the evaporation of water from a latex system. Several models and mathematical descriptions consider the transport of water in the direction normal to the film surface. This directionality creates water concentration gradients with the lower concentration near the latex/air interface.

Sheetz [35] proposed that water evaporates first rapidly from the surface and forms a dry polymer membrane at the surface. It was suggested that this surface layer becomes sufficiently dense to enable transport of water only by diffusion through the polymer at the surface. The interstitial water subsequently evaporates more slowly by diffusion through this membrane [35-38] and the drying front moves from the edges of the film inwards [39].
The wet film has a convex shape because of its meniscus. This meniscus drives the ordering of the latex particles, as represented in Figure 2.4.

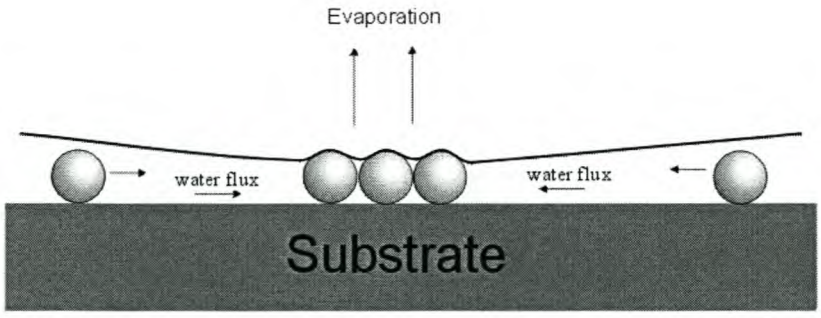

Figure 2.4: Schematic diagram of particle assembly and ordering driven by water flow to regions of faster evaporation [40].

In the first stage, the height of the water drops below the size of a particle. Capillary forces, caused by water evaporation, create a nucleus of a hexagonally ordered, two-dimensional cluster [41]. Evaporation from the ordered areas of the nucleus leads to convective particle flux to the edges of the growing nucleus. Water is drawn from the surrounding regions to maintain the water level and to compensate for evaporative water loss in the region of the nucleus. This incoming flux carries with it particles that subsequently become part of the ordered array of the colloidal crystal, until finally the entire latex forms an ordered array. This process is called convective self-assembly. The resulting colloidal crystal forms an FCC crystal [42,43].

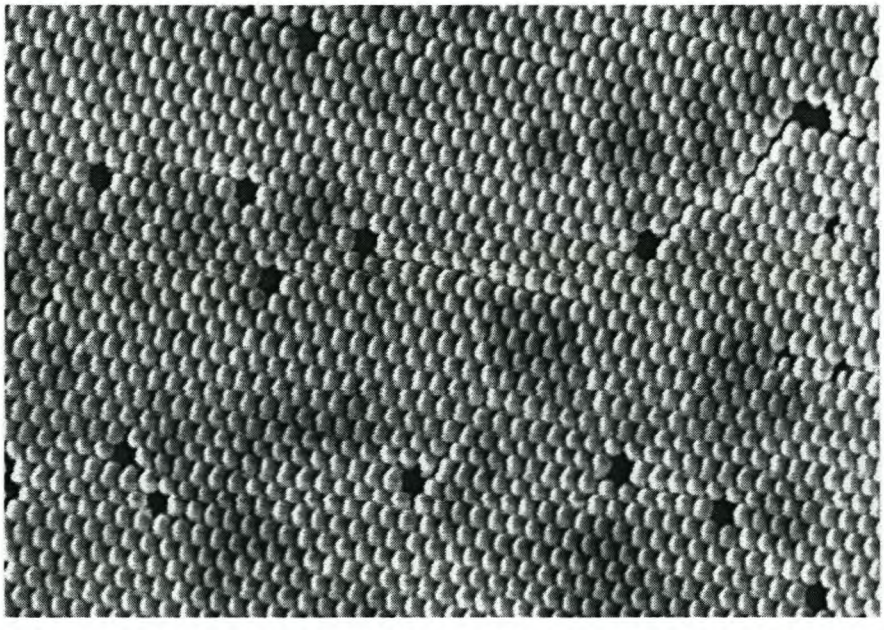

Figure 2.5: SEM image of polystyrene particles forming a colloidal crystal. The particles are hexagonally ordered with some vacancies and dislocations.

The evaporation rate affects the packing of the latex particles, and the faster the evaporation, the less the crystalline order [44]. It was also shown that freeze-drying produces colloidal crystals with a low packing order, since it increases the rate of evaporation.
Joanicot et al. [45] did not observe the formation of a long-range order under three circumstances:

1) When the latex volume fraction was less than 20%
2) when salt was present in the aqueous solvent
3) when the particles were polydisperse.

2.2.2 Particle Deformation and Coalescence

The latex surface flattens with further evaporation of the interstitial water. The particles move closer to each other and are deformed into hexagons. The interfacial tension between the polymer and water/air are sufficient to cause gradual coalescence and the observable particle boundaries are deformed and start to disappear [46].
Several hypotheses have been proposed to account for the origin of the deforming forces. Some of the hypotheses are based on the Frenkel model:
Frenkel's Model of Film Formation [47]:
Two spherical of equal diameter latex particles move closer to each other and coalesce. The contact surface between them increases until the pores between the particles become disconnected and are eventually closed. The process is illustrated as coalescence of two liquid drops, which are initially in contact at a single point only. After a time t the contact area will increase to a circle with the radius a(t). For simplicity it is assumed that the remaining parts of the drops keep a spherical shape. The contact radius is then given as: $a = r \sin\theta$, where r is the radius of the spherical portion of the drops. This is given by: $1/3\pi r^2(2+3\cos\theta-\cos^3\theta) = 4\pi/3r_0^3$. This equation expresses the constancy of the volume of each drop.

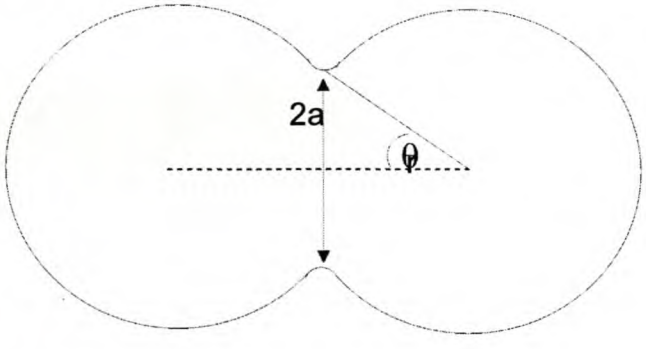

Figure 2.6: Schematic illustration of the cross section of two coalesced latex particles and forming a "neck".

The decrease in the surface of the drops is:

$$S_0 - S = 8\pi r_0^2 - 4\pi r^2 (1+\cos\theta) \qquad (2.32)$$

The time-dependent work of the surface tension forces can then be described as:

$$-\sigma \frac{dS}{dt} = 4\pi r_0^2 \sigma \frac{d\theta}{dt} \qquad (2.33)$$

with the surface tension σ. From this equation follows a time dependency for the contact angle θ:

$$\theta^2 = \frac{3}{2}\pi\frac{\sigma}{r\eta}t \tag{2.34}$$

and the contact area:

$$\pi a = \frac{3R\sigma}{2\eta}t \tag{2.35}$$

Dillon et al. [48] postulated that the main driving force for particle coalescence is provided by the polymer surface tension following the evaporation of water. Subsequently, the particles undergo dry sintering (coalescence driven by the polymer air interfacial tension) accompanied by viscous flow and subsequent particle deformation. They proposed that the relationship developed by Frenkel for the coalescence of spheres due to purely viscous flow governs the process of film formation:

$$a^2 = \frac{3\sigma Rt}{2\pi\eta} \tag{2.36}$$

where a is the contact radius of two coalesced spheres, σ is the polymer surface tension, R is the particle radius, t is the elapsed time and η is the polymer viscosity.

Brown [41] later proposed that at least four forces tend to be involved in the coalescence of polymer particles:

1) the force produced by the curvature of the polymer surface F_S
2) the capillary force resulting from the curvature of the water surface present in the interstitial capillary system during the period of water loss F_C
3) the Van der Waals forces between the spheres, F_V, and
4) gravitational forces which lead to settling in a dispersion F_g.

The forces that tend to resist coalescence are the resistance of spheres to deformation F_R and the coulombic repulsion F_e.
For coalescence to happen, the following inequality must be fulfilled:

$$F_S + F_C + F_V + F_g > F_e + F_R \tag{2.37}$$

The capillary force is substantially larger than the other forces particularly when the latex contains emulsifier. The coulombic repulsion is considered negligible compared to the resistive force F_R. The inequality can therefore be reduced to:

$$F_C > F_R \quad \text{or} \quad 12.9\sigma A/R > 0.37G(t)A \tag{2.38}$$

with σ the surface tension of water, $G(t)$ the time dependent elastic shear modulus of the polymer and A the area over which the forces act. The condition for film formation to occur is then:

$$G(t) < 35\sigma/R \tag{2.39}$$

Mason [49] corrected this formula to:

$$G(t) < 266\sigma/R \quad (2.40)$$

because the areas over which the capillary pressure has an effect and the pressure due to particle contact are not equivalent. The capillary pressure is also not constant.

Both models utilize an elastic model to describe the deformation of polymer spheres. This implies that when the stress is removed, the spheres will rebound to their spherical shape. Since the polymer is in fact viscoelastic, the validity of both models is questionable.

The capillary forces alone are not sufficient for particle deformation. The second part of the driving force is surface forces provided by the interfacial tension between polymer and water (wet sintering [35],[50]) or polymer and air (dry sintering [48,51]). Capillary forces account for the viscoelastic deformation, followed by viscous flow driven by interfacial tension [48],[51-53].

2.2.2.1 Dry Sintering

Dry sintering means that the coalescence of the particles is driven by the polymer/air interfacial tension. Sperry et al. [51] modeled interparticle void space as air bubbles that shrink by viscous flow under the action of surface tension. The role of the water in particle deformation is dependent on the temperature of the system. The MFT, which corresponds to the minimum void size for optical clarity, was related to the time and the particle size. Figure 2.7 shows the rate limiting steps in film formation:

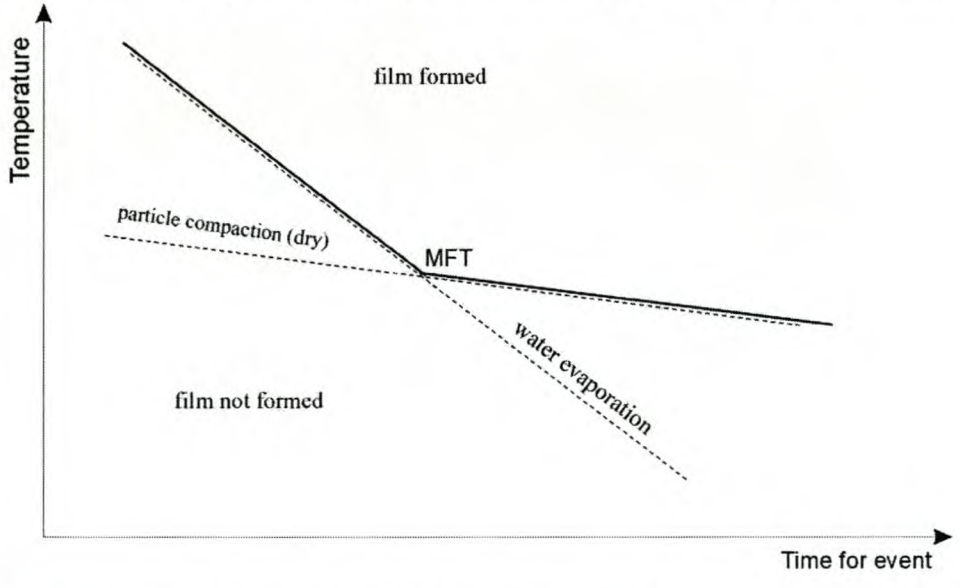

Figure 2.7: Dependence of the MFT on time and temperature

2.2.2.2 Wet Sintering

In the case of wet sintering the coalescence of the particles is driven by the interfacial tension between the polymer and water/air. Vanderhoff et al. [50,53] developed a model in which the interfacial tension between water and air first forces the latex

particles into contact with each other. When this force is sufficiently large, the stabilizing outer layer of particles is ruptured. This stabilizing layer is described as consisting of an electric double layer and emulsifiers. Polymer-polymer contact is obtained by the rupture of this layer, and the polymer/water interfacial tension becomes operative and induces a pressure on the polymer particles.
The results of this theory show that the pressure inducing fusion is essentially independent of the size of the latex particles. This implies that the minimum film formation temperature (MFT) should also be independent of the particle size.

Sheetz [35] proposed that interfacial tension and capillarity create a "skin", or membrane at the air/latex interface. Water can still evaporate from the underlying wet latex by diffusion through the membrane. This evaporation thereby generates a compressive force normal to the film, which leads to the particle deformation.
Eckersley and Rudin [54] proposed that capillary forces account for viscoelastic particle deformation. This is followed by viscous flow driven by interfacial tension. The contact radius a was expressed as a function of the complex shear modulus G^* and the particle radius R. Deformation resulting from capillary forces leads to a contact radius proportional to $(R^2/G^*)^{1/3}$, whereas interfacial tension should lead to a contact radius that varies as $(R/G^*)^{1/2}$. The experimental values were found to be between the two curves. This supports the theory that both, interfacial tension and capillarity account for the particle deformation.

Kendall and Padget [55] propose that adhesive forces are the origin of the deformation. Both Brown's and Kendall/Padget's theories predict that the deforming force is inversely proportional to the size of the latex particle.
Eckersley/Rudin and Jensen/Morgan [52] and Kan [56] found that the minimum film formation temperature is a function of the particle size, and increases with the particle diameter.

2.2.2.3 Flattening of the Particles

The particles are not only deformed into hexagons. AFM studies [57-59] show that the surface becomes smooth, which means the particles are flattened.
Lin et al. [57] found that smoothing of a corrugated surface takes about ten times longer under dry conditions than with condensed water on the surface. This leads to the conclusion that capillary pressure is typically the dominant driving force for film formation. Furthermore, it was found that the distance between particle centers does not change as the surface flattens during annealing. Therefore it was argued that the application of Frenkel-type sintering models is invalid for film formation, because an increase in the contact radius $a \sim t^{1/2}$ is predicted. Accordingly, the magnitude of decrease in height z should vary as $t^{1/2}$.

Goh et al. [58] noted that the average peak-to-valley height z decreases with time faster than an exponential decay; a $\log z^2 \sim \log t$ behavior was observed. A possible explanation is that the polymer chains next to the polymer surface diffuse faster than those within the film due to less hindrance to motion and an additional driving force from the surface energy. This is consistent with the results of theoretical models and

Monte Carlo simulations, which predict that the polymer mobility is higher next to the surface [60,61].

Goudy et al. [59] found that the peak to valley height decreases at a greater rate for smaller particles (≈ 250nm) than for larger particles (≈ 350nm). This could be due to a greater driving force from capillary forces in the smaller particles.

All these studies show that the Frenkel model is only valid for describing the initial particle necking. It is more appropriate to describe the decrease in z as the decay of the amplitude of a sinusoidal surface under action of surface tension. Mullins [62] predicted that z would vary as t^{-2}. This time dependence is expected at later times, when the Frenkel equation no longer applies.
According to Mayes et al. [26], the segregation of chain ends at the particle surface might have a relevant influence on the particle deformation. The reason is that the molecular weight of emulsion polymers near the surface of latex particles is lower than in the bulk of the particle [60]. As a consequence, the T_g and the viscosity are both expected to be lower at the latex surface than in the bulk [58]. According to Evers et al. [61] the surface mobility is enhanced because chain ends and shorter chains are preferentially located at the surface of the particles.

The model developed by Dillon, Matheson and Bradford postulates that surface forces, such as surface tension, drive the polymer particles to coalesce. They applied Frenkel's model to describe the coalescence of spheres by viscous flow. As coalescence proceeds, the contact angle θ increases with increasing surface tension γ and time t, and decreases with increasing particle size r and viscosity η.

$$\theta^2 = \frac{3\gamma t}{2\pi r \eta} \tag{2.41}$$

Since γ and t do not vary from particle to particle in an emulsion, one can expect particle size to have an effect on the film formation behavior of a latex.

Brown's theory suggests capillary forces as main driving forces for particle coalescence. Although different in the mechanisms, both proposed models – Brown's and Dillon's - suggest that small particles should coalesce more easily than large ones.

2.2.3 Particle Interdiffusion

Physical contact between latex particles is insufficient to produce a strong continuous film. To obtain a stable film it is necessary that segments of polymer chains diffuse from one latex particle to another [63] to provide a sufficient level of entanglement between chains in neighboring latex particles, thus imparting mechanical strength. Increasing molecular weight and increasing incompatibility of polymers lower the interdiffusion rate, whereas dense crosslinking of the matrix accelerates interdiffusion [64].

The diffusion coefficient D is found to decrease with time. According to the reptation model, diffusion in polymers above their entanglement molecular weight is expected to vary inversely with the square of the molecular weight [65]. If shorter chains are at the particle surface, therefore, the diffusion rate is faster. Experimentally, D in a series of PBMA samples has been found by Wang et al. [66] to decrease with molecular weight according to a -2.3 power law.
An increase in the gyration radius R_g has been observed by Linne et al. [67] when the polymers are heated above their T_g. They concluded that a coherent, tough film was obtained when there was an increase in R_g of about 5 to 6 nm. In a subsequent publication, Yoo et al. [68] concluded that the two important parameters determining the diffusion rate in a latex are the location of chain ends and the ratio of the gyration radius R_g of the polymer to the particle radius r.

Diffusion coefficients D, determined by applying a spherical diffusion model, are dependent on time and temperature. A decrease over time is attributed to the effect of low molecular weight chains near the particle surface dominating at early times. For lower molecular weight, the volume fraction of mixing f_m of the polymer particles can be described by the Fickian diffusion law in which $r \sim t^{1/2}$.
For higher molecular weight polymers ($6x10^5$), the volume fraction of mixing f_m becomes proportional to $r \sim t^{1/4}$. The diffusion law or the reptation model cannot explain this dependence [69,66].
The temperature dependence is consistent with the WLF equation; D increases with increasing temperature and decreases with an increase in the molecular weight of polymers.
Acrylic acid-rich phases at the particle surface can create a continuous network, or interphase, upon film formation of the latex. They form an interphase between the bulk particles, which can further prevent particle interdiffusion [70].

Kim and Winnik [71] have outlined a general scenario for interdiffusion in core-shell systems. In systems where the thin shell membranes are poorly miscible with the core polymer, interdiffusion is prevented. It can only take place when the membrane ruptures. If core and shell polymers are miscible, interdiffusion is not always suppressed. In some cases the core polymers can diffuse across the membranes, depending on their molecular weight [72].

Organic solvents, or coalescing aids, lead to enhanced rates of polymer interdiffusion [73,74]. The interdiffusion rate is also faster in the presence of co-surfactants (cetyl and stearyl alcohols) at times longer than the reptation time τ [75].

2.2.4 Effect of Emulsifiers and Surfactants

Surfactants are nearly always present in a polymer latex. They are known to affect several aspects of film formation, such as the colloidal stability, particle ordering, evaporative drying mechanisms, the extent of particle deformation and the rate of polymer interdiffusion.
Surfactants affect the mechanisms of drying as well as the rate of evaporation – addition of surfactant usually leads to a slower evaporation rate [76]. They can also

lead to the opposite effect – an acceleration of the evaporation rate of water in the late stages of drying. This effect is attributed to the influence of the surfactant on flocculation and gelation. Surfactants create a hydrophilic membrane that assists water transport in the film [39].
Particle flocculation at an early stage of drying prevents close packing. Post-added stabilizer postpones flocculation and allows closer particle packing [77]. AFM investigations of Juhue et al. [78] on the dependence of the peak-to-valley height z on surfactant concentration, revealed that full coverage of the latex particles leads to the highest degree of ordering and the densest packing at the film surface.
In a non-polar, hydrophobic latex the MFT becomes higher with addition of SDS and a nonyl phenol ethylene oxide, than with SDS alone. In contrast the MFT is higher in a hydrophilic latex with the addition of SDS than with the surfactant combination [79].

2.2.5 Effect of Pigments

Experiments indicate that the required time for film formation is roughly independent of the pigment volume concentration and extender size [80]. However, non film-forming particles will undoubtedly influence the morphology of films.
The importance of van der Waals forces originating from the pigments over capillary forces has been confirmed by AFM studies [81]. The viscoelastic properties of latex particles were shown to affect transport along inorganic surfaces. Whereas hard particles show lateral transport presumably induced by capillarity, soft particles deform and adsorb on inorganic surfaces and therefore cannot undergo aggregation and ordering.

2.2.6 Latex Blends and Composite Latex Particles

Blends of latices with different T_g's are interesting for industrial use. The latex with the lower T_g will film-form to create a continuous phase to which the higher T_g latex will impart desirable mechanical or optical properties. Such blends would not require volatile solvent plasticizers and therefore should be less damaging to the environment.
The storage modulus increases with increasing concentration of high T_g particles and the sintering process becomes slower [82]. In environmental scanning electron microscope (ESEM) and AFM studies the softer particles formed a continuous film around the harder particles. The harder particles were always found to be at the latex surface [82,83].

The use of core-shell latices can offer the same advantage as homogeneous particles post-added with film forming (coalescent) aid and avoid the disadvantage of solvent emission during the film formation process. The low T_g shells can lead to film formation while hard cores improve mechanical properties and stabilize the film. MFT measurements indicate that the shell, rather then the core, has greater impact on film formation [84]. With increasing thickness of a hard shell around a soft core, the MFT increases. However, when the thickness of a soft shell increases, the MFT drops.

AFM studies by Sommer et al. [85] supported a shell formation mechanism via an aggregation mechanism of nucleating microdomains of PMMA growing in size and then coagulating.
Juhue [86] studied interdiffusion during the film formation of core-shell latex particles. Particles with a high T_g core and a low T_g shell exhibit interparticle chain diffusion that is comparable to what is found in the high T_g latex with an added film-forming solvent.

2.2.7 Thin Films

The properties of latex films change dramatically when the film thickness becomes comparable to the length scale of the polymer, for example the gyration radius r_G. The conformation of the polymer molecules will be disturbed and the confinement restrictions affect the mechanical properties of the sample. One of these properties is the glass transition temperature T_g. Keddie et al. [87] measured the T_g of thin films by ellipsometry and found a reduction of T_g with the film thickness h according to:

$$T_g(h) = T_g^{bulk}\left[1-\left(\frac{\alpha}{h}\right)^{\delta}\right] \tag{2.42}$$

with the fit parameters α and δ. They suggested that the reduction in T_g is caused by the interaction between the substrate and the polymer. Experimental results obtained by Zheng et al. [88] demonstrated that the chain mobility is strongly influenced by substrate effects. A strong attractive interaction between the substrate and the polymer might even increase the T_g. They expected higher chain mobility at the free surface, which is in agreement with theoretical models by Mayes [26] (see also chapter 2.1.4), De Gennes [6] and Baschnagel [89]. Simulations by Baschnagel et al. showed that the chain mobility in the surface layer is highly anisotropic with an enhancement / reduction parallel / perpendicular to the interface. Since the surface-area to volume ratio of ultra thin films is extremely large these effects become predominant.
Forrest et al. [90] described the lowering of T_g by the empirical relation:

$$T_g(h) = \begin{cases} T_g^{bulk}\left[1-\left(\frac{h_0-h}{\xi}\right)\right], & h < h_0 \\ T_g^{bulk}, & h \geq h_0 \end{cases} \tag{2.43}$$

with the slope parameter ξ. For the threshold value h_0 below which the T_g decreases linearly they found $h_0 \approx 690$ Å. Above h_0 T_g has the bulk value. This empirical relation was later confirmed by experimental measurements [31].

2.3 Bibliography

[1] Alig,I., *Handbuch der Kunststoffpruefung*, 1992, Kapitel 10.2,
[2] Tadjbakhsch,S., *PhD thesis, Technische Universitaet Darmstadt, Physik*, 1998,
[3] Doi,M., Edwards,S., *The theory of polymer dynamics, Oxford science publication, Clarendon press 1988*, 1988,
[4] Rouse,P., *Journal of Chemical Physics*, 1953, **21**, 1272
[5] Zimm,B., *Journal of Chemical Physics*, 1956, **24**, 269
[6] deGennes,P., *Physics*, 1967, **3**, 37
[7] Greiner,W., 1983, Statistische Mechanik, 2. Edition, Verlag Harry Deutsch
[8] Hoffman,J., Davis,G., Lauritzen,J., Treaties on solid state chemistry, Plenum Press, New York, 1976,
[9] Lauritzen,J., Hoffman,J., *J. Res. Nat. Bur. Std*, 1060, **64A**, 73
[10] Fulcher,G., *Journal of the American Chemical Society*, 1955, **77**, 3701
[11] Vogel,H., *Physikalische Zeitung*, 1921, **22**, 645
[12] Buchenau,U., *22. IFF Ferienkurs 1991, Forschungszentrum Juelich*
[13] Donath,E., *Relaxation and Thermodynamics in Polymers, Akademie Verlag, Berlin 1992*
[14] Cohen,M., Turnbull,D., *Journal of Chemical Physics*, 1959, **31**, 1164
[15] Simha,R., Boyer,R., *Journal of Chemical Physics*, 1962, **37**, 1003
[16] Wunderlich,R., *Macromolecular Physics, Academic Press, New York*, 1976, Vol II
[17] Gibbs,J., DiMarzio,E., *Journal of Chemical Physics*, 1958, **28**, 373
[18] Williams,M., Landel,R., Ferry,J., *Journal of the American Chemical Society*, 1955, **77**, 3701
[19] Fox,T., Flory,P., *Journal of Polymer Science*, 1954, **14**, 315
[20] Gordon,M., Taylor,J., *Journal of Applied Chemistry*, 1952, **2**, 493
[21] Fox,T., *Bulletin of the American Physical Society*, 1956, **1**, 123
[22] Wu,W., Satija,S., Majkrazak,C., *Polymer Communications*, 1991, **32**, 262[23] Winkler,R., Matsuda,T., Yoon,D., *Journal of Chemical Physics*, 1993, **98**, 1
[24] Kumar,S., Vacatello,M., Yoon,D., *Journal of Chemical Physics*, 1988, **89**, 5206
[25] Harris,J., *Journal of Physical Chemistry*, 1992, **96**, 5077
[26] Mayes,A., *Macromolecules*, 1994, **27**, 3114
[27] deGennes,P., *C. R. Acad. Sci. (Paris)*, 1988, **307**, 1841
[28] Tanaka,K., Taura,A., Ge,S., Takahara,A., Kajiyama,T., *Macromolecules*, 1996, **29**, 3040
[29] Kajiyama,T., Tanaka,K., Takahara,A., *Macromolecules*, 1997, **30**, 280
[30] Zhao,W., Zhao,X., Rafailovich,M., Sokolov,J., et al., *Macromolecules*, 1993, **26**, 561
[31] Forrest,J., Dalnoki-Veress,K., Dutcher,J., *Physical Review E*, 1997, **56**, 5705
[32] Dobler,F., Holl,Y., *Trends in Polymer Science*, 1996, **4**, 145
[33] Winnik,M., *Emulsion Polymerization and Emulsion Polymers, John Wiley, New York*, 1997,
[34] Keddie,J., *Materials Science*, 1997, **9**, 101
[35] Sheetz,D., *Journal of Applied Polymer Science*, 1965, **9**, 3759
[36] Vanderhoff,J., Bradford,E., Carrington,W., *Journal of Polymer Science: Symposium*, 1973, **41**, 155

[37] Croll,S., *Journal of Coatings Technology*, 1986, **58**, 41
[38] Croll,S., *Journal of Coatings Technology*, 1987, **59**, 81
[39] Winnik,M., Feng,J., *Journal of Coatings Technology*, 1996, **68**, 39
[40] Denkov,N., Velev,O., Kralchevsky,P., *Nature*, 1993, **361**, 26
[41] Brown,G., *Journal of Polymer Science*, 1956, **22**, 423
[42] Pusey,P., vanMegen,W., Bartlett,P., *Physical Review Letters*, 1989, **63**, 2753
[43] Rieger,J., Haedicke,E., Lindner,P., *Physical Review Letters*, 1992, **68**, 2782
[44] Sosnowski,S., Li,L., Winnik,M., Clubb,B., Shivers,R., *Journal of Polymer Science, B: Polymer Physics*, 1994, **32**, 2499
[45] Joanicot,M., Wong,K., Maquet,J., Cabane,B., *Colloid and Polymer Science*, 1992, **270**, 806
[46] El-Aasser,S., Robertson,A., *Journal of Paint Technology*, 1975, **47**, 50
[47] Frenkel,J., *Journal of Physics*, 1945, **9**, 385
[48] Dillon,R., Matheson,L., Bradford,E., *Journal of Colloid Science*, 1951, **6**, 108
[49] Mason,G., *British Polymer Journal* , 1973, **5**, 101
[50] Vanderhoff,J., Tarkowski,H., Jenkins,M., Bradford,E., *Journal of Macromolecular Chemistry*, 1966, **1**, 361
[51] Sperry,P., Snyder,B., O'Dowd,M., Lesko,P., *Langmuir*, 1994, **10**, 2619
[52] Jensen,D., Morgan,L., *Journal of Applied Polymer Science*, 1991, **42**, 2845
[53] Vanderhoff,J., *Br. Polymer Journal*, 1970, **2**, 161
[54] Eckersley,S., Rudin,A., *Journal of Coatings Technology*, 1990, **62**, 89
[55] Kendall,K., Padget,J., *International Journal of Adhesion and Adhesives*, 1982, **July**, 149
[56] Kan,C., *Proceedings TAPPI Adv. Coating Fundation Symposium*, 1993, **101**,
[57] Lin,F., Meier,D., *Langmuir*, 1995, **11**, 2726
[58] Goh,C., Juhue,D., Leung,O., Wang,Y., Winnik,M., *Langmuir*, 1993, **9**, 1319
[59] Goudy,A., Gee,M., Biggs,S., Underwood,S., *Langmuir*, 1995, **11**, 4454
[60] Clay,P., Gilbert,G., *Macromolecules*, 1995, **28**, 552
[61] Evers,O., Ley,G., Haedicke,E., *Macromolecules*, 1993, **26**, 2885
[62] Mullins,W., *Journal of Applied Physics*, 1959, **30**, 77
[63] Voyutsii,S., *Journal of Polymer Science*, 1958, **32**, 528
[64] Hahn,K., Ley,G., Oberthuer,R., *Colloid and Polymer Science*, 1991, **266**, 631
[65] deGennes,P., *Journal of Chemical Physics*, 1971, **55**, 572
[66] Wang,Y., Winnik,M., *Macromolecules*, 1993, **26**, 3147
[67] Linne,M., Klein,A., Sperling,L., Wignall,G., *Journal of Macromolecular Science: Physics*, 1988, **27**, 217
[68] Yoo,J., Sperling,L., Glinka,C., Klein,A., *Macromolecules*, 1991, **24**, 2868
[69] Wang,Y., Zhao,C., Winnik,M., *Journal of Chemical Physics*, 1991, **95**, 2143
[70] Zosel,A., *Polymer Advanced Techniques*, 1995, **6**, 263
[71] Kim,H., Winnik,M., *Macromolecules* , 1995, **28**, 2033
[72] Joanicot,M., Wong,K., Cabane,B., *Macromolecules*, 1996, **29**, 4976
[73] Winnik,M., Wang,Y., Haley,F., *Journal of Coatings Technology*, 1992, **64**, 51
[74] Juhue,D., Lang,J., *Macromolecules* , 1994, **27**, 695
[75] Kim,K., Sperling,L., Klein,A., Hammouda,B., *Macromolecules*, 1994, **27**, 6841
[76] Okubo,M., Takeya,T., Tsutsumi,Y., Kadooka,T., Matsumoto,T., *Journal of Polymer Science, A*, 1981, **19**, 1
[77] Isaacs,P., *Journal of Macromolecular Chemistry*, 1966, **1**, 163
[78] Juhue,D., Lang,J., *Langmuir*, 1993, **9**, 792

[79] Powell,E., Clay,P., Sauntson,B., *Journal of Applied Polymer Science*, 1968, **12**, 1765
[80] Gate,L., Preston,J., *Journal of Surface Coatings*, 1995, **78**, 321
[81] Butt,H., Kuropka,R., *Journal of Coatings Technology*, 1995, **67**, 101
[82] Keddie,J., Meredith,P., Jones,R., Donald,A., *Langmuir*, 1996, **12**, 3793
[83] Patel,A., Feng,J., Winnik,M., Vancso,G., Dittman,C., *Polymer*, 1996, **37**, 5577
[84] Morgan,L., *Journal of Applied Polymer Science*, 1982, **27**, 2033
[85] Sommer,F., Duc,T., Pirri,R., Meunier,G., Quet,C., *Langmuir*, 1995, **11**, 440
[86] Juhue,D., Lang,J., *Macromolecules* , 1995, **28**, 1306
[87] Keddie,J., Jones,R., Cory,R., *Europhysics Letters*, 1994, **27**, 59
[88] Zheng,X., Sauer,B., Van Alsten,J., Schwartz,S., Rafailovich,H., Sokolov,J., Rubinstein,M., *Physical Review Letters*, 1995, **74**, 407
[89] Baschnagel,J., Binder,K., *Macromolecules*, 1995, **28**, 6808
[90] Forrest,J., Dalnoki-Veress,K., Stevens,J., Dutcher,J., *Physical Review Letters*, 1996, **77**, 2002

CHAPTER 3: Scanning Probe Microscopy (SPM)

This chapter will give a brief introduction into Scanning Probe Microscopy and explain the basic principles of SPM. Special emphasis will be placed on the Atomic Force Microscope (AFM).

Scanning Probe Microscopes include all microscopes where a sharp probe is scanned across a sample surface and the interactions between the probe and the sample surface are detected at each point. The resulting data matrix can be presented as a three-dimensional image, representing either the topography or any other interaction force that was measured. The probe is mounted on a silicon cantilever with a fairly low force constant. A change in the interaction force will bend the cantilever and change its position. This change is detected and mapped.
The scanning motion across the surface is in most SPMs realized by using piezo crystals that move the probe in x- and y-direction. A piezo in z-direction controls the distance between the probe and the sample.

The Scanning Tunneling Microscope (STM), invented by Binning and Rohrer [1], was the first Scanning Probe Microscope. It was introduced in 1982 for studying conductive metal surfaces. The STM detects a tunneling current between the metal tip and the conductive sample surface.
The Atomic Force Microscope (AFM) was a further step in the development of the SPM by Binning, Quate and Gerber in 1986 [2]. It detects the atomic forces acting between the probe and the sample surface, thus allowing the surface topography of non-metals and non-conductive materials to be studied as well. Hence it provides an obvious advantage for materials like polymers.

Other interaction forces that can be detected are the electrostatic force (EFM), using a silicon tip that is affected by the presence of surface charges on the sample [3], the magnetostatic force (MFM), using a magnetic tip that is affected by the magnetic moments on the sample surface [4]. The Scanning Nearfield Optical Microscope (SNOM) detects the reflection or transmission of light on the sample surface. It uses a glass fiber instead of the tip, through which a light beam is focused on the sample surface [5]. The Scanning Thermal Microscope (SThM) detects the temperature or the heat capacity of the sample [6,7], by measuring the change of resistance through a small wire that is scanned over the surface.

3.1 Signal Detection

The SPM probe is mounted on a silicon cantilever that will bend according to the repulsive or attractive forces that the probe experiences. In most SPMs the movement of the cantilever is detected by the distortion of a laser beam, which is reflected from the cantilever, as displayed in Figure 3.1. If the interaction between the probe tip and the sample surface, or the force acting on the tip, changes, the cantilever is bent and the deflected laser beam shifts. The intensity of the laser is

detected by a photodiode with four segments. The change of light intensity in the four quadrants is used to calculate the force acting on the tip.

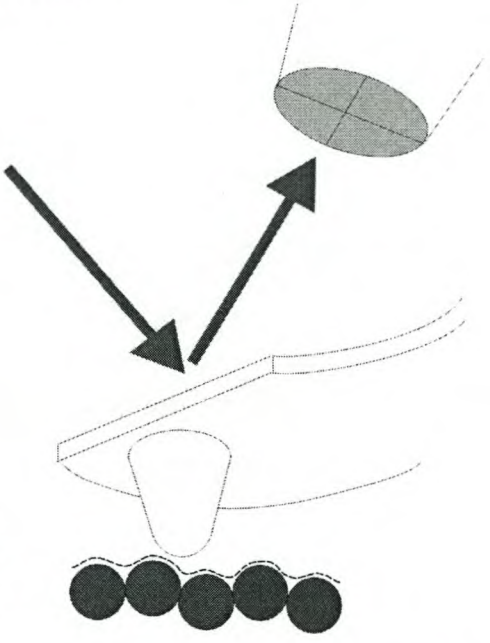

Figure 3.1: Schematic representation of an SPM probe, mounted on a cantilever, scanning over a surface and detecting the interaction force at each point.

In the constant force mode the interaction force between the probe and the sample is kept constant while the probe is scanned across the surface. This can be accomplished by using a feedback loop that keeps a constant cantilever deflection by compensating the z-position with the z-piezo crystal. Figure 3.2 displays a schematic feedback circuit to keep the force acting on the probe constant, so that the tip "follows" variations in the surface topology.

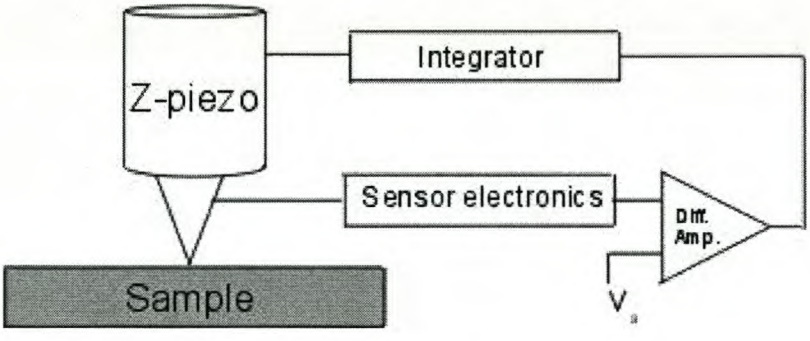

Figure 3.2: Schematic feedback circuit of the Atomic Force Microscope.

The acquired three-dimensional topographic image displays for each point (x,y) on the surface a gray value z(x,y) between 0 and 255. This value represents the required voltage to keep the probe tip at a certain distance from the surface by adjusting the z-piezo. The resulting three-dimensional image represents the topography of the scanned sample area.

3.2 The Atomic Force Microscope (AFM)

As a topographic imaging technique, the AFM may be regarded as a stylus profilometer. Atomic resolution is obtained by reducing the contact force of a commercial profilometer (~ 10^{-4}N) to below 10^{-9}N. This is less than most interatomic forces and limits the tip-induced surface deformation. The resolution of the AFM depends strongly on the diameter of the tip scanned across the surface. The AFM tip is a non-conducting silicon tip and the detected forces are repulsive contact forces, and attractive and repulsive non-contact forces, such as van der Waals interactions.

In case of the AFM, where the interaction forces are the atomic forces between the probe and the tip, the resulting image represents in fact a picture of the total charge density of the surface atoms. The corrugation of the surface can be modeled from this data by regarding the atoms as hard spheres in contact with each other.

3.2.1 Force Distance Relationship

As the AFM tip is brought closer to the sample, it experiences an attracting force. A variety of long-range attractive forces, such as van der Waals forces, electrostatic or magnetostatic forces are at work. When the probe gets very close to the surface, the electron orbitals of the surface atoms start to repel each other. As the gap decreases, the repulsive forces neutralize the attractive forces and become dominant. Figure 3.3 displays the forces acting between the tip and the sample, as a function of the distance between the tip and the sample.

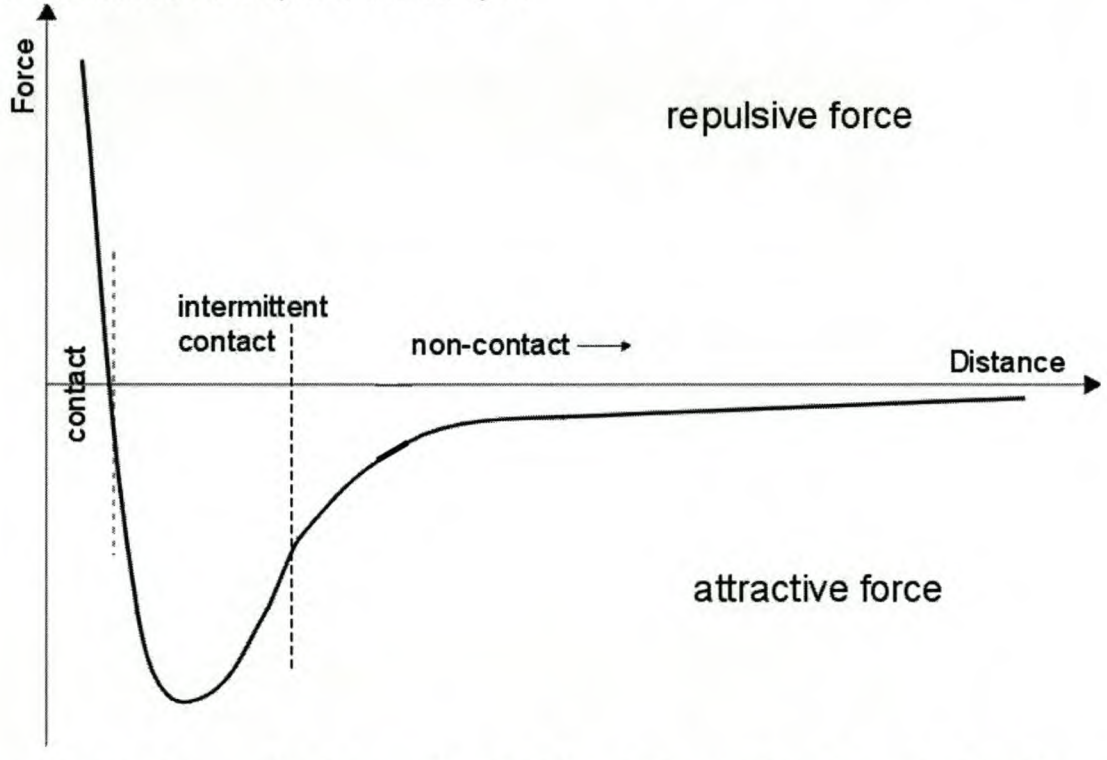

Figure 3.3: The forces acting between the AFM tip and the sample surface and the regions of the different scanning modes [8].

Depending on the distance between tip and sample the operation modes of the AFM are called contact or non-contact mode.

3.2.2 Contact Mode

In the contact mode the tip is close to the surface, so that the atomic forces acting between tip and sample are repulsive.
The contact forces used for imaging surfaces should be small enough to ensure that the sample is not disturbed. The bonding of atoms at surfaces may involve either strong ionic forces, medium-strength covalent bonding forces, or weak van der Waals forces. The magnitude of these forces can be estimated by considering a typical potential energy function of an interatomic bond. The ionic bonding energy can be estimated as $U_{ion} \leq 10eV$ and the van der Waals bonding energy as $U_{vdW} \leq 10meV$ [9]. Considering the repulsive contact forces acting through a distance of $\Delta x \approx 0.2Å$, the interatomic force, $F = -\Delta U/\Delta x$, would be $\leq 10^{-7}N$ for ionic bonds and $\leq 10^{-11}N$ for van der Waals bonds. These forces are also consistent with typical vibrational frequencies of a typical molecule:

$$\omega = \sqrt{\frac{k_{bond}}{m_a}} \tag{3.1}$$

where k_{bond} is the interatomic force constant and m_a is the atomic mass.

These estimates define the requirements for the force imparted by the tip, i.e. the force constant of the cantilever. With a force constant of 0.1N/m, even a 10nm loading deflection creates a force of $<10^{-9}N$. The first AFM cantilever, constructed by Binning et al., used a diamond chip attached to a 0.8mm x 0.25mm x 25µm gold foil. The spring constant was ~0.01N/m.
A softer cantilever imparts less force for a given deflection on the sample. However, to maintain a high resonance frequency, a reduction in the force constant must be coupled with a reduction in mass to preserve the k/m ratio.
Silicon device technology has introduced micro fabrication techniques to produce silicon, silicon oxide, or silicon nitride micro cantilevers of extremely small dimensions on a µm scale. Recent cantilevers have, for example, dimensions of 220 x 40 x 8 µm with a force constant of 30-70 N/m and a resonance frequency of 150 to 200 kHz [10].

Considering the discussed forces, measuring a very small cantilever deflection is crucial for a high-sensitivity force measurement.
In contact mode, the measurement of the cantilever deflection is performed directly as the tip is scanned over the sample surface. The AFM can also image and measure long-range interactions such as van der Waals, electrostatic [11] and magnetostatic [4] forces, with the tip scanning at relatively large distances from the sample surface by non-contact imaging [12].

3.2.3 Non - Contact Mode

In this mode the lateral resolution is substantially decreased compared to the contact mode, but the damage to the sample surface is considerably smaller.
The detected forces are rather small. At typical tip-sample separations of 10–100 nm the forces are smaller than 10^{-10}N; this is much smaller than the repulsive contact force.
Measuring these forces and their deviations requires instrumental sensitivities as high as 10^{-13}N and even higher. Such performance can only be obtained with resonance enhancement techniques.

The cantilever is driven at (or near) its resonance frequency by piezoelectric elements. Immersion in a force field results in a deviation of the resonance frequency. This deviation can be detected by measuring the changes in an observable parameter of the mechanical system, i.e. the shift of the resonance frequency, the change in amplitude at a fixed frequency, or a phase shift. The resonance frequency of an oscillating cantilever is given by:

$$f_r = 2\pi\omega = 2\pi\sqrt{\frac{k}{m}} \tag{3.2}$$

In order to illustrate the non-contact technique, a cantilever with the force constant k is considered. This cantilever is oscillating at its resonance frequency $\omega_0 = (k/m_{eff})^{1/2}$, by a piezoelectric transducer. The effective mass m_{eff} depends on the mass distribution and geometry of the tip/cantilever assembly. If the tip is placed in a force field f, the force constant k changes to:

$$k' = k - \frac{\partial f}{\partial z} \tag{3.3}$$

where $\partial f/\partial z$ is the force gradient in z direction and z is the vertical separation between the tip and the sample surface. The negative sign signifies an attractive force. The effective force constant is lower than for the free cantilever, thereby reducing the resonance frequency to:

$$\omega_0' = \sqrt{\frac{k'}{m_{eff}}} > \omega_0 \tag{3.4}$$

The typical equation of motion for a driven oscillator, with an external driving force f is:

$$m\frac{\partial^2 z}{\partial t^2} + \gamma\frac{\partial z}{\partial t} + k(z-u) = f(z-g) \tag{3.5}$$

In this expression γ is the damping term, with $\gamma = m\omega_0/Q$, and Q is the quality factor of the cantilever. u is the position of the undeflected cantilever, g is the sample position and z is the position of the deflected cantilever.

The most common method for measuring the force gradient and the forces of a particular tip-sample separation over one spot on the sample, is to drive the cantilever at its resonance frequency ω_0 and to monitor the reduction in the vibration amplitude $A(\omega_0,z)$ due to the shift in the resonance frequency of the system. Far away from the surface (beyond the interaction distance), the function $A(\omega,z)$ can be described by a Lorentzian function:

$$A(\omega,\infty) = A_0 \frac{\omega_0}{\omega} \frac{1}{\sqrt{1+Q^2(\frac{\omega}{\omega_0}-\frac{\omega_0}{\omega})^2}} \tag{3.6}$$

When the tip interacts with the surface, the amplitude of the cantilever can be written as:

$$A(\omega,z) = A_0 \frac{\omega_0'}{\omega} \frac{1}{\sqrt{1+Q^2(\frac{\omega}{\omega_0'}-\frac{\omega_0'}{\omega})^2}} \tag{3.7}$$

This measured amplitude can be used to calculate the new resonance frequency ω'_0. This in turn is directly related to the force gradient at the particular location above the sample by equation 3.8:

$$\frac{df}{dz} = \sqrt{m_{eff}(\omega_0^2 - \omega'^2_0)} \tag{3.8}$$

The force can be deduced by measuring the amplitude, calculating the new resonance frequency and the force gradient as a function of z and then integrating df/dz.

Sources of noise emanate from optical and thermal contributions. Optical noise is induced by the photons of the laser, inducing a pressure on the cantilever, which is negligible. The noise force due to a 1mW beam is of the order of 10^{-19}N. The thermal noise presents a more serious limitation. The thermal energy excites the cantilever to a vibration of the amplitude $A_T = (2k_BT/k)^{1/2}$ and a vibration noise $N = (4k_BTQB/k\omega_m)^{1/2}$, at a frequency ω_m and in a bandwidth B [4],[13]. The smallest detectable force gradient f'_m is found by setting $\Delta A=N$ and with the approximation $\omega_0=\omega_m$:

$$f'_m = \frac{1}{A_0}\sqrt{\frac{27k_BTB}{Q\omega_0}} \tag{3.9}$$

Thus, several parameters can be optimized in order to maximize the sensitivity of the AFM:

- Decreasing the cantilever stiffness k. The lower value is limited by the maximum tolerable thermal noise vibration A_T, which varies as $k_B^{-1/2}$.
- Increasing the quality factor Q. Q depends strongly on the quality of the mechanical connection between the cantilever and the piezoelectric transducer.
- Increasing the vibration amplitude A_0 and the natural resonance frequency ω_0 of the cantilever.

Besides contact and non-contact imaging, the AFM can be used as a nanoscale surface force apparatus to measure adhesion between materials and the indentation /deformation properties of surfaces under extremely small loads [14]. The atomic scale basis of friction – nanotribology – can also be studied with a modified AFM by sliding a lightly loaded tip along the surface and measuring the lateral resistance to the motion [15].

3.2.4 Resolution and Artifacts

The resolution of the SPM in each of the three dimensions is limited by different factors.

The resolution in the z direction is limited by the level of vibrations between the probe and the surface and the sensitivity of the control electronics. It is possible to get an Ångstrom resolution in the z-direction.

The maximum achievable resolution in the x-/y- plane is established by the geometry of the probe. When imaging extremely flat surfaces, the resolution is only limited by the diameter of the atom(s) at the probe's tip. When scanning rougher surfaces, the resolution is limited by the aspect ratio a = L/W of the tip (L: length of tip, W: average diameter of the tip). Figure 3.4 illustrates the artifacts due to the probe geometry. At the step the probe and the sample interact before the tip of the probe reaches the step. In the resulting image the step appears wider than it really is and the edges are rounded.

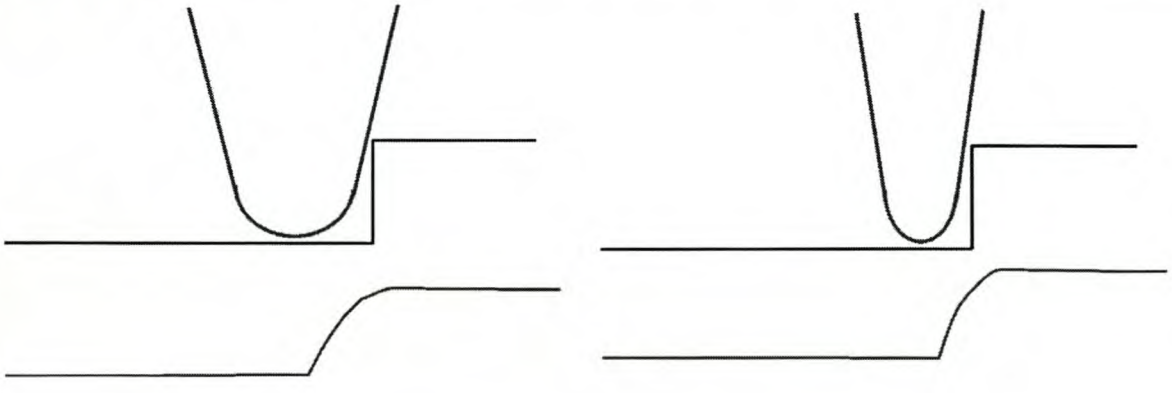

Figure 3.4: Imaging artifacts for tips with different aspect ratio. Due to the probe geometry, the edges appear rounded and image the tip as well as the sample topography.

Higher aspect ratios will result in images that more closely represent the shape of the surface. The probes manufactured by Nanosensors have a pyramidal shape with tip radii of about 10 nm, a mean width of typically 40 μm and a length of about 220 μm, which leads to a fairly high aspect ratio of 5–6. Figure 3.5 displays a SEM image of a silicon Pointprobe manufactured by Nanosensors.

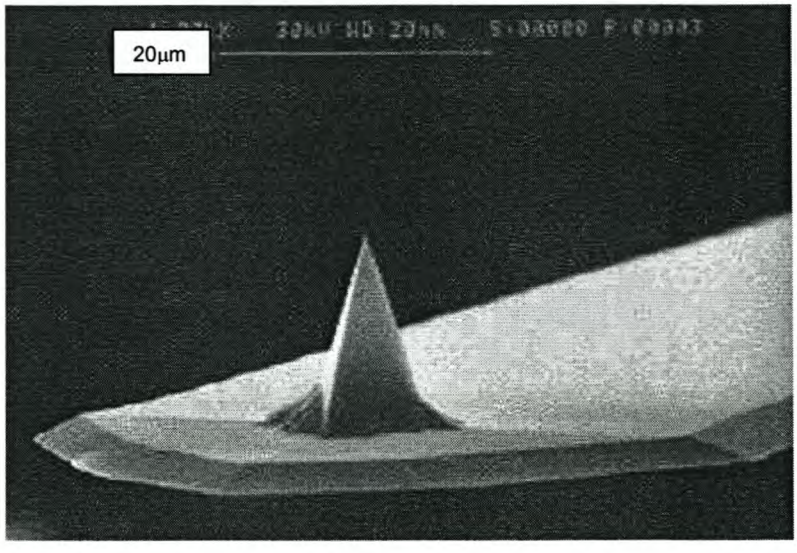

Figure 3.5: SEM image of a Pointprobe silicon cantilever with silicon tip.

The resolution is also influenced by the sample surface itself. Under ambient conditions it will have a thin contamination layer, composed of water and other ambient contaminants. As the probe moves towards the sample surface, it will be pulled towards the surface due to attractive capillary forces.
The shape of the tip is also important for the resolution of the image, since the image is the result of the sample surface and the probe shape. A dull, large radius, low aspect ratio tip will have a large area interacting with the contamination layer of the sample, resulting in strong attractive forces. A sharp, small radius, high aspect ratio probe will have a much smaller area that interacts with the contamination layer. The wetted area of the tip is smaller therefore it can be moved in and out of this layer more easily.

3.3 The Scanning Thermal Microscope (SThM)

In the SThM, the tip is replaced by a thermal probe. This can be a thermocouple [16-18] or a resistive element [19,20]. The resistive thermo-probe is a bent Wollaston wire, that is etched back to its platinum core at the tip. This platinum core forms a resistive element that is scanned over the sample surface in the conventional AFM contact mode. Using this sensor, it is possible to obtain simultaneous images of the

topography and the heat conductivity or the temperature of the sample. Figure 3.6 illustrates a Thermal Probe.

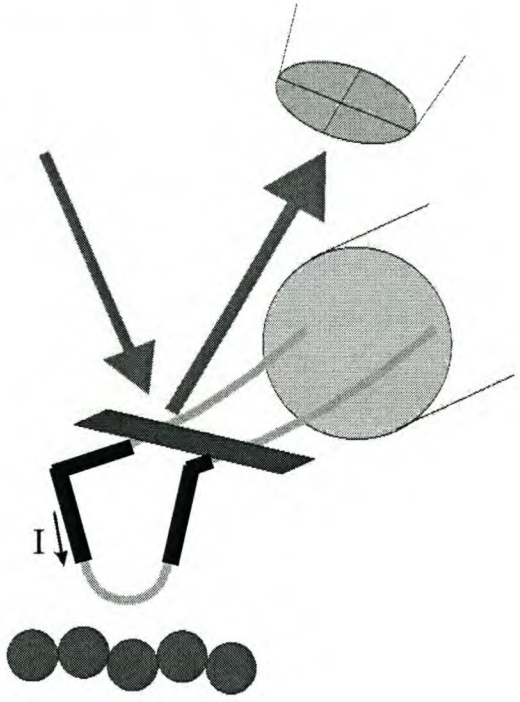

Figure 3.6: Schematic illustration of a thermal probe.

The dimensions of the wire loop at the tip are about 5μm in diameter, but the effective contact area on a flat surface is about 30 to 300nm. This still leads to a fairly good lateral resolution.

The probe can be used to map the surface temperature of the sample or to measure the heat conductivity. If the temperature is monitored, the tip is scanned in the contact mode across the surface to maximize the heat transfer between the sample and the tip. The constant current through the platinum wire is small to prevent self-heating.
As the probe is scanned across a surface with temperature variations, the temperature dependent resistance of the platinum wire will change according to:

$$R = R_0(T-T_0)\alpha+1 \qquad (3.10)$$

where T is the temperature of the sample surface, and R_0 the resistance of the wire at the reference temperature T_0. The temperature coefficient α of platinum is $3.9\text{x}10^{-3}$ 1/K.

If the current through the wire is large enough to heat the tip, the heat capacity of the sample can be measured. Depending on the temperature of the sample, a heat flow occurs from the probe into the sample surface and leads to a change in the temperature and with it the resistance of the platinum wire, depending on the thermal conductivity of the sample.

To measure the resistance through the platinum wire, the probe is used as one of the legs of a Wheatstone bridge, as displayed in Figure 3.7.

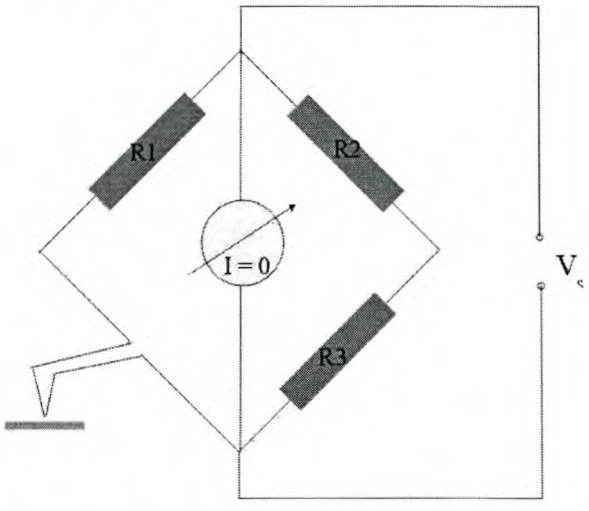

Figure 3.7: Measurement principle of the SThM. The change in resistance is measured with a Wheatstone bridge.

The supply voltage is adjusted so that the bridge remains balanced. If the thermal probe is cooled and the resistance changes, the supply voltage will be increased to compensate this and to equalize the bridge again. If the contact area between the tip and the sample, and the temperature difference between tip and sample are constant, the change of the supply voltage of the Wheatstone bridge will be directly proportional to the local heat capacity of the sample.

In order to increase the sensitivity of the system, the signal is modulated with alternating voltage. This creates an alternating output signal, which is fed into a Lock-In amplifier. Due to its phase sensitive amplification, the Lock-In amplifier measures any deviation from the bridge balance with increased sensitivity. From this the resistance of the probe can be calculated. In this mode the bridge is not equalized; the output signal is the deviation from the bridge balance.

3.3.1 Micro Thermal Analysis (μTA)

The μTA [21] uses an SPM with a thermal tip. The probe can be placed at different points on the surface and perform localised thermal analysis at these points.

The temperature of the tip is ramped linearly at rates of some K/s. Heat is transferred from the tip into the sample and the sample is heated in this way. At the same time the laser deflection of the cantilever is measured during heating, thus recording the expansion or contraction of the sample.
Information on surface expansion, film thickness, glass transition temperatures, hardness changes, softening and melting processes can be determined from these plots.

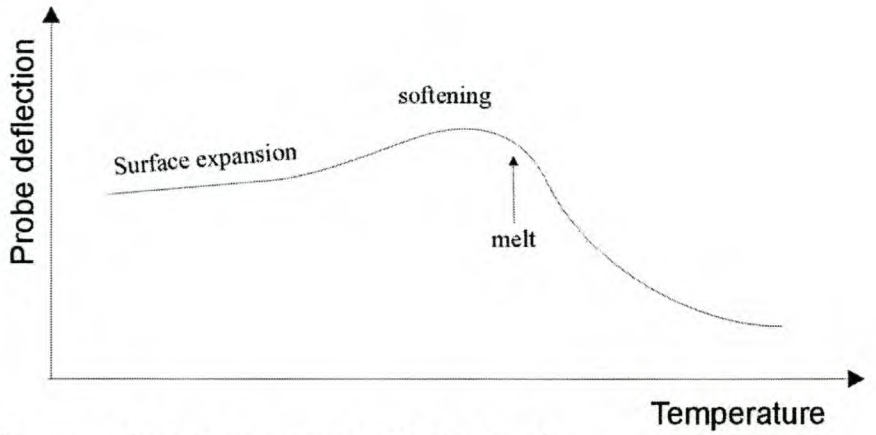

Figure 3.8: μTA curve of a polymer recorded during heating.

While the sample softens and expands three-dimensionally as the temperature is increased, the tip follows the "upwards" movement and the cantilever is bent. Close to the melting point the polymer becomes softer and the tip indents the sample.

The disadvantage of this method is that the thermal probe is always in contact with the sample surface and is therefore destroying, or at least disturbing, the surface. The tip may also be contaminated with polymer, thus affecting the heat conductivity and the heat transfer from the tip to the sample.

3.4 Thermal Analysis of Polymers by AFM

To measure thermal parameters of a polymer such as T_g or T_m in an entirely non-destructive way, and to prevent any contamination of the tip, a new method has been developed in this thesis to use the AFM as a "NanoDMA". The idea is to use the AFM in the same way as a DMA, but on a much smaller scale, to excite molecules mechanically and measure their response. In this way it should be possible to determine thermal transitions of polymers on a molecular scale and thus determine the thermal parameters of different polymer phases in close proximity to the tip.
Unlike the μTA, a normal non-contact tip can be used instead of a thermal probe. Another difference is that the entire sample is heated, not only a part of it.

The instrument is used in the non-contact mode with a non-contact tip. In this mode the tip is not used to scan the sample surface, but rather to probe at one point of the surface and measure the properties at that specific point. In order to prevent any contamination, the tip is kept at a fairly large distance of about 20 μm from the surface. The cantilever oscillates above the polymer surface and thus excites the underlying molecules. Depending on their degree of freedom, the molecules can respond to this excitation and cause a change in the characteristic behavior of the cantilever.

A simple hydrodynamic model was derived from Cichacki et al. [22] to describe the amplitude, resonance frequency and damping of the oscillating cantilever as a function of the tip/sample distance far away from the sample surface.
In this model, which is a great simplification but sufficient for estimations, the cantilever is regarded as an oscillating sphere with the radius r in a liquid with the viscosity η at a distance d from the sample surface. The eigenfrequency of the oscillating sphere is ω_0, the frequency of the driving force F is ω.

The equation of motion of the system can be expressed as:

$$\gamma \frac{dz}{dt} = F(t) \tag{3.11}$$

where γ is the damping factor, given as

$$\gamma = \frac{6\pi\eta r}{X_1 + X_2\, r/d} \tag{3.12}$$

and the external driving force $F(t) = -A_0\sin(\omega-\omega_0)t$ with the drive amplitude A_0. X_1, X_2 are fit factors, containing all other constant values.

The differential equation of motion can be solved by inserting eq. 3.11 into the equation for a driven oscillator, with the external driving force A(t):

$$\frac{d^2x}{dt^2} + 2\gamma\frac{dx}{dt} + \omega^2 x = A(t) \tag{3.13}$$

with the solution:

$$x = \frac{A_0}{\sqrt{(\omega^2 - \omega_0^2)^2 + 4\gamma^2\omega^2}}\cos(\omega t - \delta) \tag{3.14}$$

The amplitude in expression (3.14) has a maximum when $\cos(\omega t-\delta) = 1$:

From this the resonance frequency can be derived as: $\omega_r^2 = \omega_0^2 - 2\gamma^2$ (3.15)

and the maximum amplitude is given by: $$A_{max} = \frac{A_0}{2\gamma\sqrt{\omega_0^2 - \gamma^2}} \tag{3.16}$$

The experimentally determined values of the resonance frequency ω_r and the amplitude of the cantilever A_{max} measured isothermally at different distances between the tip and a metal surface could be fitted well with equations (3.15) and (3.16), as displayed in Figure 3.9.

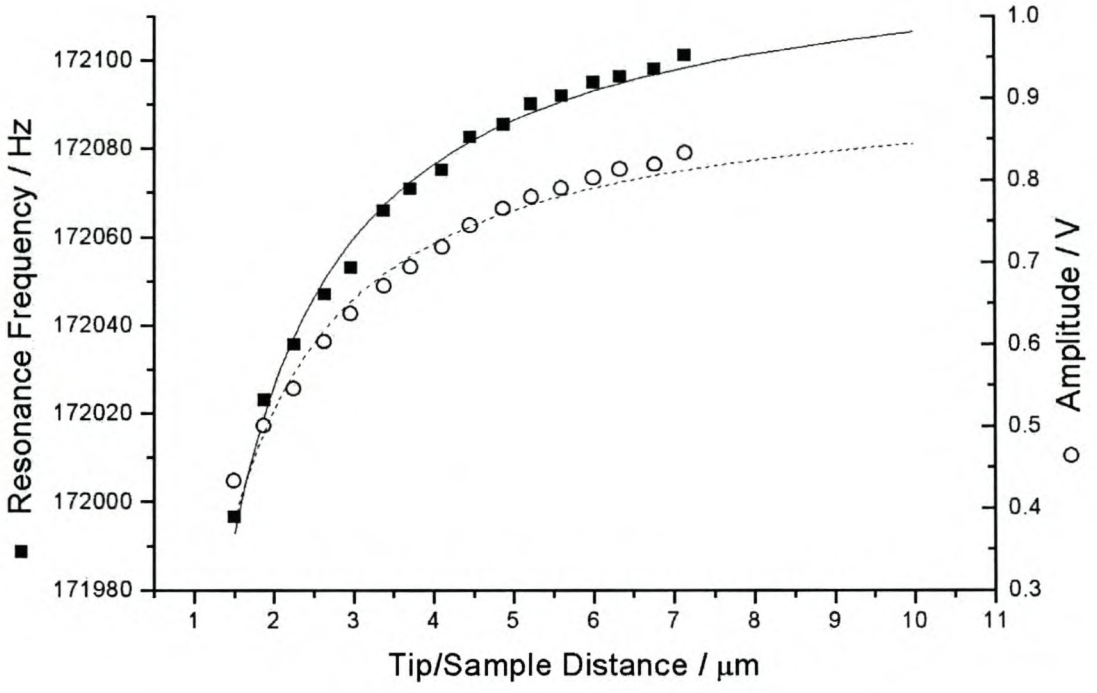

Figure 3.9: Change of the resonance frequency and the amplitude of the oscillating cantilever as a function of the cantilever/sample distance. The measured values fitted the theoretical model well.

The diameter of the sphere r was assumed to be the width of the cantilever (≈ 20μm) and the distance h was changed within the limits of the piezo crystal moving the cantilever in z-direction. The z-piezo of the 100μm scanner has a z-range of 7.5 μm by applying a voltage between 0 and 100 V. The eigenfrequency ω_0 of the cantilever is given by [10]:

$$\omega_0 = 0.162\sqrt{\frac{E}{\rho}}\frac{T}{L^2} \tag{3.17}$$

and is about $\omega_0 \approx 190.4$ kHz.

For distances greater than 10 μm, the change in resonance frequency and amplitude become very small and hardly recognizable. This means a slight variation in the distance does not cause a great change in the resonance frequency or the amplitude of the oscillating cantilever.

3.4.1 The Interaction Mode

The interaction between a polymeric sample and the cantilever is influenced by two factors:

1) the distance between the sample and the tip
2) the viscoelastic properties of the polymer, particularly the storage and the loss modulus.

A decrease in distance between the sample and the tip results in a decrease of the resonance frequency, as explained in the previous section. The resonance frequency of the cantilever was measured as a function of the temperature. As the temperature increases, all materials with the original length L and the material constant α are expanding linearly, according to $L = \alpha * T$.
The length of the cantilever will thus increase, resulting in a decrease of the resonance frequency ω_r of the cantilever, hence an increase in temperature results in a shift of the resonance frequency towards lower values according to

$$\omega_r \sim \sqrt{\frac{E}{\rho}\frac{D}{L^2}} \tag{3.18}$$

Where E is the elastic modulus, ρ the density, D the diameter and L the length of the cantilever as given by the manufacturer [10]. D and L are increasing linearly with temperature, so the ratio D/L^2 results in a linear decrease of the resonance frequency.

Simultaneously, the thermal expansion of the heating stage leads to a decrease in the distance between the tip and the sample surface, and therefore to a slight decrease in the resonance frequency. Due to the large distance between cantilever and sample this effect can be neglected (see Figure 3.9), unless the distance decreases rapidly, like at the melting point.

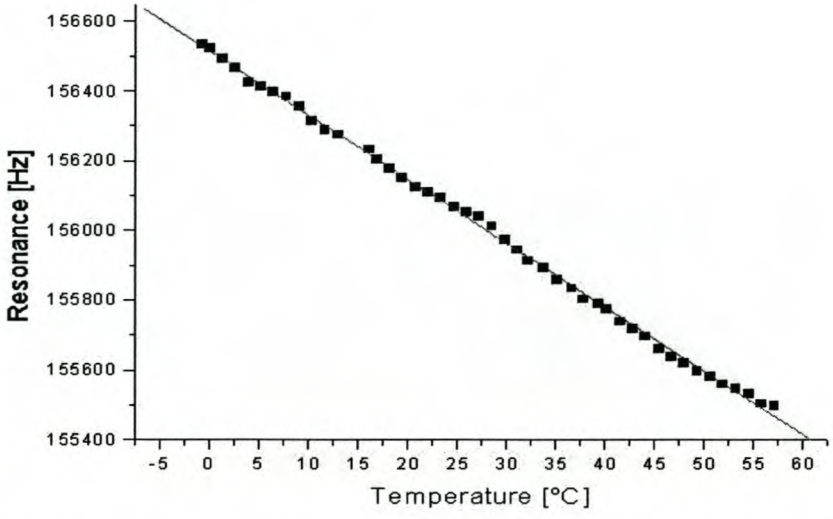

Figure 3.10: Resonance frequency of the AFM cantilever as a function of temperature (this study).

The frequency plot of the cantilever as a function of the temperature is a linearly decreasing function, as shown in Figure 3.10. The gradient depends only on the material characteristics of the cantilever and the expansion coefficient of the heating stage. The characteristic form of the frequency curve changes if the AFM probe is placed above a polymer, which is heated from the below.

3.4.2 The Melting Point

At the melting point, the volume of the polymer increases drastically since the polymer chains are now able to move freely. The increase in volume leads to a decrease in the distance between the AFM tip and the surface and therefore to a sharp decrease in the resonance frequency of the cantilever.

The melting point of a polymer appears as a sharp kink in the resonance plot, as displayed in Figure 3.11:

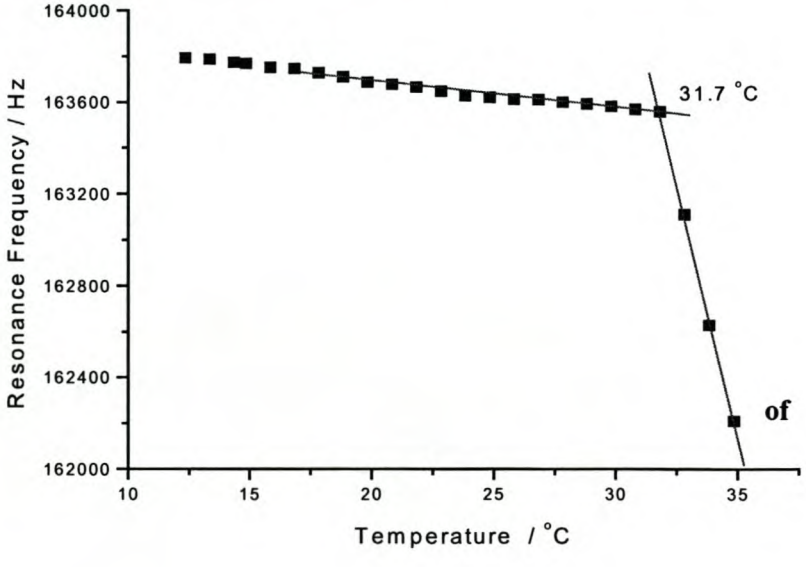

Figure 3.11: The melting point of octadecane at 31.7°C appears as a sharp kink (this study).

3.4.3 The Glass Transition

The free volume expansion of second order transitions is several orders of magnitude smaller than at the melting point, and is in fact a change in the expansion coefficient and not a distinct volume expansion. The glass transition is not even a real second order transition - it is characterized by a change of the viscoelastic properties rather than a change in volume. The change in free volume is just enough to allow the movement of the polymer chains.
The clearly visible transition in the frequency plot can therefore not be explained by a change in the free volume of a polymer. The glass transition appears as a plateau (region 2) in the frequency plot, as shown in Figure 3.12. The curve represented by the black squares represent the measured frequency shift, with a plateau around the glass transition temperature of the polymer.
If the decreasing linear function (region 1 and 3) given by the cantilever characteristics and thermal expansion, is used as a baseline and subtracted from the entire curve, the frequency shift results in the curve represented by the hollow circles. It then becomes visible that the glass transition is in fact represented by an increase in the resonance frequency.

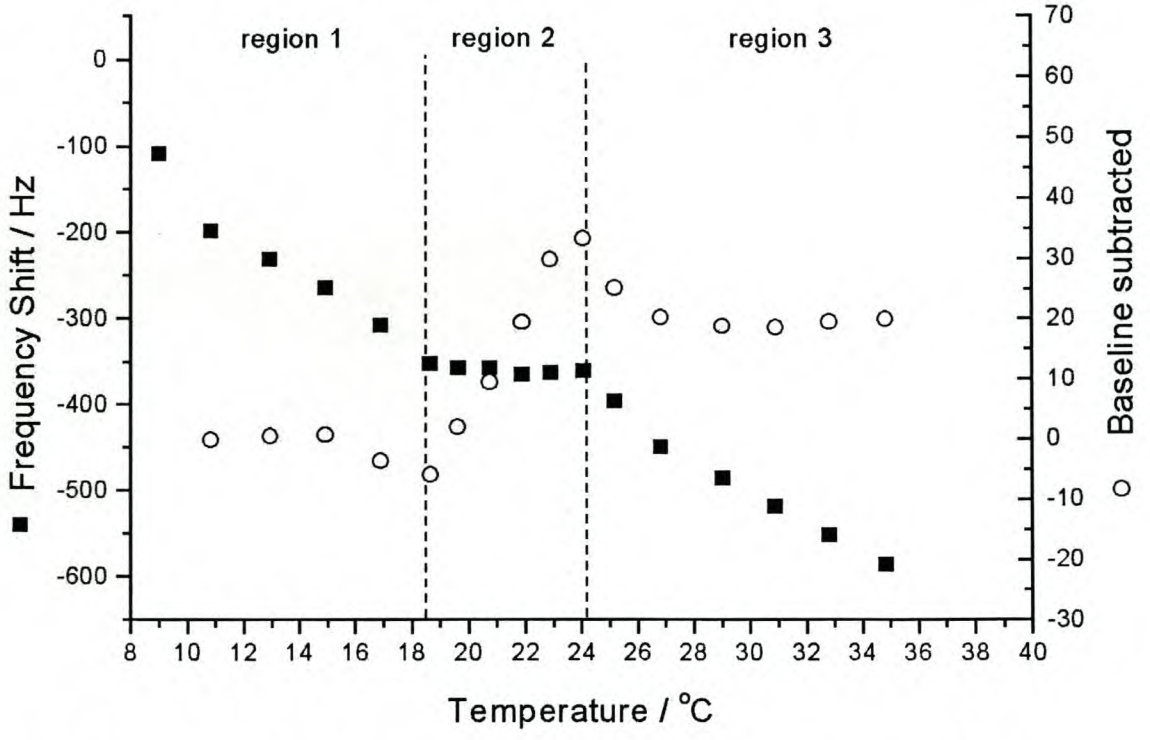

Figure 3.12: Glass transition of a random copolymer with a T_g of about 21°C (this study).

A model has been developed to describe this behavior of the cantilever by taking the viscoelastic properties of the polymer into account.
The oscillating cantilever generates a pressure wave or a sonic wave, transporting energy through the air molecules. Air is needed as a transport medium between the

cantilever and the polymer, as can be seen in Figure 3.13. The plateau, indicating the glass transition of the polymer, becomes smaller and eventually disappears with decreasing pressure. The slope of the resonance curve is also decreasing.

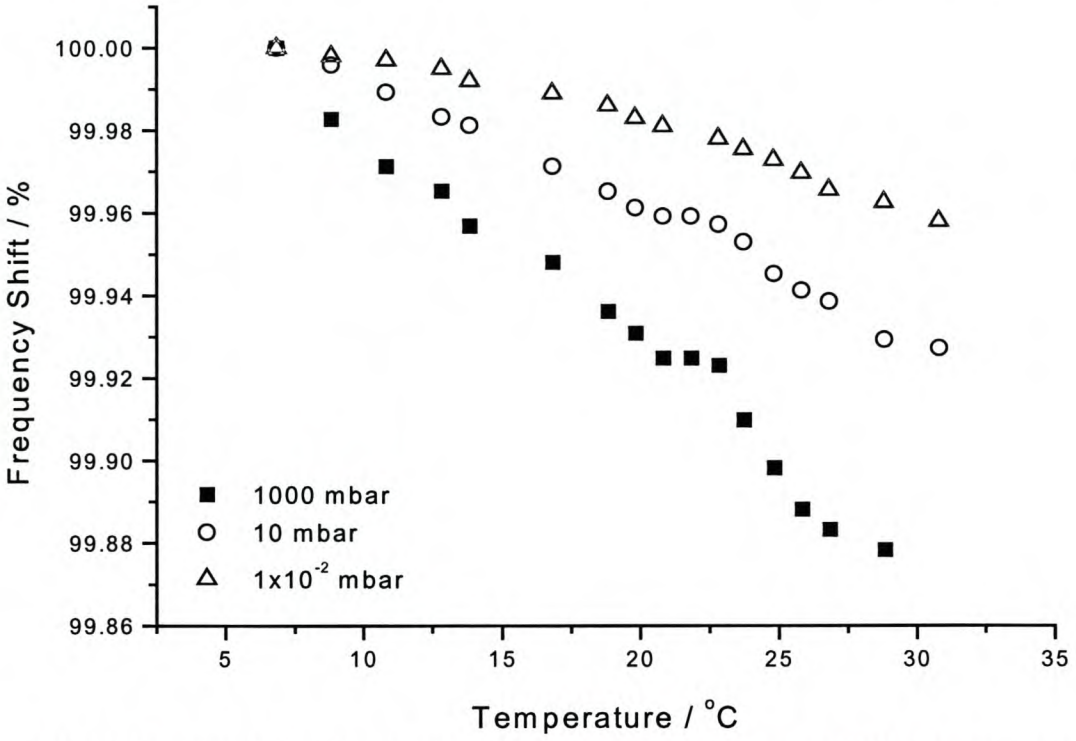

Figure 3.13: Resonance frequency as a function of the temperature at different pressures (this study).

The pressure wave generated by the oscillating cantilever is partly reflected at the air/polymer interface and partly absorbed by the polymer. Since the cantilever and the sample are most likely not perfectly aligned, the pressure wave will also have a transverse component. If a shear wave with the oscillation direction parallel to the interface is reflected at the air/polymer interface at normal incidence, the complex reflection coefficient r* is expressed by [23]:

$$r^* = \frac{Z_p^* - Z_a^*}{Z_p^* + Z_a^*} \tag{3.19}$$

where Z_p^* and Z_a^* are the imaginary acoustic impedance of the air and the polymer respectively and $Z^{*2} = \rho^2 G^{*2}$ [24]. The impedance of air is much smaller than that of the polymer, so Z_a^* can be replaced by the real part Z_a with $Z_a = (\rho^* G)^{1/2} = (\rho^* \eta^* \omega)^{1/2} \approx 1944\ \mathrm{kg/(s*m^2)}$.
The absorption coefficient a^* is given by:

$$a^* = 1 - r^* \tag{3.20}$$

At the glass transition a^* and r^* change significantly, as displayed in Figure 3.14.

The reflection and absorption curves have been calculated from the complex shear modulus G^* of polymethylmethacrylat acid (PMMA) determined by DMA measurements. In this example the onset of the decrease in the shear modulus was regarded as T_g.

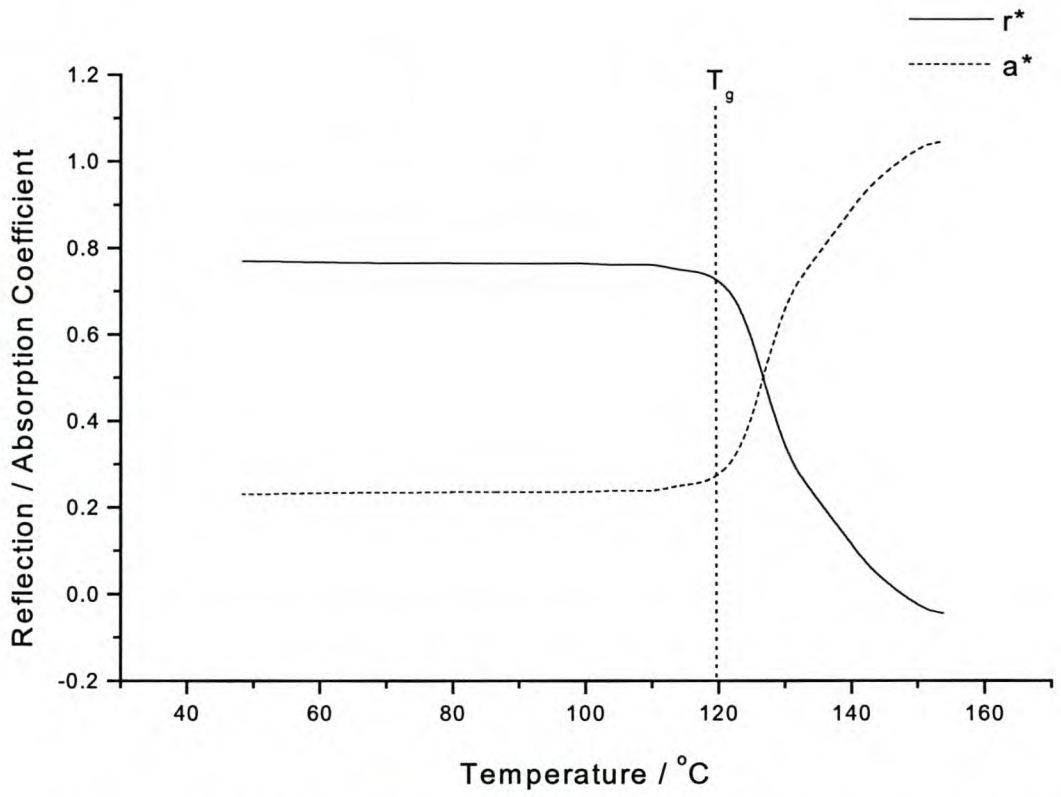

Figure 3.14: Reflection and absorption coefficient of PMMA at the air/polymer interface (this study).

The absorption coefficient increases at the glass transition, because the polymer chains are now able to absorb energy, due to the free volume that is created at T_g, and convert it into kinetic energy. This can also be seen in the loss modulus G", which reaches a maximum after T_g and is a measure for the damping of the polymer. In the glassy state the surface is obviously harder and the pressure waves are reflected to a greater extent.
The reflected wave, or rather the moving air molecules, hinders the oscillating cantilever and thus leads to a further decrease of the resonance frequency. This effect must be added to the effect of thermal expansion. At the glass transition the reflected energy decreases because more energy is now absorbed by the polymer due to the increase in free volume and the ability of the molecule chains to move. The cantilever is now less hindered by the air molecules and can oscillate more freely closer to its eigenfrequency $\omega_0 \approx 190$ kHz. This is represented by the increase of the resonance frequency (or the plateau) around T_g. After further increase of a few degrees in temperature this effect slows down, because the absorption coefficient reaches its maximum value at the specific frequency of the cantilever. Other effects,

like the thermal expansion of the cantilever, start to dominate again. This leads to a further linear decrease in the resonance frequency like in region 1 before T_g.

The width of the plateau around T_g (region 2) seems to depend on the film thickness, which implies that this method shows a certain depth sensitivity. Obviously a thicker film contains more polymer layers. Thus more absorbed energy can be converted into kinetic energy for chain movement at temperatures above the glass transition.
Since the glass transition is lowered at the surface as described in chapter 1.1.4.2, the absorption coefficient should start to increase when the surface chains are able to move, thus allowing the cantilever to oscillate more freely. At the same time the resonance frequency stops decreasing. The absorption coefficient would then increase further at higher temperatures once the bulk chains can start moving as well. This continues until the saturation value is reached and the amount of reflected energy stays constant. From this temperature onwards the resonance frequency starts decreasing again, because the effect of increased energy absorption by the polymer is superposed by the thermal expansion of the cantilever and the sample.

Experimental results in chapter 6 show, that the resonance frequency method of the AFM is not only surface sensitive in determining thermal parameters, but also slightly depth sensitive to some underlying polymer layers.
The AFM resonance frequency method shows the glass transition over a temperature range of a few degrees, starting at the lowered value for the surface T_g followed by the higher bulk value of T_g. This results in a plateau over a certain temperature range T which width depends on the film thickness.
These findings agree well with the theory of a lowered glass transition at the surface, as described in chapter 1.1.4.2.

3.5 Bibliography

[1] Binning,G., Rohrer,H., Gerber,C., Weibel,E., *Physical Review Letters*, 1983, **50**, 120
[2] Binning,G., Quate,C., Gerber,C., *Physical Review Letters*, 1986, **56**, 930
[3] Martin,Y., Williams,C., Wickramasinghe,H., *Physical Review Letters*, 1986, **56**, 930
[4] Martin,Y., Williams,C., Wickramasinghe,H., *Journal of Applied Physics*, 1987, **61**, 4723
[5] Fischer,U., Pohl,D., *Physical Review Letters*, 1989, **62**, 458
[6] Balk,L., Cramer,R., Fiege,G., *International Symposium on the Physical Failure Analysis of Integrated Circuits*, 1997, Singapore
[7] Stopka,M., Hadjiiski,L., Oesterschulze,E., Kassing,R., *Journal of Vacuum Science Technology B*, 19951, **13**, 2153
[8] Thermomicroscopes, *Technical Report, Thermomicroscopes*, 2000,
[9] Di Nardo,N., *Nanoscale Characterization of Surfaces and Interfaces*, chapter3, p. 118, *VCH*
[10] Nanosensors, *Nanosensors, product specification*, 2000
[11] Martin,Y., Abraham,D., Wickramasinghe,H., *Applied Physics Letters*, 1988, **52**, 1103
[12] Zhong,Q., Inniss,D., Kjoller,K., Elings,V., *Surface Science Letters*, 1993, **290**, 688
[13] Duerig,U., Gimzewski,K., Pohl,D., Schlitter,R., *Physical Review Letters*, 1986, **57**, 2403
[14] Rosa-Zeiser,A., Weilandt,E., Hild,S., Marti,O., *Measurement Science Technology*, 1997, **8**, 1333
[15] Overney,R., Buenviaje,C., Luginbuehl,R., Dinelli,F., *Journal of Thermal Analysis and Calorimetry*, 2000, **59**, 205
[16] Oesterschulze,E., Stopka,M., *Journal of Vacuum Science Technology A*, 1996, **14**, 1172
[17] Luo,K., Shi,Z., Varesi,J., Majumdar,A., *Journal of Vacuum Science Technology B*, 1997, **15**, 349
[18] Luo,K., Shi,Z., Lai,J., Majumdar,A., *Applied Physics Letters*, 1996, **68**, 325
[19] Mayes,A., *Macromolecules*, 1994, **27**, 3114
[20] Hammiche,A., Hourston,A., Pollock,H., Reading,M., *Journal of Vacuum Science Technology B*, 1996, **14**, 1486
[21] Pollock,H., Hammiche,A., *Journal of Physics D*, 2001
[22] Cichacki,B., Jones,R., *Physica A*, 1998, **258**, 273
[23] Alig,I., Lellinger,D., Sulimma,J., Tadjbakhsch,S., *Review Scientific Instrumentation*, 1997, **68**, 1536
[24] Tadjbakhsch,S., *PhD thesis, Technische Universitaet Darmstadt, Physik*, 1998,

CHAPTER 4: Experimental

In this chapter the experimental methods to characterize and synthesize the investigated polymers are described. The AFM was used as an imaging tool to monitor the kinetic drying and film formation processes of the polymers and as a probing tool to determine their thermal transitions.

4.1 Characterization Methods

The characterization of the investigated polymers was performed by various methods. The most important information of the latices required for this work were the glass transition temperature of the polymer and the particle size of the latex particles. The latter is presumed to affect the film formation behavior of an emulsion [1-5]. T_gs were obtained by Differential Scanning Calorimetry and Dynamic Mechanical Analysis. The particle size was determined by Photon Correlation Spectroscopy.

4.1.1 Differential Scanning Calorimetry (DSC)

The DSC [6,7] is constructed like a balance. It consists of two cells, one containing the sample and one acting as a reference cell, as can be seen Figure 4.1.

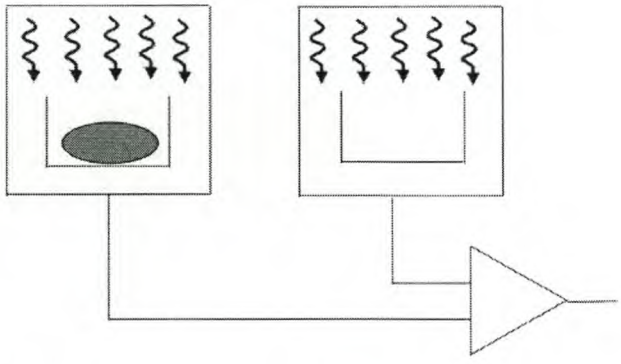

Figure 4.1: Schematic illustration of a DSC.

The difference in energy required to keep both chambers at the same temperature is measured. The energy absorbed or evolved by the sample is compensated by adding or subtracting an equivalent amount of energy to or from the reference cell.
Both cells are heated at a fixed rate from a starting temperature to a higher temperature. During heating any molecular changes, such as glass transition, melting or crystallization can be detected by a change in the enthalpy of the sample. Such changes can be exothermic (heat is given off) or endothermic (heat is absorbed), leading to an increase or a decrease in the temperature of the sample cell compared to the reference cell. The DSC will compensate for this temperature difference. This change of energy is detected by thermocouples and recorded as an energy difference on the thermogram. The resulting diagram shows the heat flow in mW or the derivative of the heat flow, the heat capacity in J/(g·K), as a function of the

temperature. If the heat flow is plotted against the temperature, a glass transition point appears as an inflection point and a melting point as a peak. If the heat capacity of the polymer is plotted as a function of the temperature, the glass transition appears as a peak and the melting point as a peak followed by a drop, as displayed in Figure 4.2.

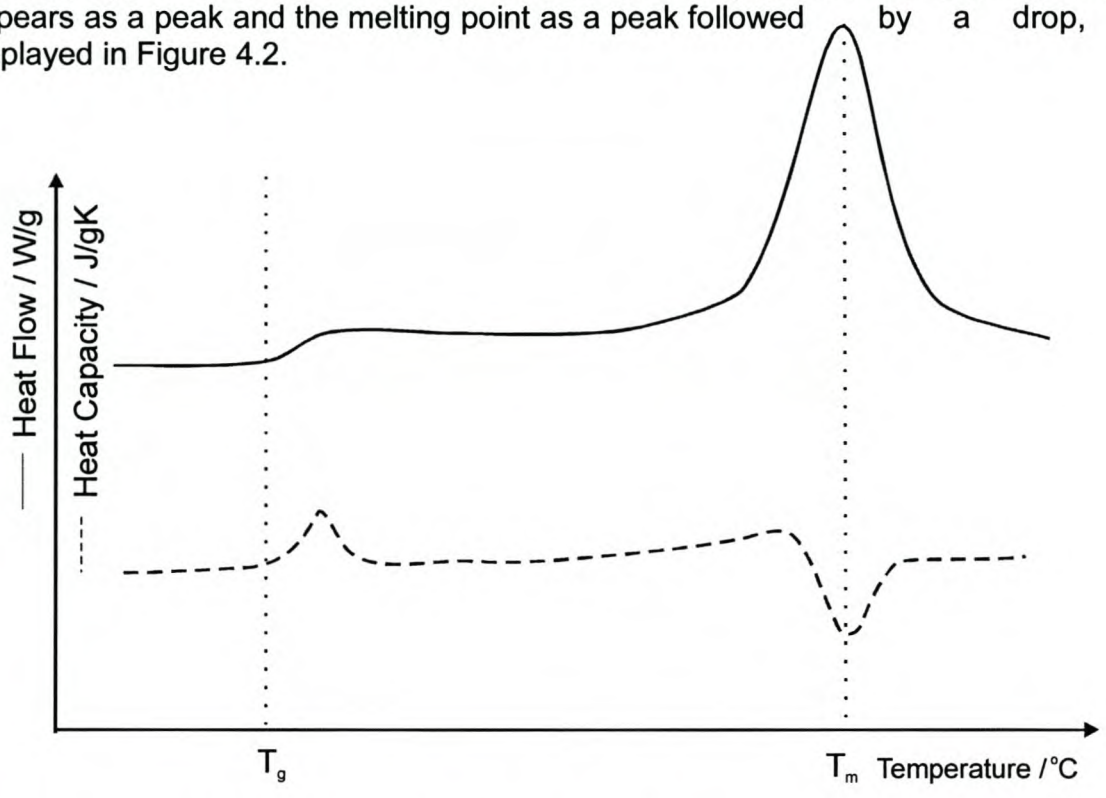

Figure 4.2: Resulting heat flow and heat capacity thermogram of a DSC experiment on a polymer sample.

The DSC measurements were carried out on a Perkin-Elmer DSC Pyris 1 at heating/ cooling rates of 10K/min. The curves of the first heating cycle were used for the analysis. Acquired data was processed with the Pyris software version 3.81.

4.1.2 Dynamic Mechanic Analysis (DMA)

The DMA [8] applies a periodical mechanical stress, for example elongation or torsion, to a sample and detects the mechanical response of the sample as a function of temperature or frequency (Figure 4.3). The resulting response curves give information about the viscosity of the sample. Measured are the storage modulus of the sample G' in Pa and the phase shift δ in response to the periodical excitation. The viscosity is $\eta = G'/\omega$.
Since the elastic properties change significantly at the glass transition and the melting point, the DMA is a useful tool to determine these thermal parameters.

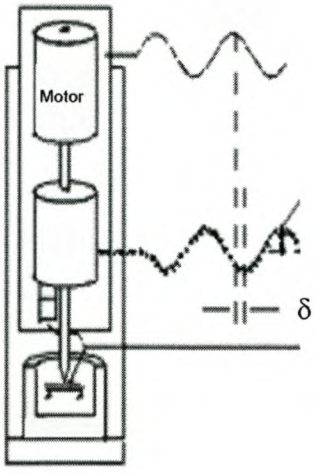

Figure 4.3: DMA measuring the storage modulus and the phase shift of a sample.

In the storage modulus the glass transition appears as an inflection point, sometimes preceded by a small hump. This hump corresponds to rearrangements of the molecules to relieve stresses frozen in below the T_g and depends on the processing method. The melting point appears as a sharp decrease of the storage modulus. In the phase plot T_g is indicated as the onset of the dampening peak and T_m as a sharp upward kink.

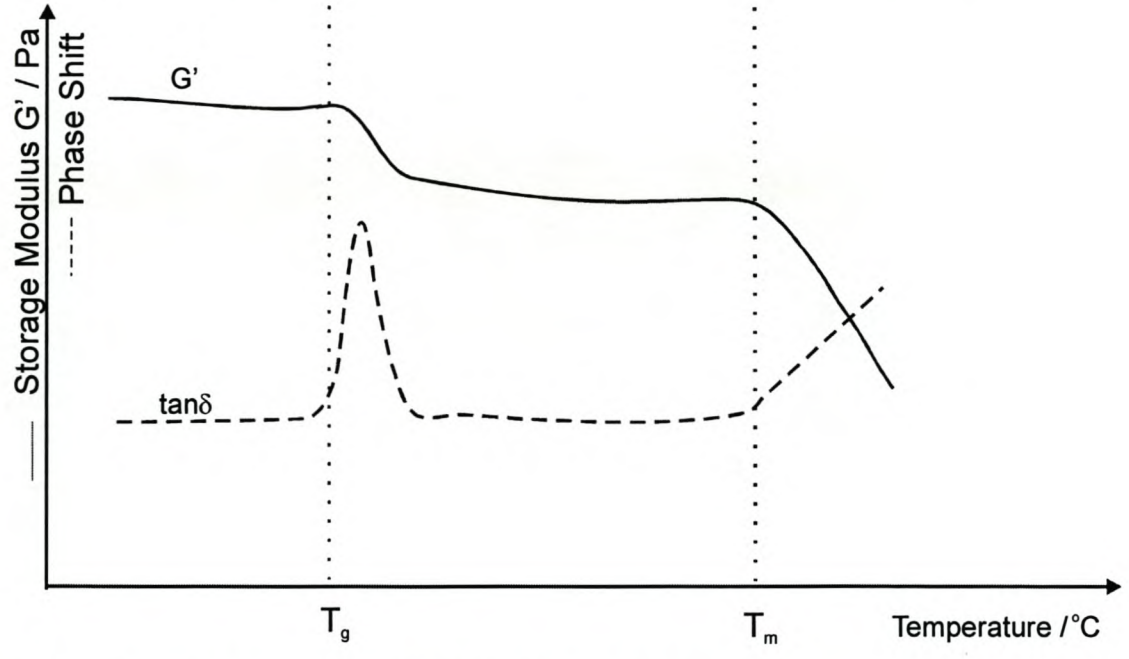

Figure 4.4: Typical response curves of a DMA for a polymer sample.

DMA measurements were performed on a Perkin-Elmer DMA 7e with heating and cooling rates of 5K/min. The acquired data was processed with the Pyris software version 3.81.

The disadvantage of both the DSC and the DMA is that it is not possible to measure thermal parameters locally. Both methods yield only an average value for the entire sample. It is thus not in general possible to measure thermal parameters of single polymer phases in, for example, blends or structured polymers.

4.1.3 Photon Correlation Spectroscopy (PCS)

The particle size of the latex particles was determined by PCS. PCS relates the Brownian motion of the dispersed particles at a known temperature to their particle size and delivers a particle size distribution with a standard deviation. The deviation shows how monodisperse or polydisperse the particles are.

Laser light is scattered by the particles. If the particle size becomes roughly equivalent to the wavelength of the light, the light then is not scattered isotropically, but becomes a complex distribution with maxima and minima at different angles. The PCS measures the scattered light intensity at one angle (for example at 90°) from which the particle size is calculated by the software.
The Photon Correlation Spectroscope used for the experiments was a Malvern Zetasizer 4.

4.1.4 Minimum Film Formation Temperature (MFT)

The MFT is described as the minimum temperature at which a water-borne synthetic latex or emulsion will coalesce when cast as a thin film. The MFT is closely related to T_g but not synonymous with it, in most cases it is a few degrees blow T_g. Above the MFT the latex will form a clear, transparent film. Below the MFT a white powdery cracked film is formed.
The minimum film formation temperature is measured with a MFT bar. This bar consists of a metal plate, which is electronically heated/cooled with a temperature gradient in a known temperature range (e.g. from –5°C to 13°C), so that the one end is cooler than the other end. Air or nitrogen is caused to flow constantly over the surface, from the cool end to the warm end to dry the thin film. The MFT is the temperature where the film changes from a white cracked film into a transparent film.
For low T_g polymers with a T_g close to 0°C it is hardly possible to determine MFT, because the latex is freezing instead of filmforming in the temperature range of interest. In this case the MFT is indicated with “NR” for no reading.

4.2 Polymer Synthesis and Properties

4.2.1 Emulsions

The investigated polymer dispersions were provided by Plascon research or synthesized with under guidanceof the Plascon research group. All latices were

prepared by emulsion polymerization. The latices consist of random copolymers containing two or more monomers.
The theoretical value of the glass transition temperature of the copolymer was calculated by using the Fox equation [9]:

$$\frac{1}{T_{g(copolymer)}} = \frac{w_1}{T_{g1}} + \ldots + \frac{w_i}{T_{gi}} \qquad (4.1)$$

In this equation T_{gi} is the glass transition of the constituent monomer's homopolymer and w_i is the weight fraction of that particular monomer in the copolymer composition.
The T_gs of the monomers used were about 100°C for styrene (S), -54°C for butyl acrylate (BA), 228°C for methacrylic acid (MAA), about 105°C for methyl methacrylate (MMA) and 30°C for vinyl acid (VA).
The solid content of all emulsions was about 50%.

4.2.1.1 Unstructured Polymers

The investigated unstructured latices (UL) were:

Polymer Name	Monomers	Particle Diameter	T_g	MFT
UL1	4.82% S, 19.25% MMA, 18.97% BA, 1.28% MAA	80nm	23°C	19°C
UL2	56.85% S, 40.27% BA, 2.89% MAA	102nm	19°C	20°C
UL3	15% BA, 85% VA	Not meas.	12°C	10°C

Table 6: Unstructured latices

4.2.1.2 Core-Shell Polymers

The synthesis of the core-shell (CS) latices was conducted under flooded conditions using reflux to exclude oxygen during the polymerization process. Typically the reactor, containing water (distilled and de-ionized), surfactant and ammonium carbonate as buffer was heated to 85°C in a water bath equipped with a thermostat. The monomer, constituting the core phase, was then added over a period of two hours. The shell-phase monomers were added subsequently, also over a period of two hours.
After monomer addition the reactor was kept at 85°C for a further 30 minutes before lowering the temperature. Tert-butyl hydroperoxide was added at a temperature of 70°C to react with any remaining monomer in the system. The reactor was then kept at 70°C for 10 minutes before cooling to room temperature.

The theoretical values of the glass transition temperature of core and shell were calculated by using the Fox equation (eq. 4.1).

Polymer	Monomers (core / shell)	Particle Size	T_g (core)	T_g (shell)	2.2.1.1. FT
CS1	65.09% S, 23.07% BA, 3.88% MAA, 4.6% EGDMA 49.07% S, 49.07% BA, 1.64% MAA	85.7 nm	65.5 °C	2.2°C	NR
CS2	68.23% S, 24.18% BA, 4.07% MAA 49.07% S, 49.07% BA, 1.64% MAA	88.1 nm	49.95 °C	2.8 °C	NR
CS3	40.38% S, 13.91% BA, 36.93% MMA, 2.99% MAA, 5.8% EGDMA 49.66% BA, 47.41% MMA, 2.94% MAA	80 nm	89.93 °C	6.16 °C	NR

Table 7: Core-shell latices

In order to obtain different particle sizes, CS3 particles with a crosslinked core and a core-shell ratio of 2/5 were produced using different surfactants (anionic surfactants from Stepan Company Northfield, Illinois, USA). The theoretical T_g of the core was for all latices 89.93°C, and the theoretical T_g of the shell was 6.16°C.
The following surfactants were used to obtain different particles sizes, based on their different CMC values:

- Polystep B25: a sodium salt of a sulfated alkyl alcohol.
- Polystep B27: a sodium salt of nonylphenoxypolyethyleneoxyethanol sulfate
- Polystep B29: a sodium salt of sulfated alkyl alcohol.

By employing these surfactants the following particle diameters were obtained:

Surfactant	Av. Particle Size
B25	68.5 nm
B27	79 nm
25%B27 + 75% B29	104.7 nm
15% B27 + 85% B29	110 nm
B29	322 nm

Table 8: Different Surfactants and achieved particle size.

It was not possible to determine any MFTs for the latices with different particle size, since they are variations of the core-shell latex CS3 with a low T_g shell and a MFT too close to 0°C.

In order to compare different core-shell ratios, CS3 polymers with a crosslinked core and a particle size of about 110 nm were produced with the following core/shell ratios (by mass):

Core/shell ratio	Amount in %	Core radius
2/3	40% core, 60% shell	$r_{core} = 0.74\ r_{shell}$
2/4	33% core, 66% shell	$r_{core} = 0.69\ r_{shell}$
2/5	28.6% core, 71.4% shell	$r_{core} = 0.66\ r_{shell}$
2/6	25% core, 75% shell	$r_{core} = 0.63\ r_{shell}$
2/7	22% core, 78% shell	$r_{core} = 0.60\ r_{shell}$
2/8	20% core, 80% shell	$r_{core} = 0.59\ r_{shell}$

Table 9: Core-shell polymers with different core/shell ratio.

Again, it was not possible to determine MFTs of the latices with different core/shell ratios for the same reason of the T_g being to close to 0°C.

4.2.1.3 Gradient Polymer

The preparation of the reactor was the same as for the core-shell synthesis. Synthesis of the gradient latex was achieved by separating the monomers that constitute the "hard" part of the latex, such as MMA and styrene, from the monomers that constitute the "soft" part of the latex, such as BA. The reaction was started by adding the solution of "hard" monomers over a period of 15 minutes into the reactor to "seed" the emulsion polymerization reaction before starting the second addition of the mixture of "soft" monomer, not to the reactor, but to the vessel containing the "hard" monomers.

In this way the composition of the monomers in the vessel metered into the reactor was gradually changed. Simultaneously the glass transition temperature of the resulting polymer was gradually changed. The result of this synthesis is a latex with a structure that changes gradually from a hard polymer phase to a soft phase.
This core-shell polymer has a crosslinked core and a shell consisting of a copolymer, which contents are gradually changing from the inner side to the outside. Around the core the copolymer consists of 100% PS, gradually decreasing towards the outside. The experimental setup to achieve a gradient latex is displayed in Figure 4.5 and the properties of the resulting latex are described in table 5.

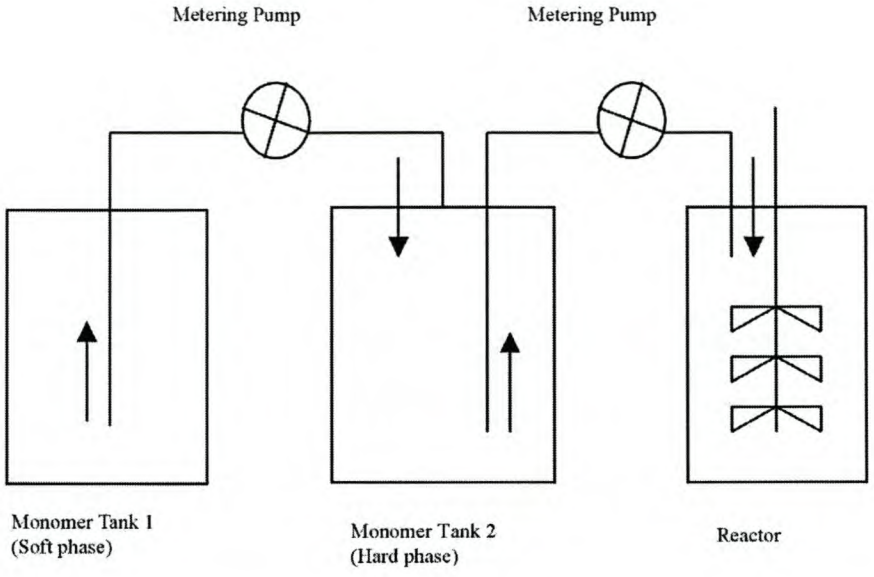

Figure 4.5: The experimental setup used to prepare a gradient polymer latex.

Polymer	Monomers core / shell	Particle Size	T_g (core)	T_g (shell)	MFT
GRAD1	68.23% S, 24.18% BA, 4.07% MAA 49.07% S, 49.07% BA, 1.64% MAA	85.7 nm	49.95 °C	100°C to -45°C	6.7°C

Table 10: Gradient polymer.

4.2.2 Polyolefins

Polyolefins used in this study were oligomers rather than polymers, consisting of only a few monomers. Their structure is based on ethylene units. If the polymer has side chains, two carbon atoms are incorporated into the backbone and the side chain is shortened by two carbon atoms compared to the original monomer. For example, poly-tetradecene would have side chains with 12 carbon atoms attached to a polyethylene backbone.

Higher α-olefins, like pentene, hexene etc. up to octadecene, were polymerized at room temperature using $(CH_3)_2Si(2\text{-methylbenz[e]indenyl})_2ZrCl_2$ and the cocatalyst methylaluminiumoxide (MAO) [10]. The resulting polymers had a molar mass of about 160,000 g/mol.

Due to the side chains, the α-olefins can form two crystalline structures, depending if the main- or the side chains are crystallizing. The two melting points are generally attributed to the melting of crystals formed by the long side chains and the helical main chain [11].

4.2.3 Thin Films

Thin polystyrene (PS) films of different molecular weight and well-defined film thickness were prepared by J. Howse, University of Sheffield.
The PS was spin-coated on (100) silicon wafers, that were previously cleaned in an oxygen plasma. The PS solution was made in HPLC grade toluene and filtered prior to the spin coating. The duration of spin coating in all cases was 30 seconds. After spin coating, the samples were annealed in vacuum at 115°C for 24 hours and subsequently cooled at a rate of 1°C per minute. The film thickness was measured by ellipsometry.
The prepared films had a molecular weight of 868800 g/mol, 142500 g/mol and 22000 g/mol. The film thickness ranged from 130 Å to 1100 Å.

4.3 Sample Preparation

Generally polymer films were prepared by spreading a thin layer of the polymer emulsion onto a silicon surface, and then flattening it with a microscope slide. The thickness of these films could not be determined accurately but was estimated to be between 20µm and 50µm. The polymer films were dried for at least 3 hours under ambient conditions.

For DSC and DMA analyses a drop of polymer was applied to a substrate and the samples were dried under ambient conditions for 12 hours.

In order to cast a film of the polyolefins, a piece of the polymer was put on a silicon substrate, which was heated above the higher of the two melting points. The sample melted and formed a smooth film on the silicon substrate. Subsequently the film was cooled to room temperature and kept in a desiccator for at least 5 days to allow the polymer to re-crystallize.

4.4 Experimental Methods Used for Polymer Studies

4.4.1 Ultrasonic Shear Wave Reflection

Ultrasonic (US) shear wave reflection was used to determine the storage (G') and loss modulus (G'') of different dispersions. The moduli are measured as a function of time, as displayed in Figure 4.6.

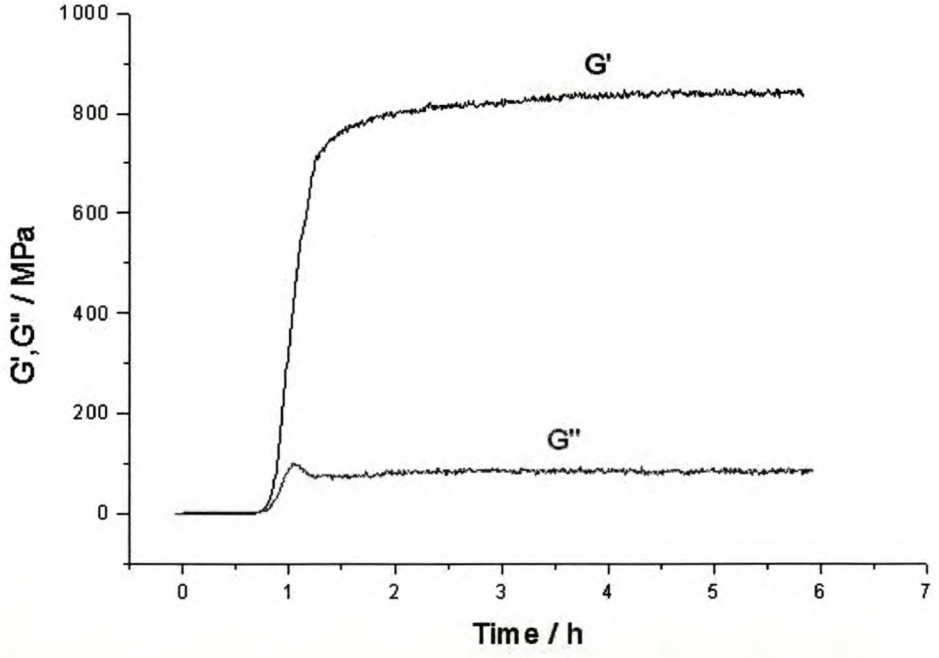

Figure 4.6: Typical curves of storage (G') and loss (G'') modulus acquired with ultrasonic shear wave reflection.

This method yields information about the kinetics of the film formation process during the drying of the emulsion. The slope of the curve represents the water evaporation and shows how the emulsion dries and forms a film. The steep increase at the beginning represents the first stage of drying, i.e. the rapid water loss by evaporation from the surface. The part of the curve before the plateau value of the modulus is reached, represents the second stage of drying, or film formation where the interstitial water diffuses through capillaries and the dry membrane formed at the polymer/air interface. The final value of the plateau gives indication about the hardness of the dried film.

The experiments were performed using the instruments of the physics group of the Deutsches Kunststoff Institut (DKI) in Darmstadt, Germany. A comprehensive explanation of the method can be found in [12-16].

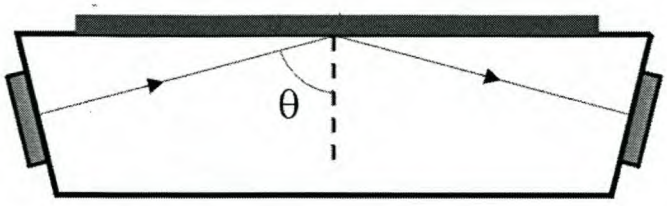

Figure 4.7: Schematic drawing of the shear wave reflection method. The polymer film is cast on the quartz glass and the US wave is reflected at the interface.

Ultrasonic shear wave reflection measures the mechanical impedance of viscoelastic materials, which is related to the complex shear modulus G^*. If a shear wave (with frequencies around 5MHz) is reflected at the solid/liquid interface, as displayed in Figure 4.7, at normal incidence, with the oscillation direction parallel to the interface, the complex reflection coefficient r* is expressed by:

$$r^* = r \cdot e^{-i(\pi-\phi)} = \frac{Z_l^* - Z_s^*}{Z_l^* + Z_s^*} \tag{4.2}$$

where Z_s* and Z_l* are the complex dynamic shear impedance of the solid and the viscoelastic (liquid) sample. In the case of the solid, here fused quartz glass, Z_s only has a real component, whereas the shear impedance of the polymer is complex: $Z_l^* = R + iX$. The shear impedance is defined as the ratio of the shear stress to the rate of change of displacement transverse to the direction of wave propagation.
The complex dynamic shear impedance of the sample Z* is related to the complex dynamic shear modulus G* = G'+iG'' as follows:

$$Z^2 = (R+iX)^2 = \rho\,(G'+iG'') \tag{4.3}$$

where ρ is the density of the polymer.
The storage and the loss component of G* are given by:

$$G' = \frac{R^2 - X^2}{\rho} \qquad G'' = \frac{2RX}{\rho} \tag{4.4}$$

The storage and loss modulus are calculated from the measured reflection and absorption coefficient of the polymer and the phase shift between the transmitted and the received ultrasonic wave.

Another measurement cell, the "longitudinal" cell, is displayed in Figure 4.8. It uses a vertical incidence of the US waves.

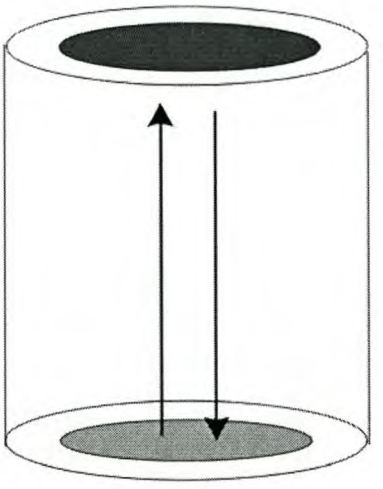

Figure 4.8: US measurement cell with vertical wave incidence.

The advantage of this method lies in the fact that neither for longitudinal, nor for transversal waves, a mode transition occurs. Additional and analogous to the shear modulus, the acoustic impedance for longitudinal waves yields the longitudinal modulus of the polymer.

In the experimental setup at the DKI 10 longitudinal cells can be used simultaneously in an environmental chamber that has humidity and temperature control. This makes it possible to compare the measured shear moduli for different latices.

Films of about 200 μm thickness were cast on each cell. The film thickness was controlled by using a mask of 200 μm height and using a sharp metal blade to flatten the dispersion.

4.4.2 The Atomic Force Microscope

The AFM used for all experiments was a Topometrix Explorer. It was always operated in the low-amplitude non-contact mode, which means the driving amplitude of the oscillating cantilever was below 1V. Typically, the driving amplitude in the performed measurements was between 0.2 and 0.5 V.
The used cantilevers were non-contact silicon cantilevers from Nanosensors GmbH/Germany with a nominal resonance frequency of about 170 kHz and a force constant of about 50 N/m. The dimensions of these cantilevers are about 225 μm x 28 μm x 7 μm. The tip has a pyramidal shape with a height of 10 to 15 μm and typical tip radii smaller than 10nm.

Most measurements were performed under ambient conditions. The samples were mounted on a heating / cooling stage consisting of two Peltier elements. The temperature range of both elements used seriell ranged from about –20°C to 120°C.

On top of the Peltier elements was a copper block with a PT 100 resistive temperature sensor to measure the temperature of the system. This arrangement led to slight deviations between the measured temperature and the real surface

temperature of the polymer. Thus, the acquired temperature values are not correct in their absolute values but the relative temperature change is correct.
When the experiment required controlled environmental conditions, the sample and the AFM were put in an environmental chamber, as sketched in Figure 4.9. In this chamber the pressure and the temperature could be controlled.

The heating / cooling stage in the vacuum chamber was a Joule-Thompson element (MMR Technologies Inc.), which allows temperature variations between –70°C and 200°C. The temperature of the system was measured by a silicon diode mounted below the polymer sample, which, again, led to slight deviations in the absolute values of the measured transitions temperatures.
A rotation pump and a turbo pump were connected to the chamber and allowed the pressure to be decreased as far as 10^{-5} mbar.
The sample was mounted onto a x-/y-translator, which could be controlled electronically from the outside by a motor. Different positions on the sample could therefore be investigated without disturbing the vacuum.

To isolate the system against vibrations the AFM and the environmental chamber were placed on an air-table.

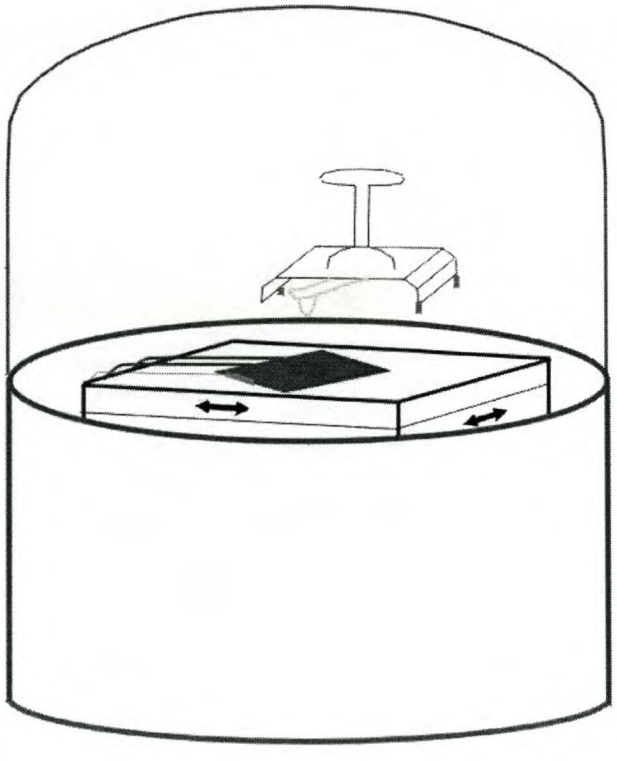

Figure 4.9: Experimental setup of the AFM in the environmental chamber

4.5 Data Acquisition and Processing

4.5.1 Film Formation Studies

Polymer films were typically cast below their glass transition temperature to slow down coalescence of the particles. A sequence of AFM images was then acquired to monitor the ordering of the polymer particles and the subsequent deformation. After the film was entirely dry, the temperature was increased above the T_g of the polymer to show the interdiffusion and film formation of the particles.
For polymers with a T_g close to room temperature the coalescence and interdiffusion was visible in a sequence of AFM images as a function of time, without the need to heat the sample further.

AFM images of the polymer film were acquired at constant time intervals after casting the film. A typical sequence of AFM images is displayed in Figure 4.10.

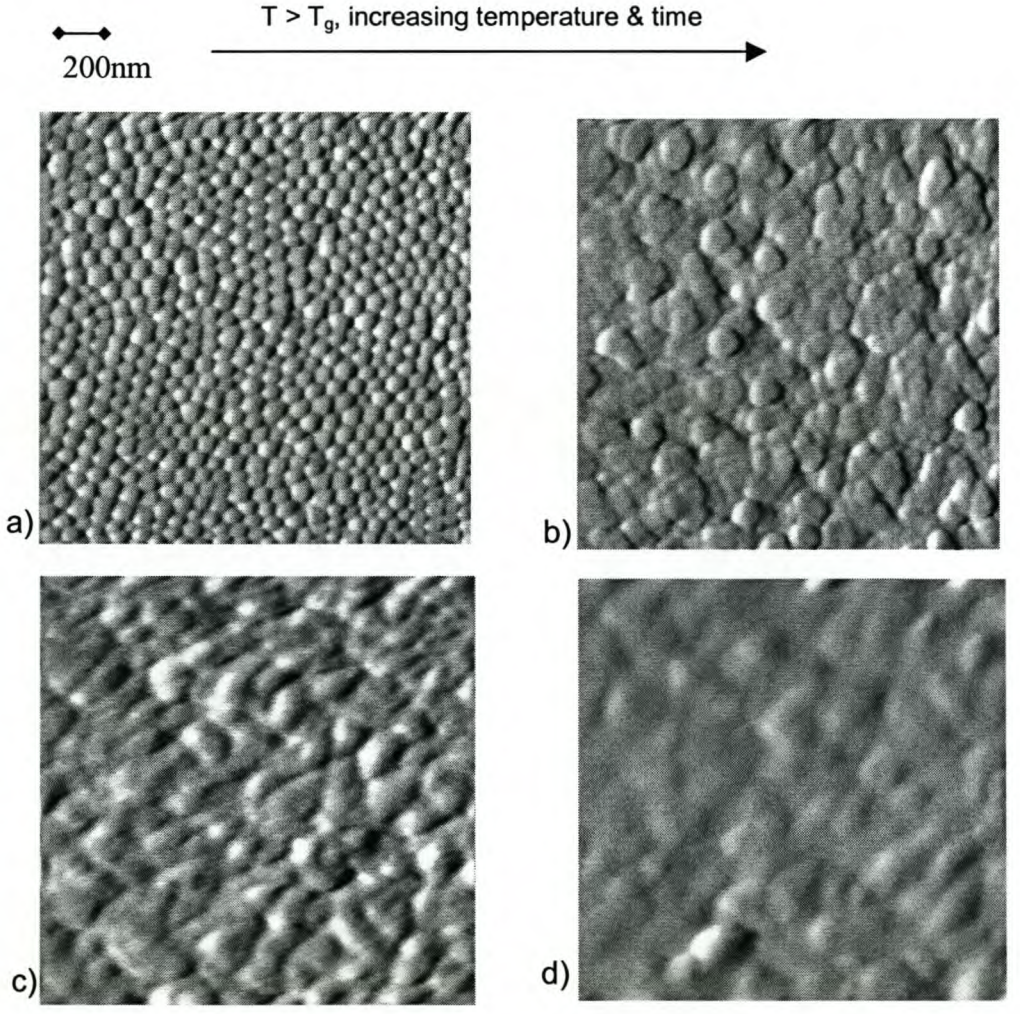

Figure 4.10: Sequence of AFM images showing PS particles losing shape and growing with increasing time or temperature until they interdiffuse and form a smooth film.

The film was dried below the T_g of the latex and the particles formed an ordered array. Subsequently the temperature was increased above the T_g. The particles lost their spherical shape, interdiffused and finally form a smooth film.

The AFM images acquired in this way were processed and analyzed in the Topometrix imaging program. Each AFM image yielded an average particle diameter with a standard deviation calculated from all recognizable particles in the image. The average particle diameter was determined by drawing line scans at different positions through the image and measuring the valley-to-valley distances, as displayed in Figure 4.11.

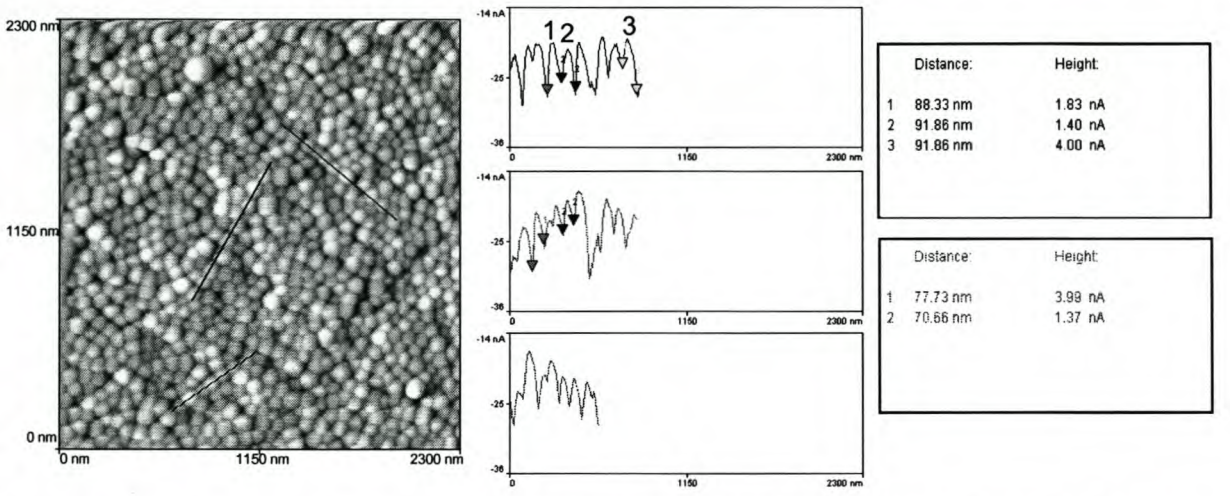

Figure 4.11: Images of polymeric particles. The average particle diameter is determined with the Topometrix analysis software by measuring valley-to-valley distances along the lines through the image.

In the case of core-shell particles, the core diameter was measured, as soon as the cores became visible at the surface. In the particle size / time plot this resulted in a particle diameter smaller than the original particle size.

Another analysis method used, was to process the entire image as a 400x400 matrix with gray values between 0 and 255 and to calculate a correlation function [17]. A program, written in C++, calculates the average gray value of all points around a point x,y with the same distance to this point. This is done for all image points and results in the two-dimensional correlation function g(x,y). A circular averaging yields the one-dimensional radial correlation function g(r). The program is attached in the appendix.

The first maximum represents the average nearest neighbor distance, and the first zero crossing represents the average peak-to-valley distance, or in other words, the average particle radius. The correlation function of a conventional, unstructured polymer is displayed in Figure 4.12.
As the particles grow and change their shape the long-range order in the correlation function disappears and consequently the higher maxima disappear.

If the average particle diameter was to be calculated using a correlation function, the sample needed to be very well prepared. The film should be flat on a molecular scale and the polymer spheres ordered hexagonally.

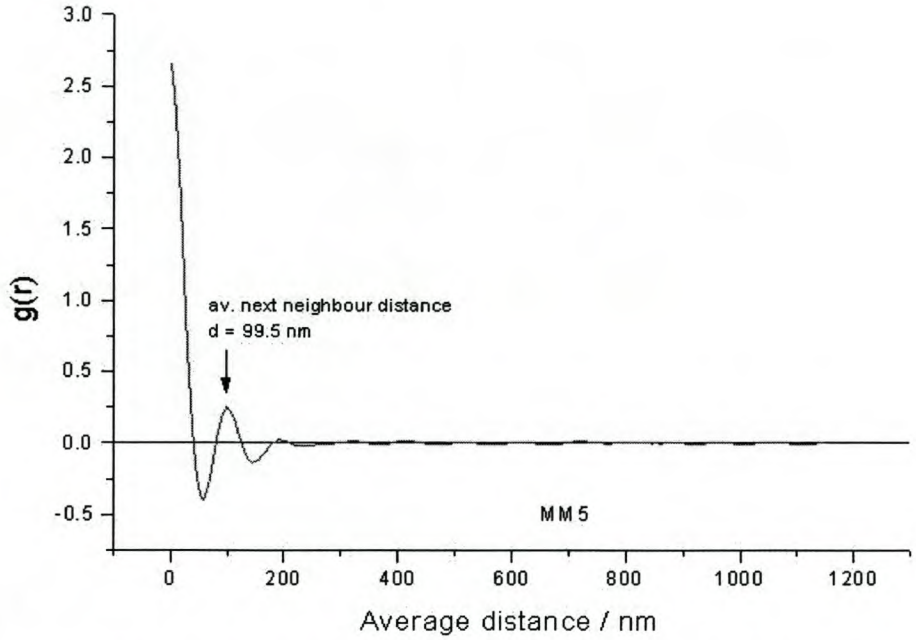

Figure 4.12: The radial correlation function of a conventional polymer to determine the average nearest neighbor distance.

If the film was rough and the particles not ordered, the averaging in the correlation function led to incorrect average particle diameter values. The particle diameter could then only be determined "manually" using the Topometrix imaging software.
The average particle diameter, acquired either by the correlation function or averaging all diameters measured in the imaging program, was then plotted as a function of time or temperature, as shown in Figure 4.13.

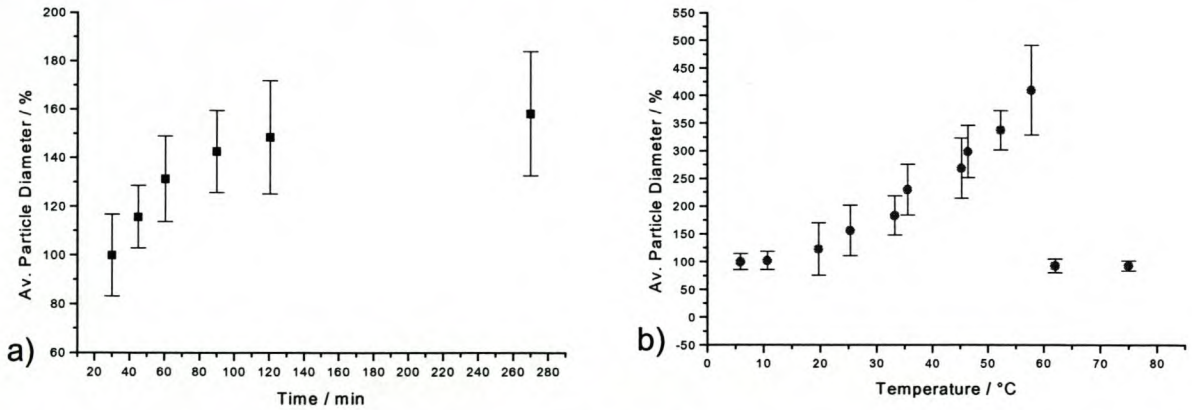

Figure 4.13: The increase of the average particle diameter as a function of (a) time, or (b) temperature.

As time or temperature increases, the average particle diameter increases since the polymer spheres lose shape and start to coalesce. The resulting curves provide thus information about the film formation kinetics of the latices and display the deformation behavior of the particles.
Since the coalescence of the particles and their agglomeration or diffusion does not necessarily happen at a constant rate, the particles size distribution becomes more polydisperse with increasing time or temperature. This can be seen in the increasing error bars of the average particle size.
In order to be able to compare the acquired particle diameter values for the different latices and the behavior of the film formation kinetics, for example, the slope of the particle diameter versus time, the average diameter of the first AFM image of each sequence was set to 100%. The particle diameters of the following images were calculated according to this value. Thus the changes in the particle size with time or temperature could be visualized and compared.
Image sequences as a function of time were acquired under ambient conditions at room temperature (ca. 20°C).
When the average particle diameter was acquired as a function of temperature, the heating rate was for all emulsions about 1°C/min. Even with time passing during the temperature change the curves could thus be compared.

4.5.2 Resonance Frequency Measurements

In order to avoid contact between the AFM tip and the polymer surface, or wetting of the tip by the polymer, the distance between the surface and tip was kept fairly large. Automatic tip approach was carried out and the cantilever was then retracted with the z-motor, so that the feedback software did not control the distance between the tip and the sample surface. The cantilever remained at a fixed position of several micrometers above the specific surface-spot chosen for analysis. It was not possible to determine the exact distance between the tip and the sample surface with the current setup. Estimations using the video camera of the Topometrix system (magnification x1000) yield a distance of about 20 μm between the tip and the sample.

The oscillation frequency of the cantilever was then swept from 0 to 400kHz to determine the resonance frequency of the cantilever. The resonance frequency was determined using the internal oscilloscope in the Topometrix software, which displays the magnitude of the oscillation as a function of the frequency. The resonance frequency is the value at which the magnitude has a maximum. The low resonance frequency cantilevers used had a typical resonance frequency of ±170 kHz.
The resonance frequency was subsequently measured while increasing the temperature in steps of one or two degree Celsius. The frequency range of the frequency sweep was decreased to about 10 kHz around the resonance frequency. This saved measurement time and simplified the determination of the peak maximum.

The temperature of the system was increased at a constant rate of one or two degrees per minute, starting from a value below the transition point of the polymer to be investigated to a value above it; for example from 5°C to 30°C for the copolymer with a T_g of 19°C.
The temperature was adjusted manually by increasing the current through the Peltier elements slowly. The temperature was measured by connecting the PT100 temperature sensor to the K20 control unit of the Joule-Thompson cooling stage. This control unit was connected to a PC and the temperature displayed on the screen. Using this program it was possible to achieve, even by adjusting the current manually, a constant heating rate of about 1.5 °C per minute.
The accuracy of the PT 100 temperature sensor is in the order of 1°C.

4.6 Bibliography

[1] Brown,G., *Journal of Polymer Science*, 1956, **22**, 423
[2] Kendall,K., Padget,J., *International Journal of Adhesion and Adhesives*, 1982, **July**, 149
[3] Eckersley,S., Rudin,A., *Journal of Coatings Technology*, 1990, **62**, 89
[4] Jensen,D., Morgan,L., *Journal of Applied Polymer Science*, 1991, **42**, 2845
[5] Kan,C., *Proceedings TAPPI Adv. Coating Foundation Symposium*, 1993, **101**,
[6] Dargent,E., Cabot,C., Saiter,J., Bayard,J., Grenet,J., *Journal of Thermal Analysis*, 1996, **47**, 887
[7] Perkin Elmer, 2001, DSC manual
[8] Twombly,B., *Instrumentation Science & Technology*, 1994, **22**, 259
[9] Mark, Bikales, Overberger, Menges, *Encyclopedia of polymer science and engineering 2nd edition*, 1985, 3
[10] Bruell,R., Pasch,H., Raubenheimer,H., Sanderson,R., Wahner,U., *Journal of Polymer Science, A*, 2000, **38**, 2333
[11] Krentsel,B., Kissin,Y., Kleiner,V., Stotkaya,L., 1997, Hanser Verlag, Muenchen
[12] Alig,I., *Handbuch der Kunststoffpruefung*, 1992, Kapitel 10.2
[13] Alig,I., Lellinger,D., Sulimma,J., Tadjbakhsch,S., *Farbe&Lack*, 1996, **12**, 56
[14] Alig,I., Lellinger,D., Sulimma,J., Tadjbakhsch,S., *Review Scientific Instrumentation*, 1997, **68**, 1536
[15] Alig,I., Tadjbakhsch,S., Zosel,A., *Journal of Polymer Science, B: Polymer Physics*, 1998, **36**, 1703
[16] Alig,I., Tadjbakhsch,S., *Journal of Polymer Science, B: Polymer Physics*, 1998, **36**
[17] Eurich,F., 2000, Lehrstuhl Dieterich, Universitaet Konstanz (see appendix)

CHAPTER 5: Imaging of Polymer Surfaces

5.1 Film Formation Studies

The deformation and film formation behavior of latex particles was investigated by AFM. To achieve a comprehensive picture of the film formation behavior, latices with different structures, different core-shell ratios and different particle sizes were studied. The influence of different additives, such as coalescent solvents or rheology modifiers, on the emulsion was investigated as well.

5.1.1 Drying

The drying process of an emulsion was monitored by applying the latex onto the substrate at a temperature below its T_g and then freeze-drying it to conserve the particle "order", or rather disorder, in the water.

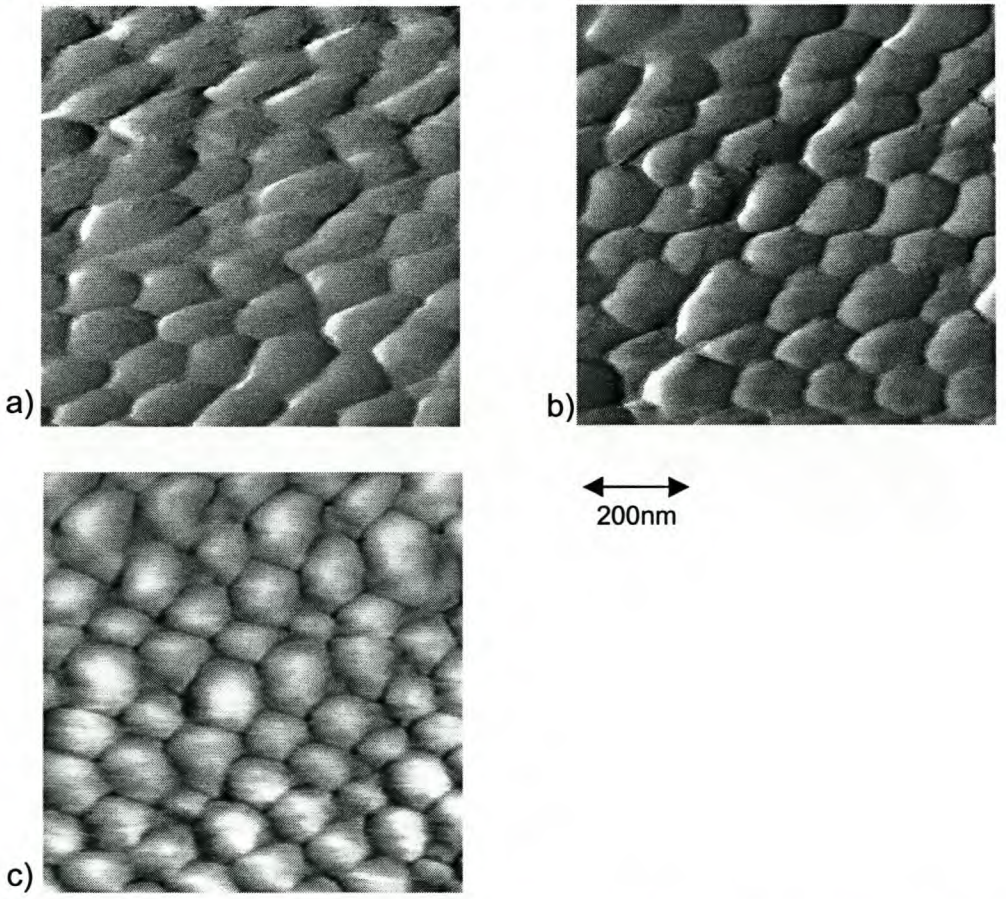

Figure 5.1: AFM images of a PS emulsion. Ordering of the spherical particles during the drying process of PS as time passes can clearly be seen.

When the pressure in the environmental chamber was lowered from ambient conditions to about 2 mbar, sublimation of the ice began. This process is comparable

to the evaporation of the excess water from the emulsion. The particles became more distinct at the surface, moved closer together and finally formed an hexagonally ordered array [1],[2], as described in chapter 2.2. The spherical particles were deformed into hexagons.
The process of drying and the particle ordering is displayed in Figure 5.1. In dispersion the particles are not ordered and covered by water / ice (a). As the water evaporates (the ice sublimes) the particles are drawn together due to capillary forces (b) and form an ordered array. Eventually the spheres are packed in a closest-packed order and deformed into hexagons (c).

5.1.2 Film Formation

A typical sequence of AFM images acquired as a function of time is presented in chapter 4.5 or in Figure 5.2. From a sequence like this, the average particle diameter could be determined for each image. The average particle diameter as a function of time (or temperature) gives information about the film formation kinetics of the latex.

The average particle diameter was mostly determined using the Topometrix imaging software and measuring the valley-to-valley distance in line scans through the image, as described in chapter 4. If the prepared film was smooth on a molecular scale and the particles formed an ordered array, the average particle diameter was also determined by calculating a radial correlation function from the matrix of gray values representing the topography image. The results obtained by this method agreed well with the particle diameters determined manually.
Figure 5.2 shows a series of AFM images of the unstructured latex UL2 and the correlation functions calculated from the images. It is clearly visible how the particles grow and finally interdiffuse.
The first maximum of the correlation function represents the average next neighbor distance. This value increases with increasing temperature. The long-range order disappears entirely with increasing temperature, as can be seen from the vanishing peaks in the correlation function.
The first maximum shifts from 98nm to 106nm and disappears at about 50°C.

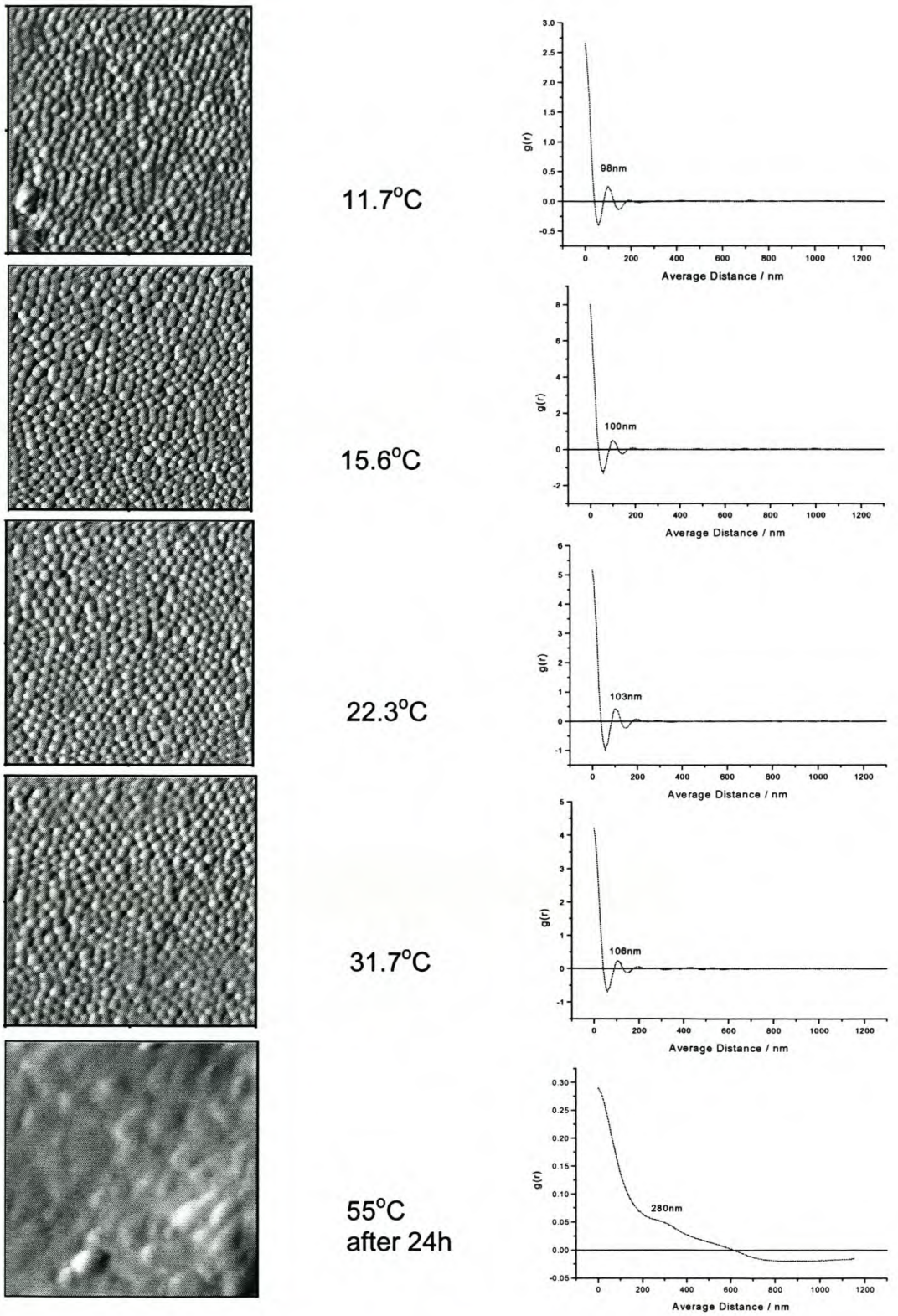

Figure 5.2: Images of the unstructured latex UL2 with increasing temperature (from top to bottom) and the corresponding radial correlation functions.

Besides providing information about the film formation behavior, AFM images obtained as a function of temperature could prove that the proposed core-shell particles really did have a core shell-structure, as displayed in Figure 5.3.

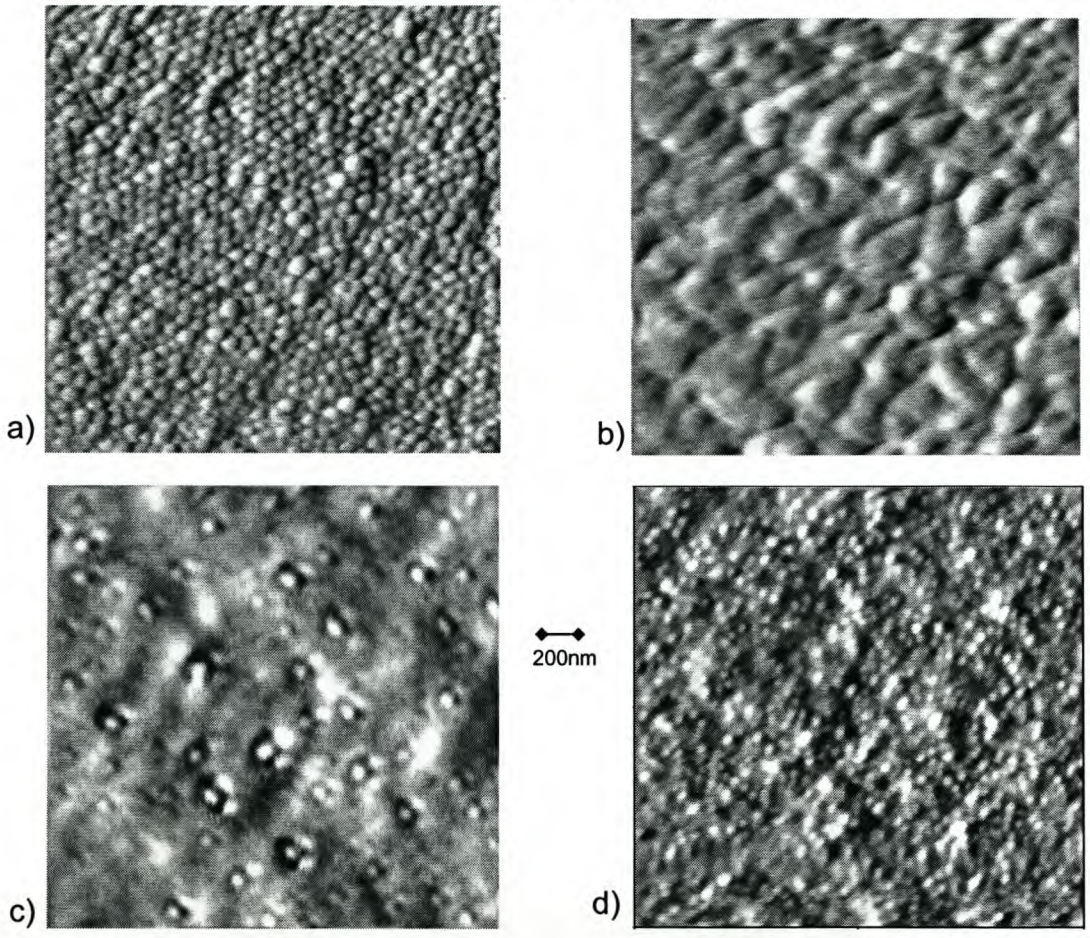

Figure 5.3: AFM images of the core-shell latex CS1 with crosslinked core at increasing temperatures. a) 2°C b) 25°C c) 40°C d) 80°C

The investigated core-shell latices were assumed to consist of hard cores, with a T_g of about 70°C, surrounded by a soft shell, with a T_g of about 2°C. The polymer film was cast below the shell T_g, at around 0°C and the temperature then slowly increased at a heating rate of 1.5°C/min. AFM images were acquired at different temperatures during the heating. Figure 5.3 b) shows how the shell polymers start to deform, flow and interdiffuse above their T_g, until they finally form a matrix around the harder core polymers (c), which retain their spherical shape and appear at the surface. This is to be expected, since the cores are more hydrophilic than the shell polymer, see chapter 4.2. If the cores are crosslinked, any further temperature increase has no influence on their shape, they remain in a spherical shape, as displayed in Figure 5.3 d).

If the cores are not crosslinked, they begin to deform and interdiffuse above their T_g like the shell polymer, and finally form an entirely smooth film. Figure 5.4 shows how the shell polymer of the core-shell latex CL2 deform (a,b). At temperatures well above the shell T_g but still below the core T_g, the cores become visible at the surface

(c). With further increasing temperature the core polymers start to interdiffuse as well and finally a smooth film is formed.

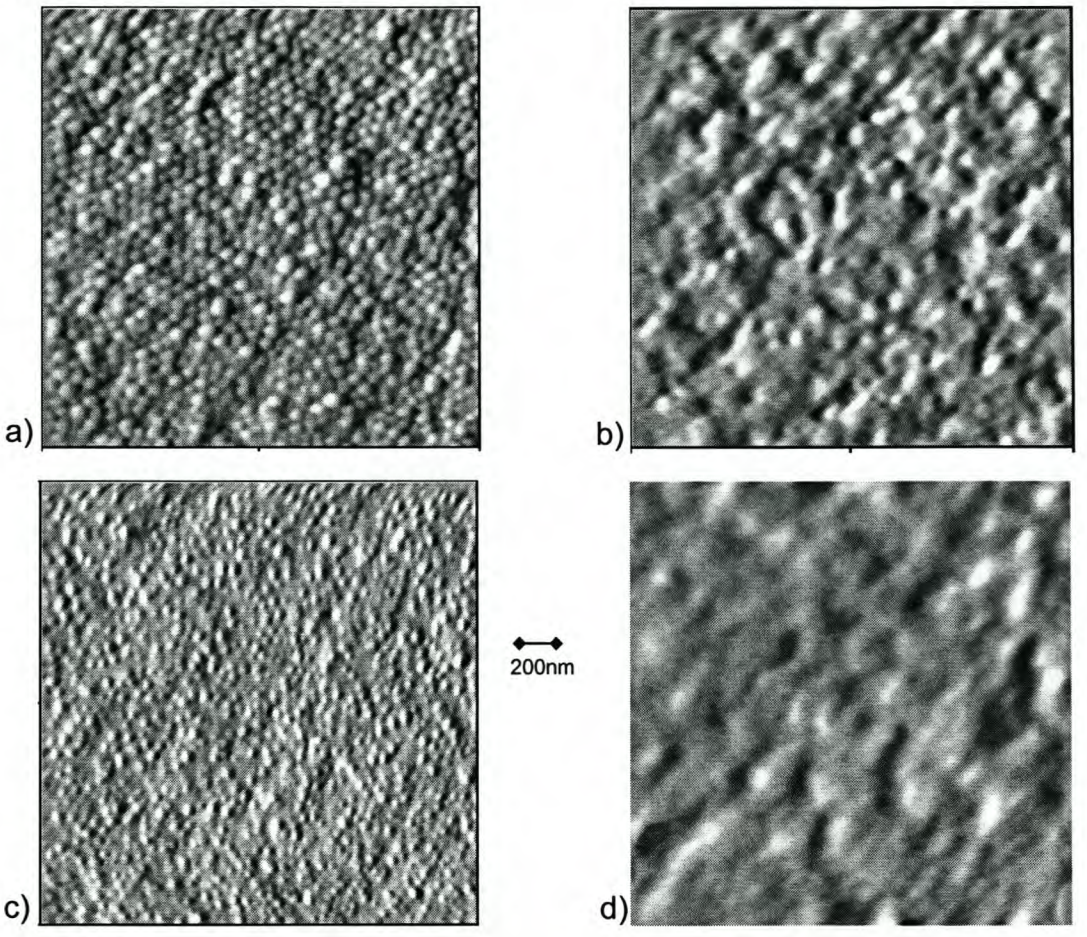

Figure 5.4: AFM images of the core-shell latex CS2 at increasing temperatures. a) 2°C b) 30°C c) 42°C d) 80°C

The acquired values of the average particle diameter as a function of time can generally be fitted with a hyperbolic curve of the form $y = Ax/(B+x)$, with two fitting coefficients A and B. The coefficient A seems to depend strongly on the particle size, whereas B changes with size and structure of the latex particle.
The curves representing the particle diameter as a function of temperature can generally be fitted with a parabolic curve of the form $y = A' + x^{B'}$, with the coefficients A' and B'. B' usually has values between 0.9 and 1.2, which means the curves are nearly linear functions. The values for A' differ greatly, with no obvious correlation between A' and the particle size or structure. A physical meaning of the fit parameters A,B,A' and B' could not be found.
The experimental results allow the comparison of the film formation behavior of different latices and to distinguish which latex filmforms faster and which particle deform to a greater extent, but the findings remain empirical.

5.1.3 Comparison of Different Polymer Structures

A conventional unstructured polymer, a core-shell polymer, a core-shell polymer with a crosslinked core and a gradient core-shell polymer were investigated and their film formation behavior compared. All polymers contained the same monomers (S, BA, MMA and MAA) and had roughly the same particle diameter of 90 to 100 nm. The solid content for all the emulsions was about 50%. The experimental details of the latices are given in chapter 4.2.
Figure 5.5 displays the increase in the average particle diameter as a function of temperature for different types of polymer structure.

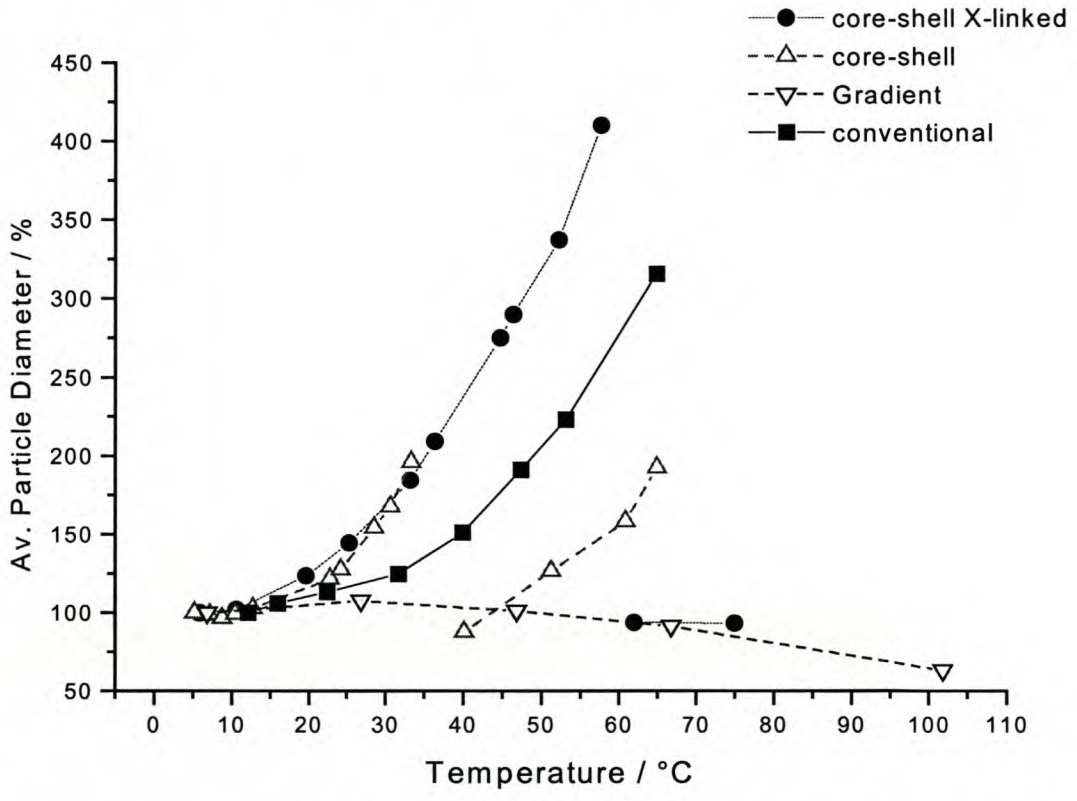

Figure 5.5: Increase in particle diameter of different polymer structures as a function of temperature.

The deformation behavior of the two core-shell polymers (hollow up-triangle,black circle) follows the same trend. Their particle diameters increase faster than that of the conventional and the gradient polymers.
In the case of the uncrosslinked core, the core diameter increases as well, once the cores become visible. The core diameter of the crosslinked cores, however remains constant with increasing temperature.
The conventional, unstructured latex (black square) deforms less than the core-shell polymers. The particle diameter only increases to a value of about 300% of the start value in a temperature range of 60°C, which means that the particles can still be recognized as individual particles and that the surface is not entirely flat.
The diameter of the gradient polymer (hollow down-triangle) decreases slightly because the pure BA at the outer part of the shell starts to flow above 5°C, leaving

only the core surrounded by a shell with a higher styrene content towards the center. This structure prevents further interdiffusion of the particles and thus no further increase in the particle diameter can be observed.

The particle diameter as a function of time at room temperature (about 20°C) shows similar deformation behavior. Figure 5.6 shows an increase in the particle diameter of the different polymer structures as a function of time.

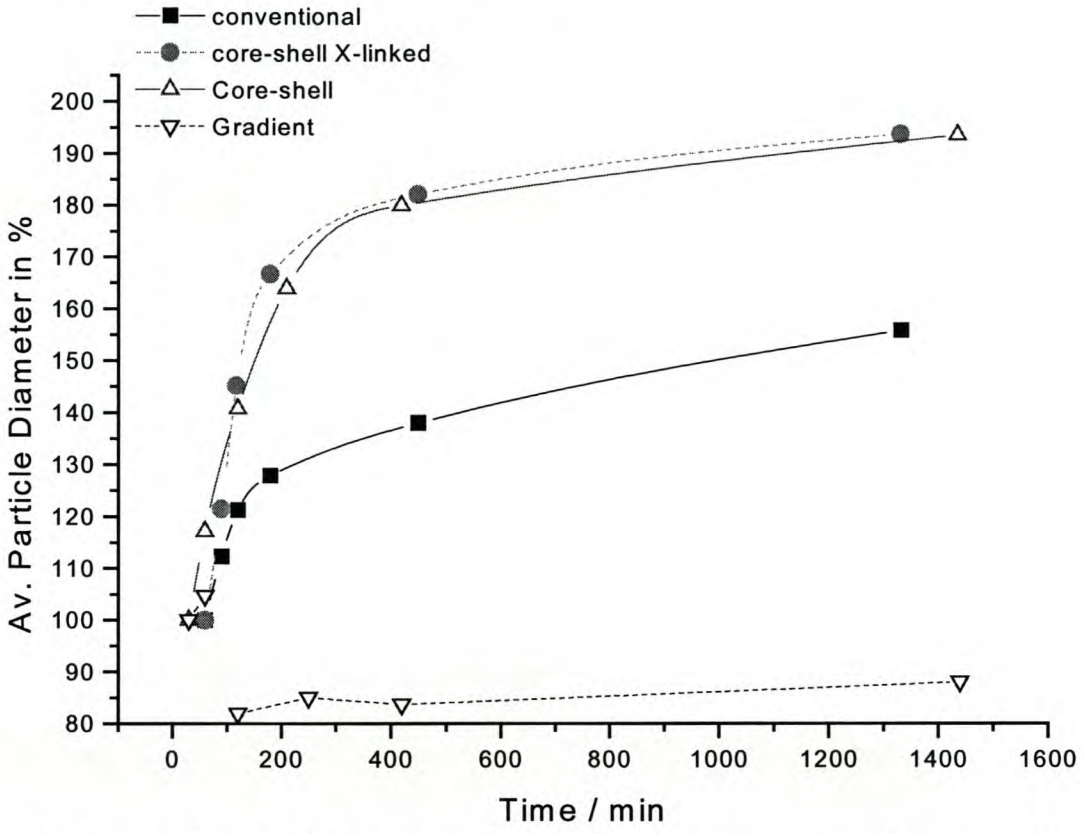

Figure 5.6: Increase in particle diameter of different polymer structures as a function of time.

Again, the two core-shell polymers (hollow up-triangle, black circle) follow the same trend. Their particle diameters increase faster than the particle diameter of the conventional, or the gradient, polymer. This means that the particles coalesce earlier and the film formation starts earlier. The soft shells have a T_g below room temperature and can therefore start flowing and coalescing at room temperature.
The T_g of the conventional polymer (black square) is only slightly below room temperature, which means that the polymers do not flow as easily as the shell polymers of the core-shell polymer, and the film formation process takes place over a longer period of time. Again, the increase in particle diameter is not as great as for the core-shell particles.
The diameter of the gradient polymer (hollow down-triangle) particles remains almost constant after a slight initial decrease. The soft BA in the shell could start flowing around the cores at room temperature and revealed the cores surrounded by the harder PS. The T_g of S is at 100°C substantially higher than room temperature so the

remaining shell of the polymer cannot flow, and the particle diameter stays constant with time.

A core-shell polymer with a hard core and a soft shell that film-forms easily at room temperature is obviously the favored polymer structure if film formation under ambient conditions is desired.

The ultrasonic shear wave measurements in Figure 5.7 confirm the findings of the AFM measurements.

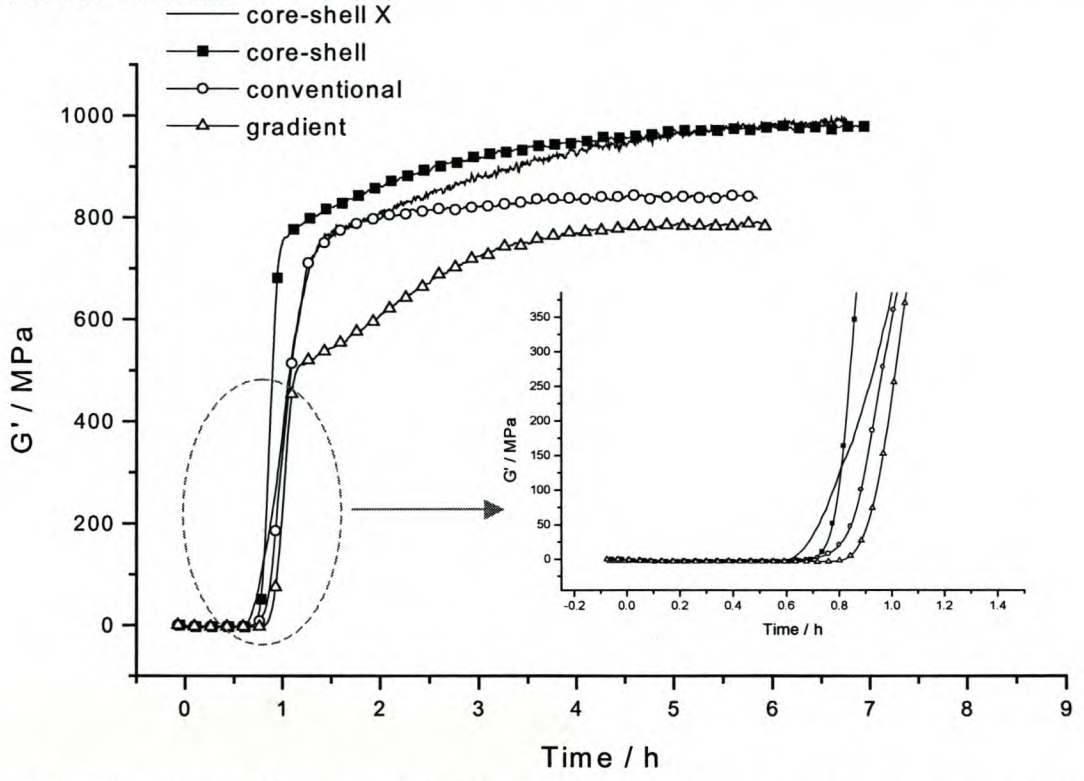

Figure 5.7: The real part of the shear modulus for the different polymer structures. Symbols mark every 20th measurement point to be able to differentiate between the curves.

Both core-shell polymers show an equally fast initial water evaporation, which starts after about 10 minutes. The second stage of film formation - the water diffusion through capillaries and the dry membrane, represented by the skew region before the plateau – is very pronounced for both core-shell polymers. It starts for both core-shell polymers about 1 hour after applying the film. Both core-shell latices reach the same end-value of the shear modulus of about 1000 MPa, which means the dry films have the same hardness and are harder than the films formed by the conventional and the gradient latex.

The conventional polymer dries initially slower than the core-shell polymers but the shear modulus reaches its end-value already after about 90 minutes. The second stage of film formation is hardly recognizable. This corresponds well with the AFM measurements, where the diameter of the conventional polymer increases at a slower rate than the diameter of the core-shell polymers.

The gradient polymer initially behaves in the same way as the conventional polymer. The second stage of film formation starts after about 1 hour and is much more pronounced than for all other latices. The final value of the shear modulus is the lowest of all latices compared, thus the film formed by the gradient latex is the softest of all compared samples.

5.1.4 Comparison of Different Core/Shell Ratios

To observe the influence of the core/shell ratio on the film formation process the core-shell latices CS3 with a crosslinked core and different core/shell ratios were prepared. The compositions of all compared polymers were similar. The diameter of the entire particle was around 110nm, the solid content about 50% and the core/shell ratio was altered from 2/3, 2/4 etc. to 2/8.

Morgan [3] studied the film formation behavior of different core-shell polymers with a soft shell surrounding a hard, but uncrosslinked core, for different core/shell ratios. They found that with increasing thickness of the soft shell the MFT decreases since the film-forming abilities increased.
In was not possible to determine MFTs for the here investigated polymers, since they were core-shell polymers with a low T_g shell. The reading for the MFT values was below 0°C, which means not determinable.

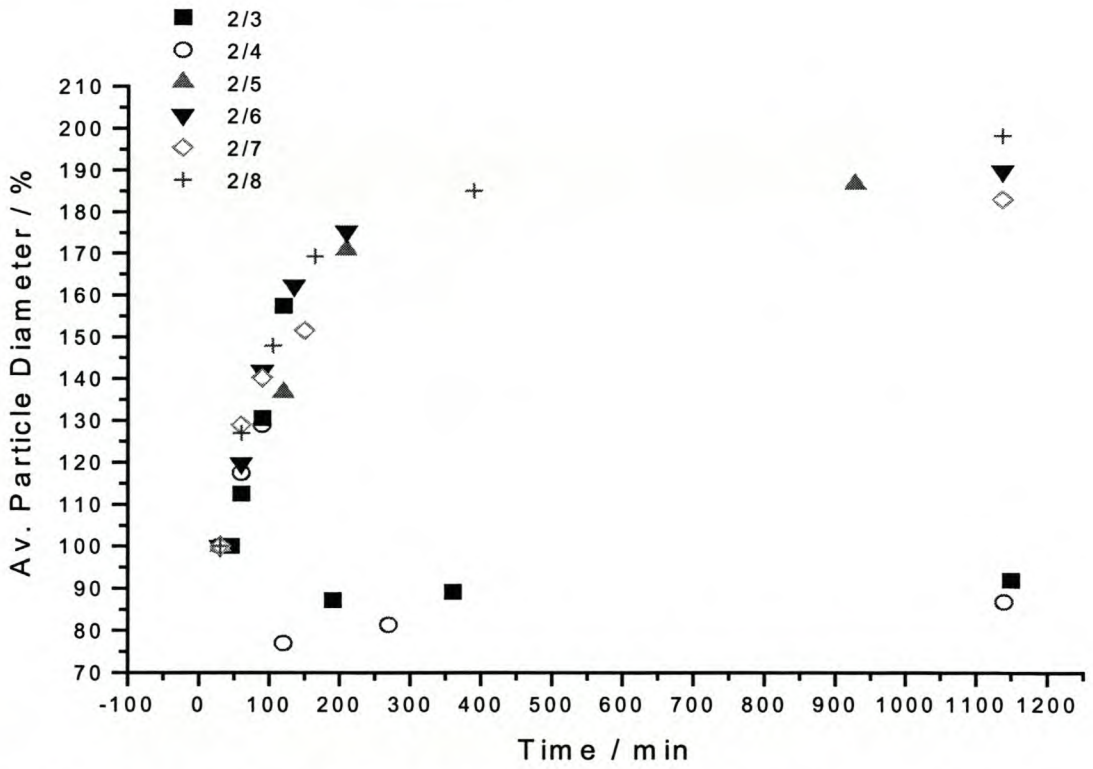

Figure 5.8: Particle diameter of core-shell polymers CS3 with different core-shell ratios, as a function of time.

The AFM measurements could not confirm these findings. All polymer samples behave similarly in the way they are deformed. All curves follow the same trend, as displayed in Figure 5.8, indicating that there is no difference in the film formation behavior.
The soft shell starts to deform and flow at room temperature and causes the increase in particle diameter, which is comparable for all latices. Even with a different amount of shell polymer, the characteristic film formation behavior is the same for all compared latices.

The latices with the core/shell ratio of 2/3 and 2/4 respectively have the largest percentage of cores, covered only with a thin shell. After about two hours the cores are revealed on the surface surrounded by shell polymers that form a film around the cores. The particle size of the cores does not increase with time because of the crosslinking. For the polymers with thicker shells (core/shell ratio 2/5 and smaller) only, the shells only deform with time and start to coalesce but the cores do not become visible at the surface. The deformation behavior follows the same trend for all core/shell ratios.

Figure 5.9 displays the increase in particle diameter as a function of temperature. Again all particles show more or less the same deformation behavior. The only difference is the temperature at which the cores become visible at the surface.

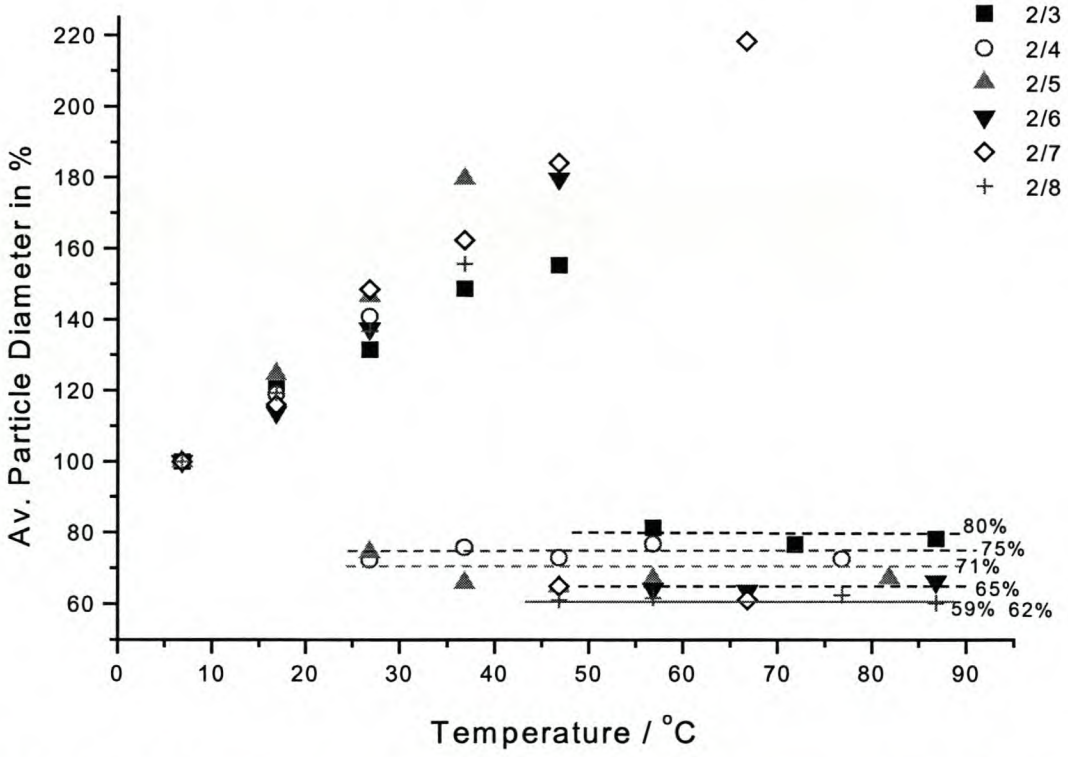

Figure 5.9: Particle diameter of core-shell polymers CS3 with different core/shell ratio, as a function of temperature.

The different core sizes, ranging from about 80% (core/shell ratio 2/3) to about 59% (core/shell ratio 2/8) of the of the original particle diameter, are clearly visible in the

plot. The values agree well with the calculated values for the core diameter ranging from 59% to 75% of the particle diameter of the entire core-shell particle.

If a smooth surface is desired then the core/shell ratio should obviously be rather small. For the polymer composition used here, a core/shell ratio of 2/5 or smaller was found to be sufficient.

Unlike the AFM measurements, the ultrasonic shear wave measurements show a different film formation behavior for different core/shell ratios, as displayed in Figure 5.10. Latices with a core/shell ratio of 2/3, 2/5 and 2/8 were investigated by ultrasonic shear wave reflection. The curves were mathematically corrected for the different solid contents in the emulsion and the density of the polymer.
The results show that the particles with the thicker shell (core/shell ratio of 2/8) start to film-form first, followed by particles with the thinner shells with a core/shell ratio of 2/5 and finally of 2/3. The hardness of the dried film increases with the core/shell ratio. Particles with a core/shell ratio of 2/3 form a harder film than particles with core/shell ratios of 2/5 or 2/8 do.

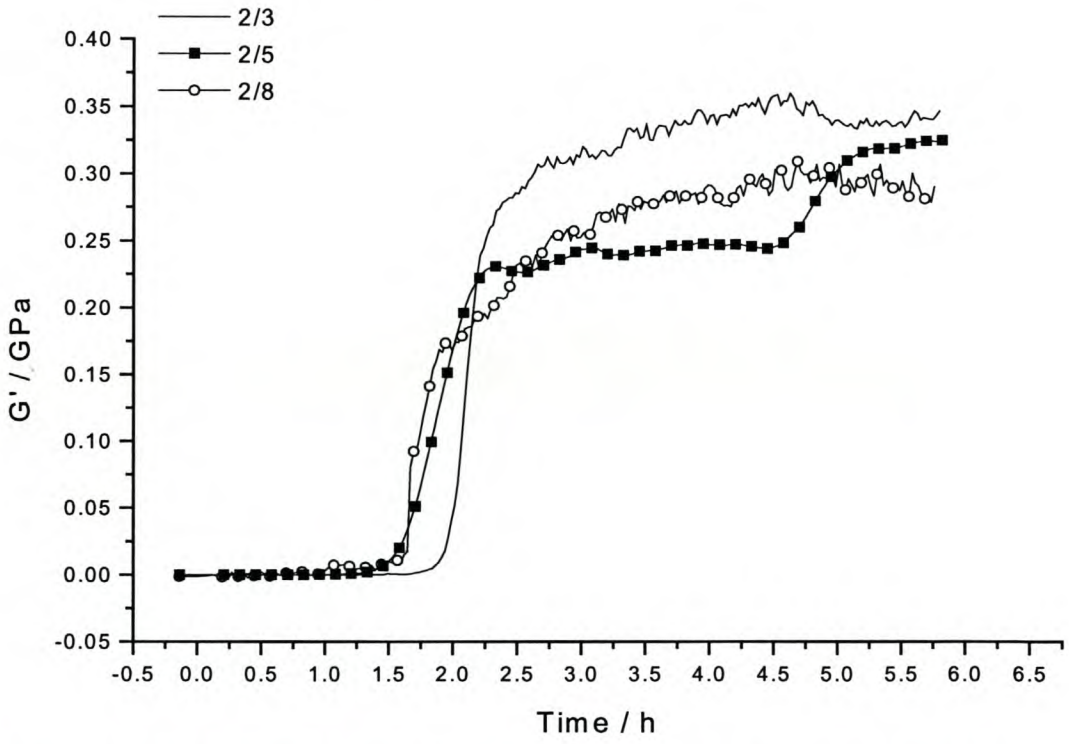

Figure 5.10: The real part of the shear modulus for core-shell polymers CS3 with different core/shell ratios. Symbols mark every 20th measurement point to be able to differentiate between the curves.

5.1.5 Comparison of Different Particle Sizes

Core-shell polymers with crosslinked core and particle diameters ranging from 69 nm to 320 nm were prepared to investigate the influence of the particle size on the film formation.

Figure 5.11 displays the particle diameter as a function of temperature. For all polymers the diameter starts to increase at about 8-10°C, which corresponds well to the predicted shell T_g of 6.2°C. The diameter of the cores does not change since they are crosslinked.

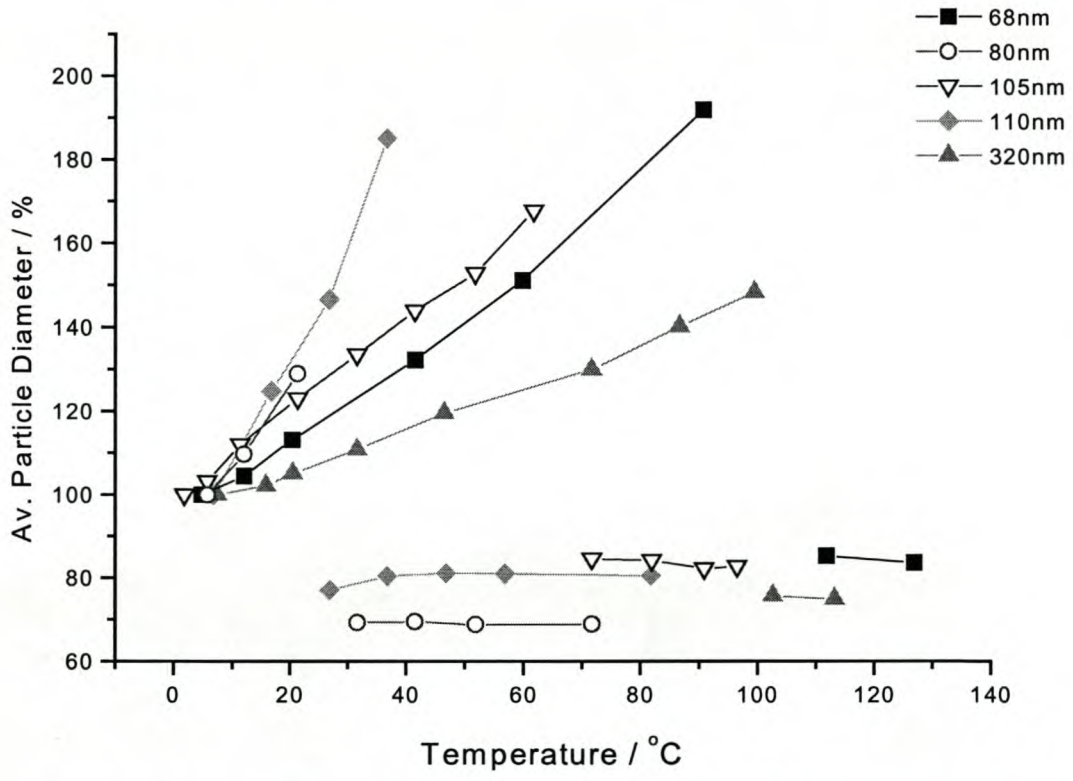

Figure 5.11: Particle diameter of core-shell polymers CS3 produced with different surfactants (resulting in different particle sizes) as a function of temperature.

The increase of particle diameter with temperature shows no correlation with particle size but it can be seen that the particles made with a particle diameter of 80nm film-form better than the other particles. This may be due to the different types of surfactants used to achieve the different particle sizes. The latex with a particle diameter of 80nm was produced with B27 (hollow circle). The particles start to coalesce and film-form already at 20°C and the cores appear at the surface at 25°C. The particles produced with the blended surfactants (B27+B29) (hollow down-triangle, diamond) also deform very fast and form a smooth film. The cores of the 110nm particles appear at 25°C at the surface and the cores of the 105nm particles at 65°C. The particles manufactured with the surfactant B25 that have a diameter of 68nm (black square) grow slower with increasing temperature. The cores become

visible at about 110°C. The particles made with the surfactant B29 (black up-triangle) show the slowest increase in particle diameter with temperature. The cores of these particles only become visible at about 100°C.

The surface corrugation - or peak to valley height of the polymer particles - decreases with increasing temperature, see Figure 5.12.
A clear dependence of the surface roughness on the particle size can be seen. The surface of the film with the smaller particles flattens faster compared to the surface of the film with larger particles. The emulsions with smaller particles form also a much smoother film with less surface corrugation.
The smaller particles seem to coalesce more easily than the larger ones, which is in good agreement with the theoretical predictions of, for example, [4] and [5].

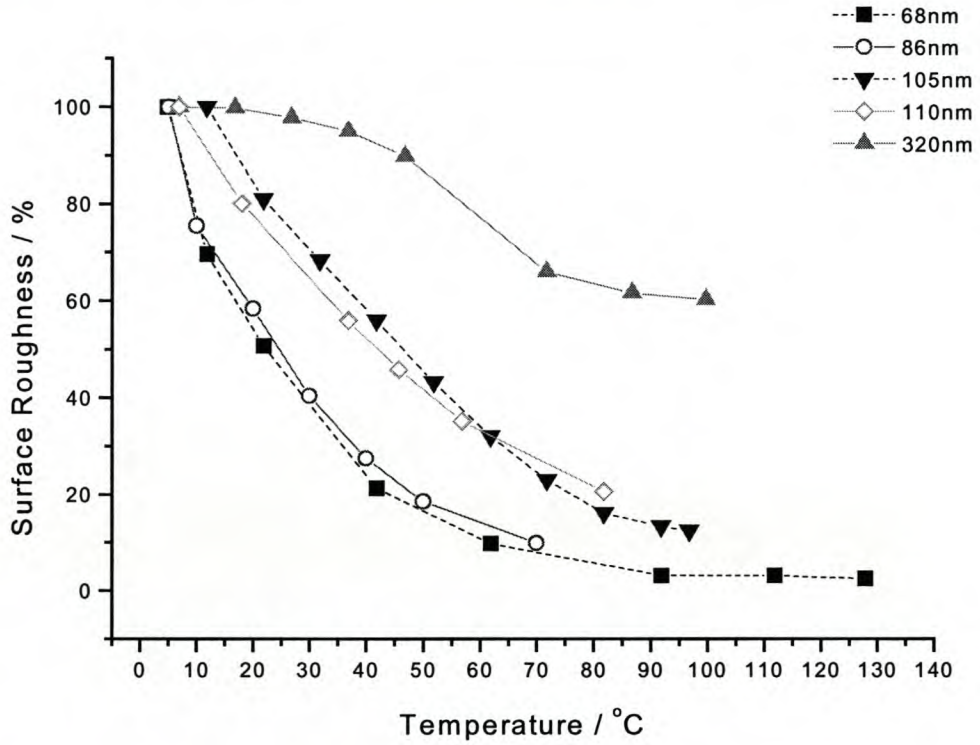

Figure 5.12: Surface corrugation of core-shell latices CS3 with different particle size as a function of temperature for the different particle sizes.

The time-dependent growth behavior of the polymer particles shows a clear relation to the particle size, as shown in Figure 5.13.
It is clearly evident that the smaller particles deform sooner, and to a larger extent, and flow with greater ease than the larger particles.

According to the theories of Dillon [4] and Brown [5], our experimental results show that the smaller particles coalesced more easily than the larger ones and that they are deformed to a larger extent. This confirms the theory of Kendall and Padget [6], that the deforming force is inversely proportional to the particle radius. It also confirms the findings of Jensen et al. [7], namely that the MFT increases with the

particle diameter. Since the MFT marks the temperature at which film formation starts, these results can be related to the findings of the AFM measurements, which show that latices with smaller particles start to filmfom at lower temperatures than latices with larger particles. In other words, the ability to form a film decreases with increasing particle size. This corresponds well with the theory of Kan [8], Goh [9], and Goudy [10].
Experimental results show that the smaller particles are more easily deformed and flow more readily than the larger particles do.

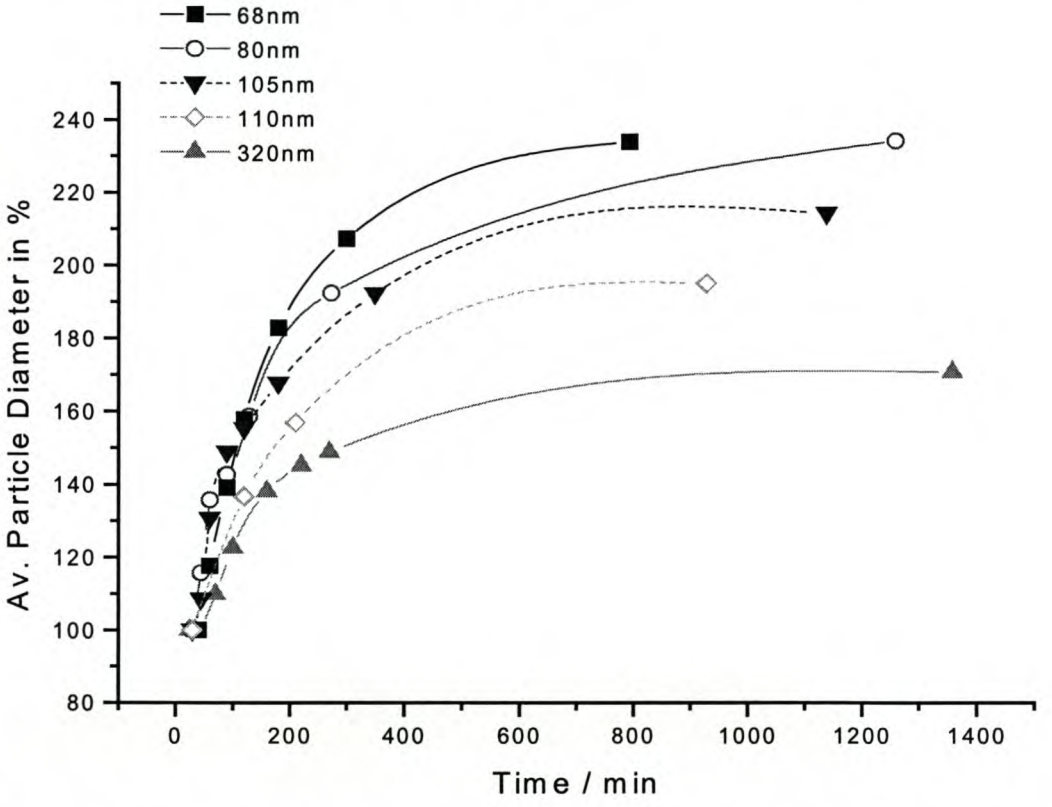

Figure 5.13: Increase in particle diameter of core-shell polymers CS3 with different particle size, as a function of time.

These findings were confirmed by ultrasonic shear wave measurements, as displayed in Figure 5.14.
The smaller particles film-form faster than the larger particles. The water evaporates quickly from the samples with larger latex particles (105nm and 320nm) and the final value of the shear modulus is soon reached. The second stage of film formation, the water diffusion through capillaries, is hardly recognizable. The second stage of water evaporation, before the final value of the shear modulus is reached, is more pronounced for the dispersions with smaller particles (68nm, 80nm).
The hardness of the film seems to depend on the particle size as well as the film formation kinetics. The shear modulus of the dried film is greater for dispersions with larger particles. This is to be expected, since the core/shell ratio of all compared latices particles is constant. This means that the relative amount of hard core polymer per particle is increasing similarly to the particle diameter.

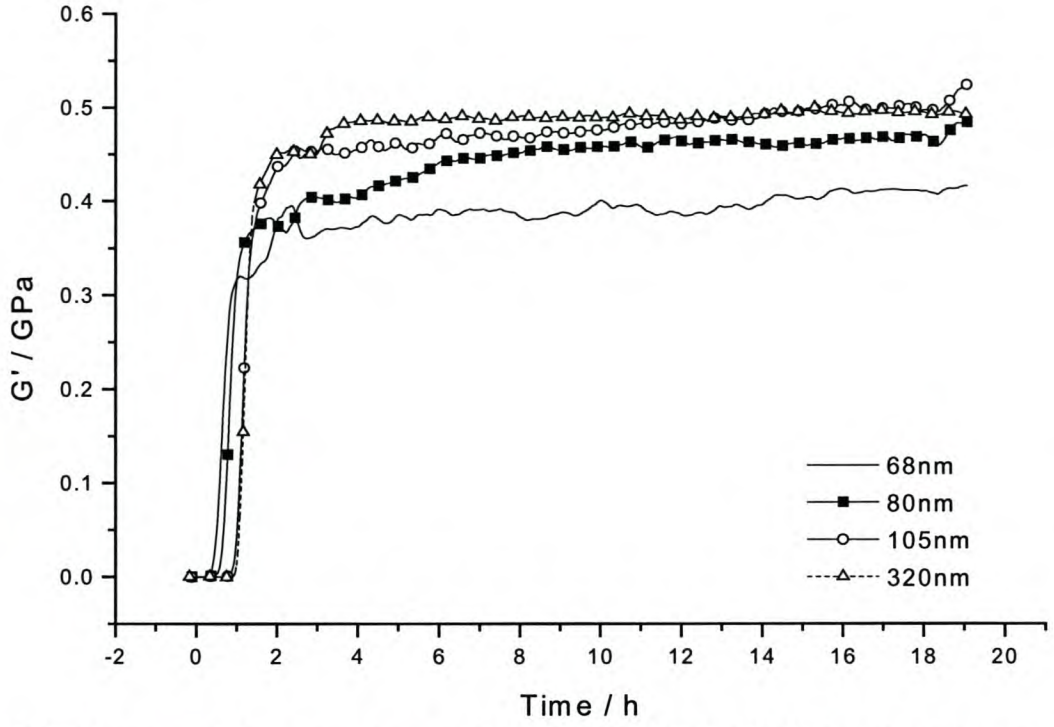

Figure 5.14: Shear modulus curves for core-shell polymers CS3 with different particle sizes. Symbols mark every 20th measurement point to be able to differentiate between the curves.

The deformation and film formation behavior of polymer particles was investigated by AFM and ultrasonic shear wave reflection. The theoretical model of particle coalescence by Kendall and Padget [6] was experimentally confirmed.

Comparison of different polymer structures containing the same monomers shows that core-shell polymers with a soft shell around a hard core filmform faster than, for example, a conventional unstructured latex. This is due to the fact that the soft core polymer with a low T_g of about 2°C starts interdiffusing earlier and flows more easily than the polymer in a conventional polymer with a higher T_g.

The effect of the shell thickness in a core-shell polymer found by Morgan et al. [3] could not be confirmed by AFM measurements. Polymers with different core-shell ratios were found to behave in a very similar manner, following the same trends for particle deformation.
Unlike the AFM results, the ultrasonic shear wave measurements show a difference in the film formation behavior, depending on the core/shell ratio. Latices with a smaller core/shell ratio, and therefore a thicker shell, filmform faster than latices with a higher core/shell ratio. Latices with a higher core/shell ratio (that means a thinner shell) reach a higher end-value for the shear modulus than particles with a smaller core/shell ratio. This is due to the fact that the particles with a greater core/shell ratio, e.g. 2/3, contain comparably more of the high T_g polymer, which seems to reinforce the film.

The film formation behavior was found to depend strongly on the particle size – the smaller particles coalesce faster than the larger ones. This corresponds well with the theory of [5] and [6] and the experimental results from [7-10]. The surface corrugation also shows a dependence on the particle size. The surface corrugation of smaller particles decreases faster and the resulting film is flatter than that of larger particles. The US measurements confirmed these findings. The smaller particles film-formed faster than the larger particles. The results also show that films formed by larger particles were harder than films formed by smaller particles.

5.1.6 The Influence of Coalescent Solvents

The influence of three different coalescence solvents on the film formation behavior of the unstructured latex UL1 was investigated. A coalescent solvent is expected to improve the film formation behavior of the latex, and thus a difference in the particle deformation is expected.
The coalescent solvents compared were:

- Fluiden, a mineral turpentine from Aktol,
- UCAR, an ester-alcohol from Union Carbide
- Ethyleneglycol monobutylether 2 butoxyethanol (EGMBEBE) purchased from Sigma Aldrich.

The coalescent solvents were added in amounts of 1%, 2% and 4% of the solid content of the latex.

5.1.6.1 1% Coalescent Solvent

1% coalescent solvent relative to the solid content of the unstructured latex UL1 was added to the dispersion.

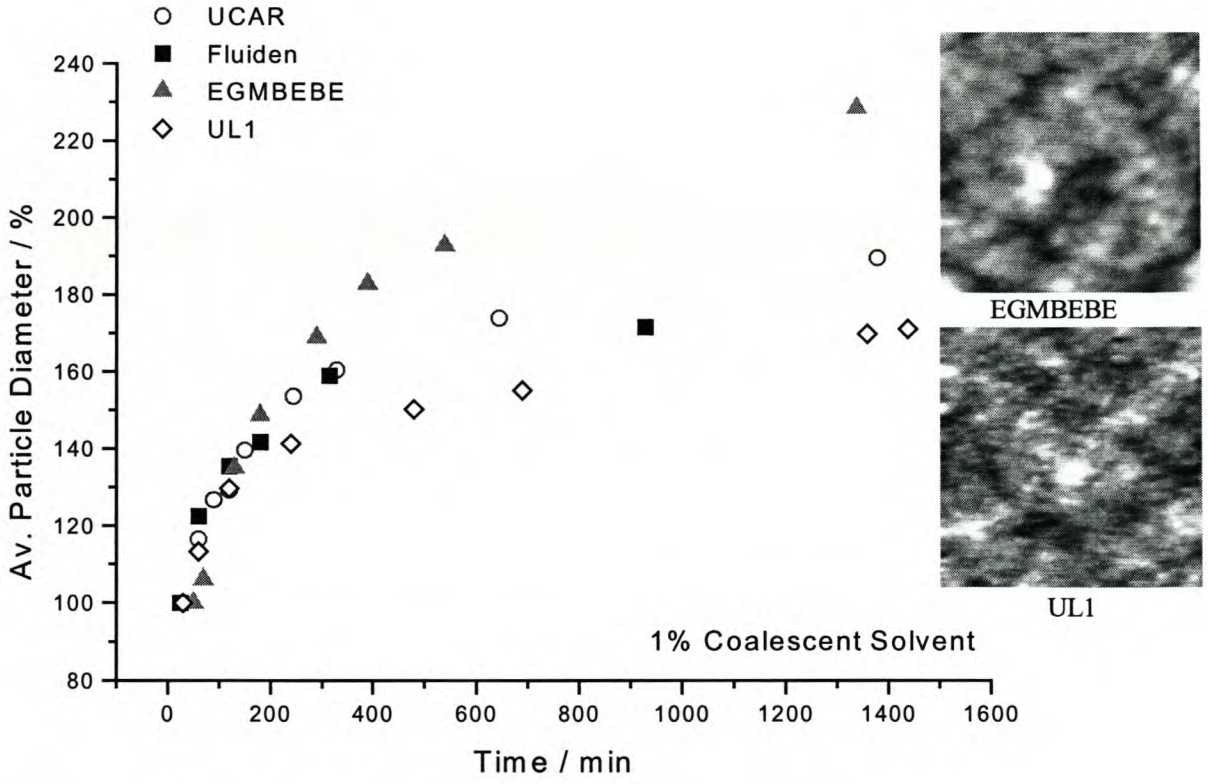

Figure 5.15: Influence of 1% coalescent solvent added to UL1 on particle deformation. The insets display AFM images of the surface of the pure latex UL1 and the latex with added EGMBEBE after 24 hours.

Figure 5.15 shows that the dispersion with EGMBEBE filmforms faster than the dispersions with the two other coalescent solvents. There is very little difference in the influence on film formation between Fluiden and UCAR. However, all three coalescent solvents enhance the film formation kinetics compared to the blank latex UL1 (hollow diamond).The latices with added coalescent solvent deform and interdiffuse to a greater extent, which results in a smoother surface. This can be seen in the AFM images in Figure 5.15 and in the larger final particle diameter of the latex with added coalescent solvent.

5.1.6.2 2% Coalescent Solvent

2% coalescent solvent relative to the solid content of the unstructured latex UL1 was added to the dispersion.

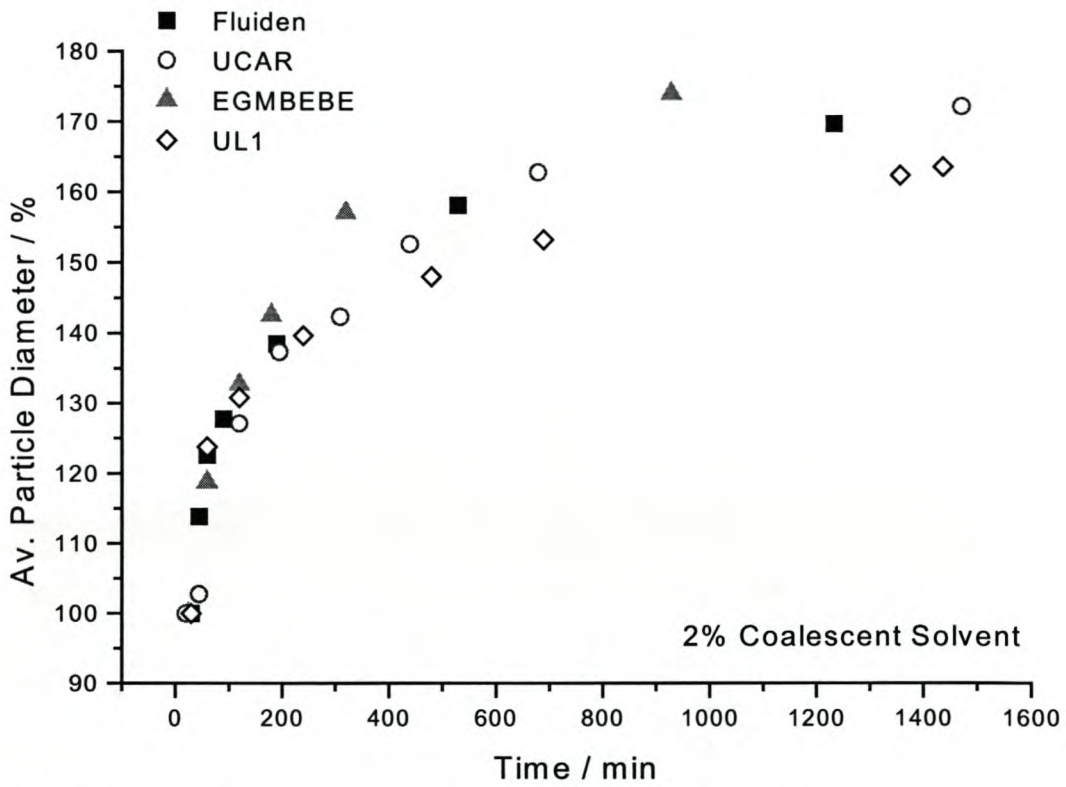

Figure 5.16: Influence of 2% coalescent solvent added to UL1 on particle deformation.

The three different coalescent solvents enhance the film formation behavior of the unstructured latex UL1. The particles are deformed to a greater extent than in the pure latex (hollow diamond). Figure 5.16 shows that the dispersion with EGMBEBE filmforms faster than the dispersions with the two other coalescent solvents. There is again very little difference in the influence on film formation between Fluiden and UCAR.

5.1.6.3 4% Coalescent Solvent

4% coalescent solvent relative to the solid content of the unstructured latex UL1 was added to the dispersion. Figure 5.17 shows that, again the coalescent solvents enhance the film forming properties clearly. The dispersion with EGMBEBE filmforms better than the dispersions with the two other coalescent solvents. There is a small difference in the influence on film formation between Fluiden and UCAR; the dispersion with Fluiden added filmforms slightly better than the dispersion with UCAR. The particles of the pure latex UL1 deform less than the particles of the latices with added coalescent solvent.

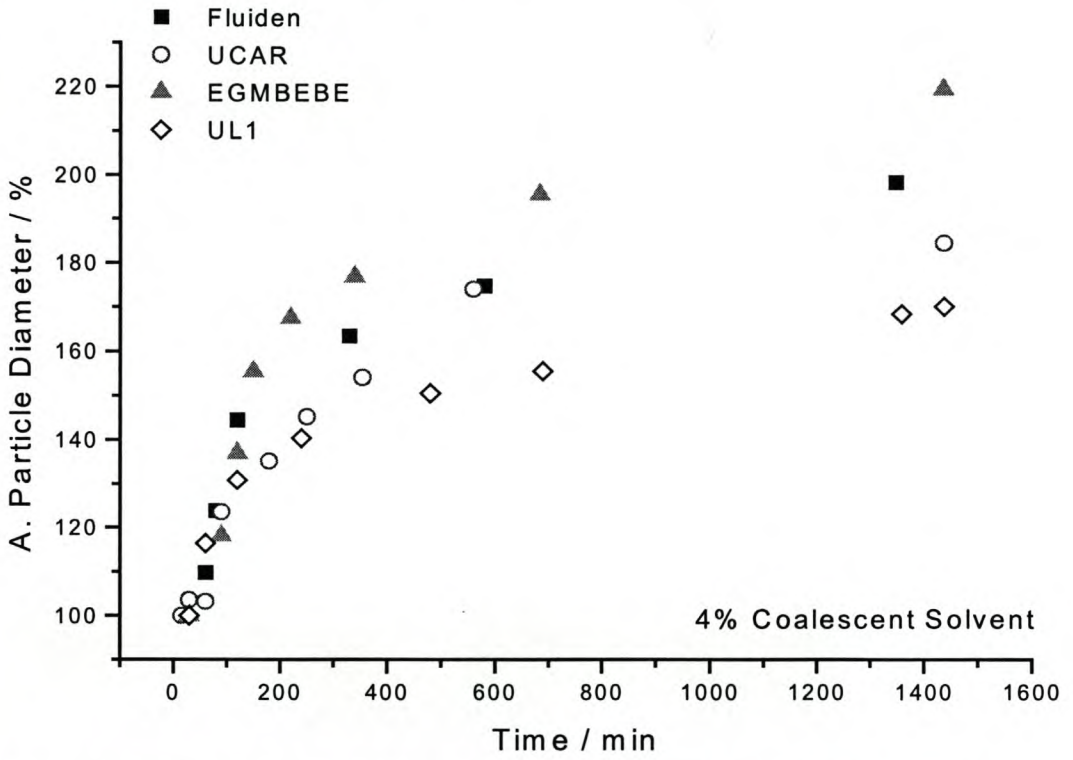

Figure 5.17: Influence of 4% coalescent solvent added to UL1 on particle deformation.

Surprisingly, the amount of the coalescent solvent at these levels has hardly any influence on the film formation, as displayed in Figure 5.18 – 5.20. For all three solvents the particle deformation is clearly enhanced by the addition of coalescent solvent compared to the pure latex. But it seems that the film formation kinetics and the particle deformation are not greatly affected by the amount of added coalescent solvent. Higher amounts than 4% of coalescent solvent are expected to yield more conclusive results.

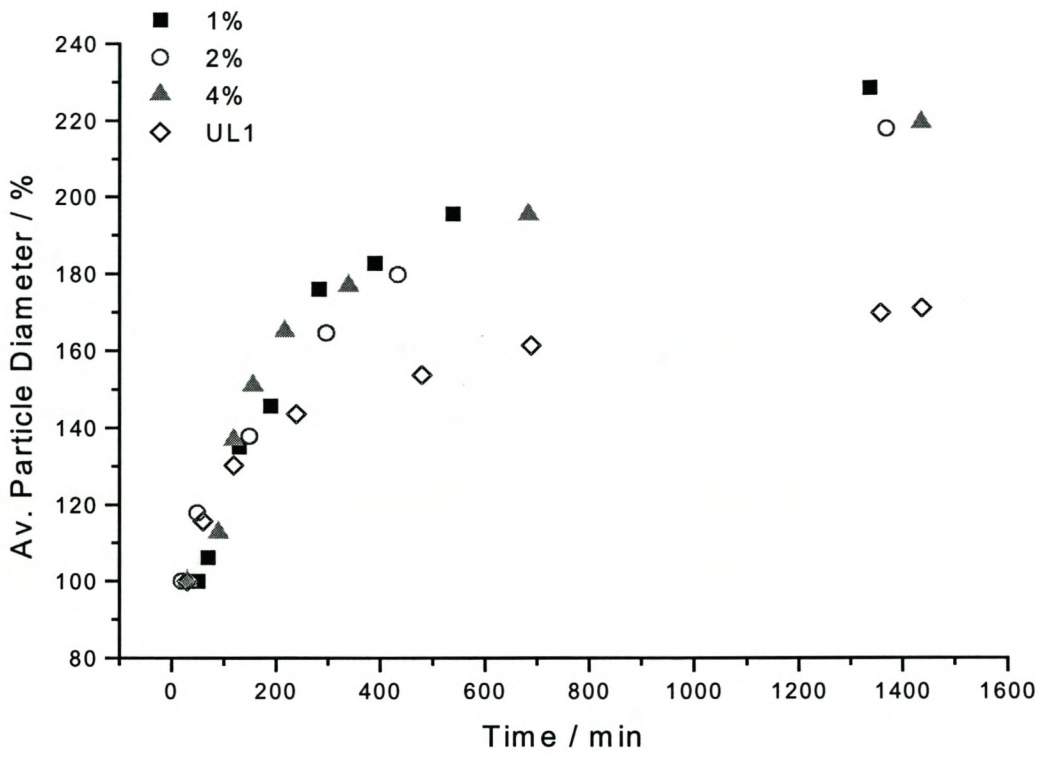

Figure 5.18: Particle deformation of UL1 with 1%, 2% and 4% EGMBEBE added.

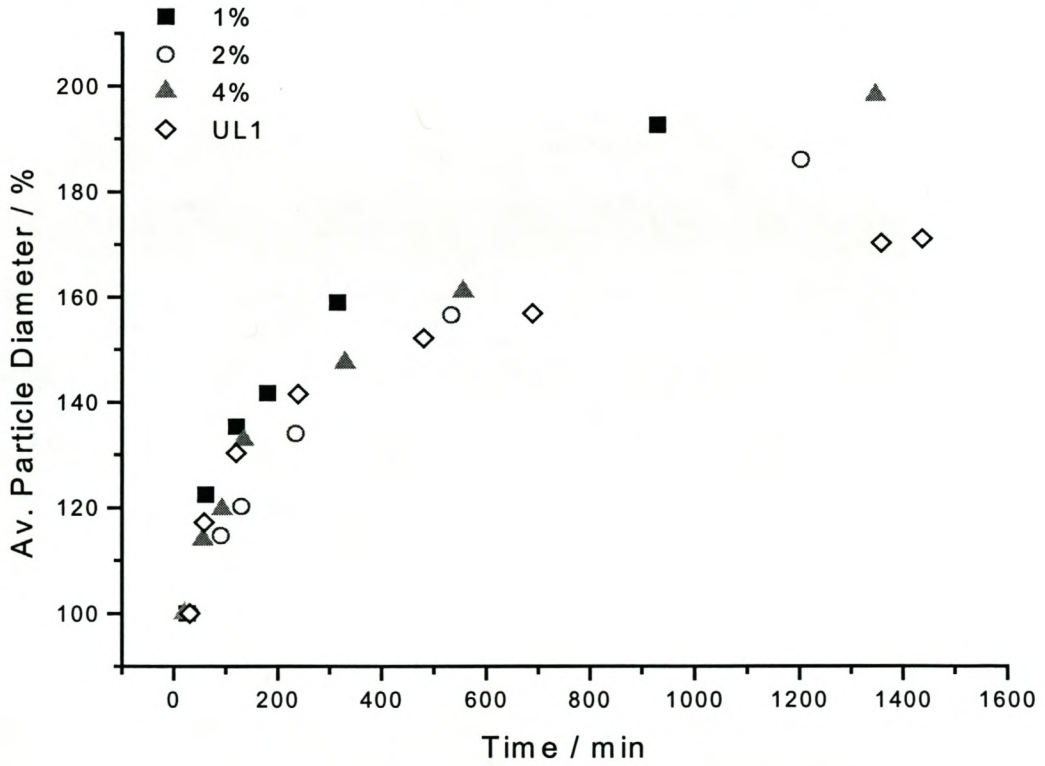

Figure 5.19: Particle deformation of UL1 with 1%, 2% and 4% Fluiden added.

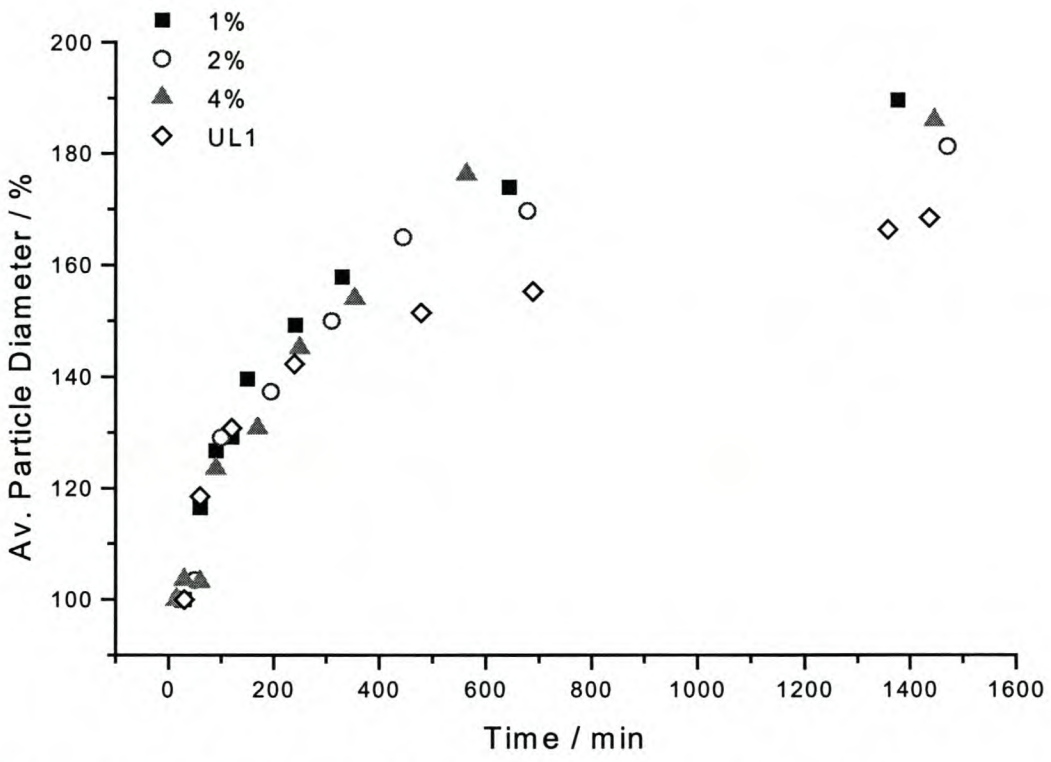

Figure 5.20: Particle deformation of UL1 with 1%, 2% and 4% UCAR added.

The AFM measurements show consistently that the surfactant EGMBEBE leads to a larger particle deformation and a better film formation than the other tested coalescent solvents. The amount of coalescent solvent, at least below 4%, in the latex seems to have little influence on the particle coalescence.

Results of the ultrasonic shear wave measurements also show a difference in the film formation behavior between the three added coalescent solvents. Films of the latex UL1 with 2% coalescent solvent were investigated. Unfortunately no results for the pure latex were obtained.
The film formation kinetics for all three samples is comparable. This is in agreement with the AFM results, which showed an equal particle deformation function with time. All three curves reach the second stage of water evaporation at the same time, after about 2 hours. The maximum value of the shear modulus is only reached after about 13 hours.
The hardness of the films, characterized by the maximum value of the shear modulus is quite different. Figure 5.21 displays the shear modulus during drying for dispersions with 2% added coalescent solvent.
The curves are very noisy, but the general trend is recognizable. The dispersion with added EGMBEBE forms the hardest film once it has dried. The film of the dispersion with UCAR reaches nearly the same hardness but the film formed by the dispersion with Fluiden is much softer, which means that the film containing Fluiden probably contains this coalescent solvent for a longer period.

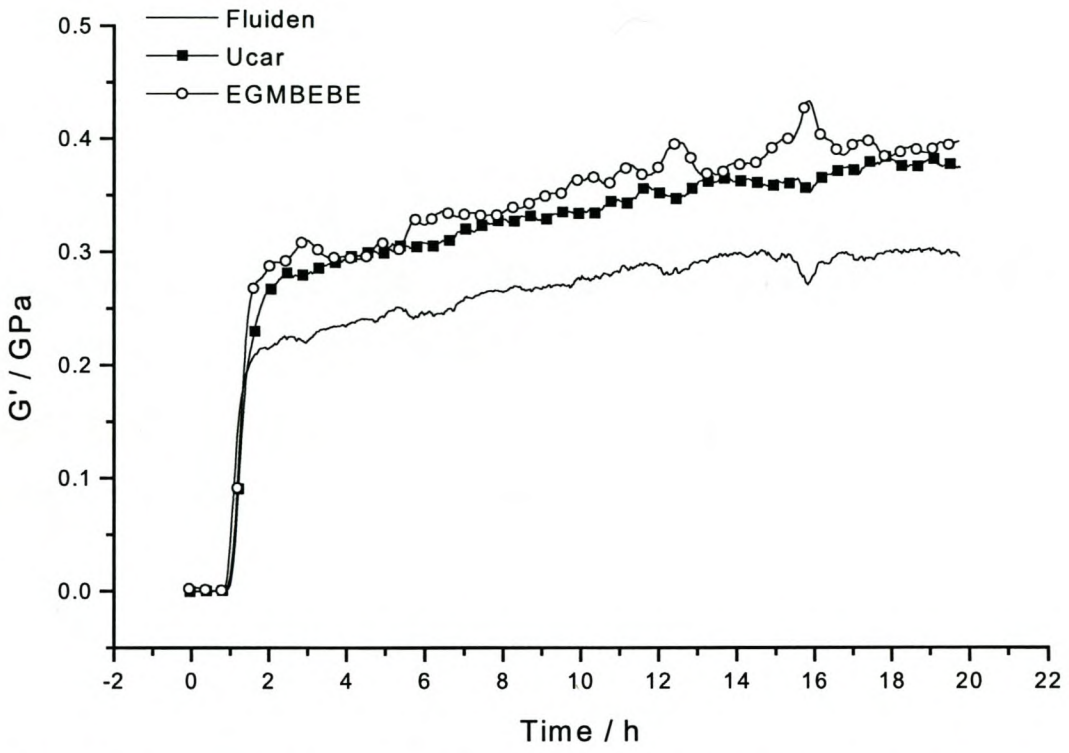

Figure 5.21: Shear modulus of dispersions of UL1 with 2% added coalescent solvent. Symbols mark every 20th measurement point to be able to differentiate between the curves.

It seems that the main influence of the coalescent solvent is to elongate the second stage of water evaporation, represented by the slowly ascending curve before the plateau is reached. The water evaporation through the dry membrane formed at the film surface lasts about 10 hours. This effect cannot be seen by AFM studies, since it does not influence the particle diameter or the interdiffusion of latex particles at the surface.

5.1.7 Influence of Rheology Modifiers

Rheology modifiers were added, to change the flow properties of the latex. These modifiers are HASE (hydrophobically modified alkali-soluble emulsion) thickeners that form a three-dimensional network with the latex particles and modify the rheological properties of the latex.

For the systems investigated, two rheology modifiers were used:

(1) a conventional thickener, consisting only of MMA and MAA in the polymer backbone;
(2) a hydrophobically-modified thickener, with the same backbone as (1) and incorporated macromonomers, which contains ethylene oxide spacer units with terminal hydrophobic end-groups. These side chains interact with the latex particles and help to form the three dimensional network.

1.6% of these modifiers were added to the unstructured latex UL1 and the core-shell latex CS3. The influence of each additive on the film formation is distinctly different.

The conventional thickener (1) consists only of a backbone and does not attach to the latex particles. It is apparent in the AFM images in Figure 5.22 that a phase separation takes place, as suggested by Shay [11]. The thickener coagulates and forms large patches separate from the latex particles during film formation. According to Shay et al. the water-soluble thickener is repelled from the polymer particles due to osmotic pressure and aggregates in thickener rich domains. This might explain the problem of increased water sensitivity after application of the thickener in paint.

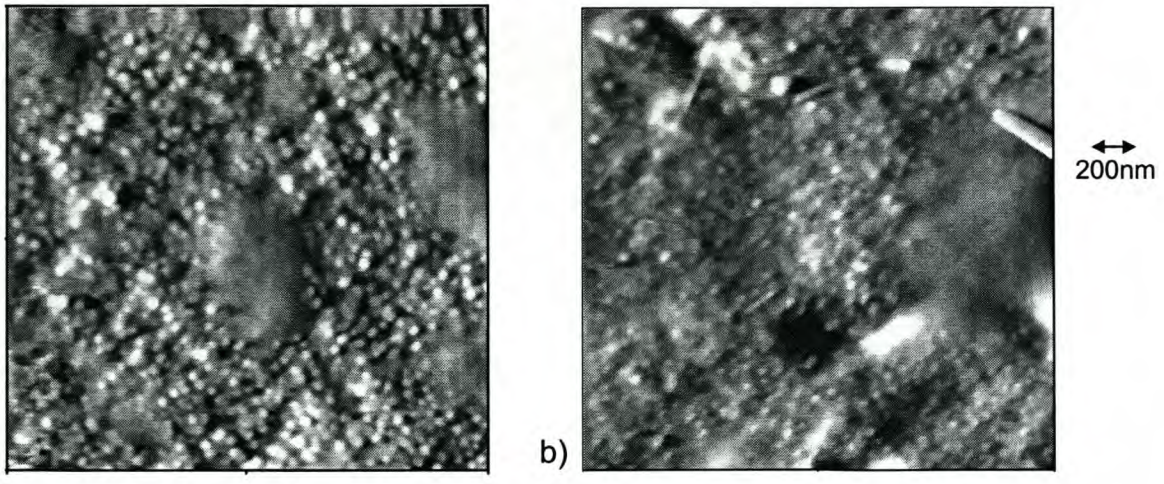

Figure 5.22: Latex particles with added conventional thickener: a) UL1 and b) CS3. The latex and the thickener do not mix.

The HASE thickener (2), which contains the associative macromonomers, shows no visible phase separation in the AFM images (see Figure 5.23). This is due to the three-dimensional network that is formed between the latex particles and the HASE thickener.

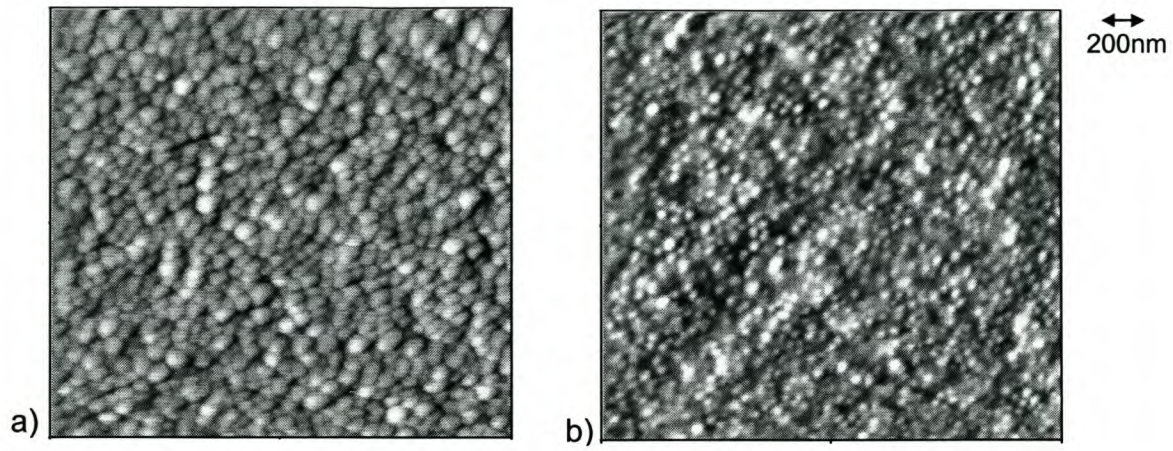

Figure 5.23: Latex particles with added HASE thickener (2). a) UL1 and b) CS3.

The deformation behavior of the latex particles is not influenced to a great extent by the thickener. In the unstructured latex UL1 all particles deform at the same rate, as displayed in Figure 5.24.

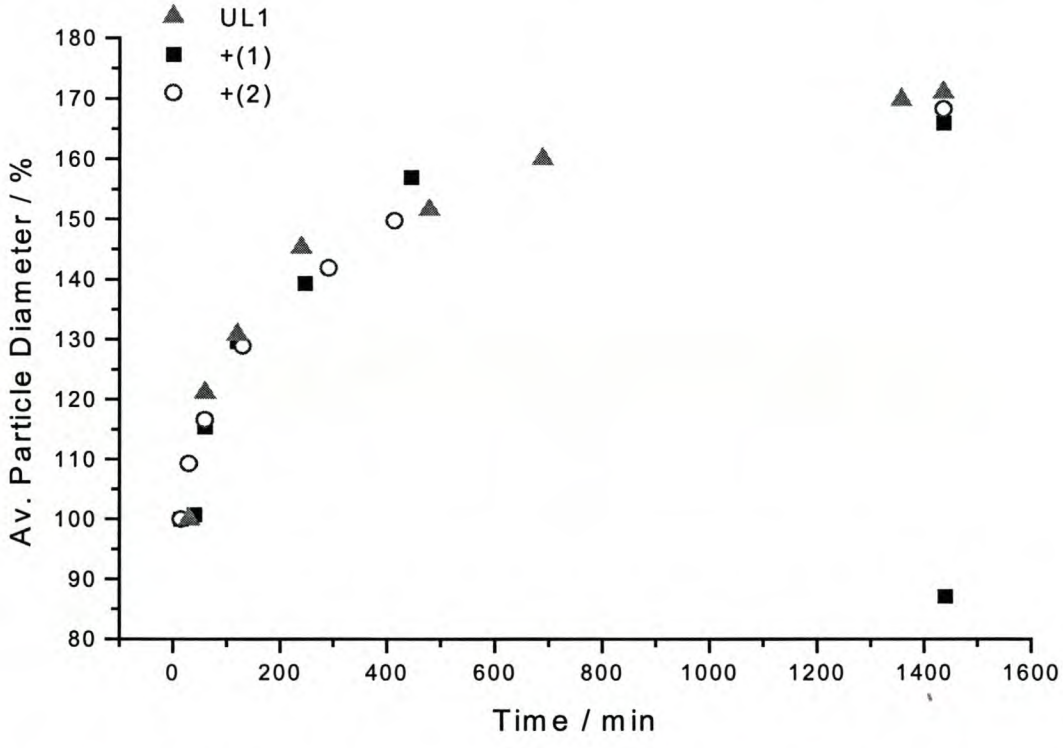

Figure 5.24: Deformation behaviour of UL1 with the different added thickeners (1) and (2).

Changing the flow properties of a latex, characterized by the viscosity, as a function of shear stress does not necessarily mean that the deformation and film formation behavior of the latex particles will be changed. The amount of the added rheology modifier was with 1.6% also very small, larger amounts might influence the particle deformation behavior.

For the latex CS3 however the film formation behavior is affected by the addition of the thickener, as displayed in Figure 5.25:

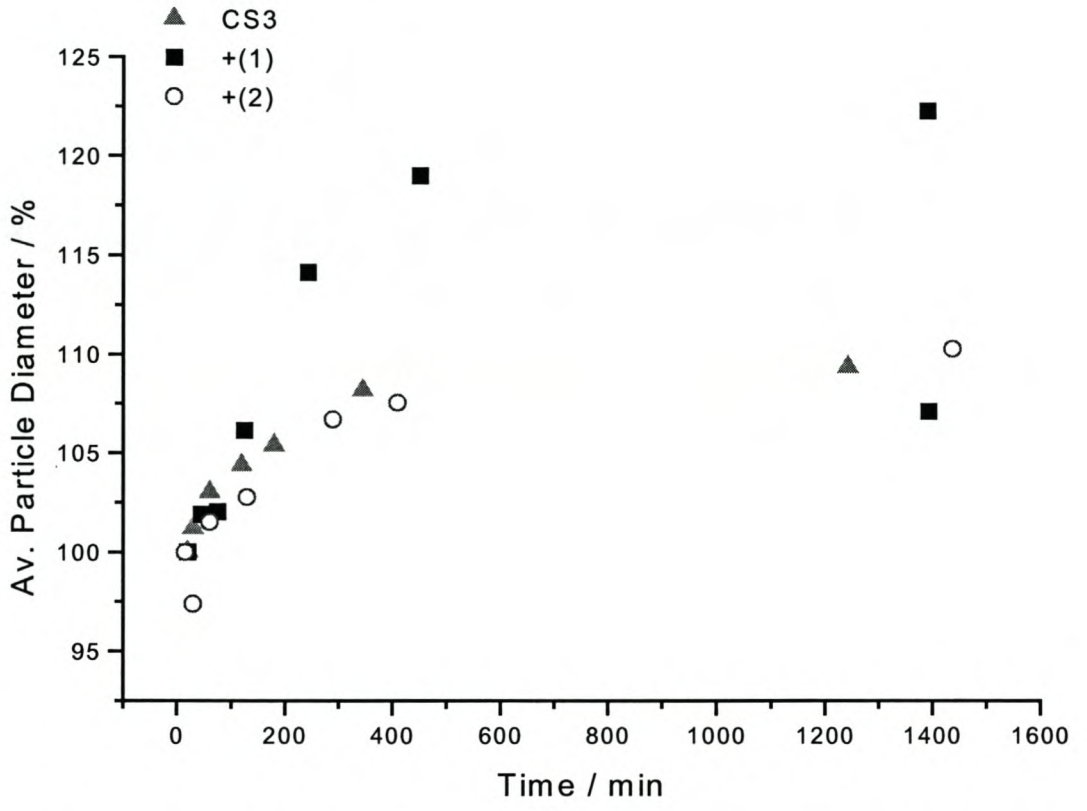

Figure 5.25: Deformation behaviour of CS3 with the different added thickeners (1) and (2).

The latex containing the conventional thickener (1) deforms much faster than the pure latex or the latex containing the HASE thickener (2). This is due to the phase separation of the conventional thickener, the few visible latex particles at the surface are surrounded by the added modifier, which segregates to the surface, coagulates there and finally covers the latex particles.
After about 24 hours the cores become visible between the shell-polymer phase and the patches of conventional thickener, so two particles sizes could be determined. No cores become visible in the latex with the HASE thickener (2).

5.2 Scanning Thermal Microscopy (SThM)

In the course of the studies it was attempted to use SThM for the thermal characterization of polymers, especially latices with different polymer phases, like core-shell polymers. The SThM [12] allows to map the surface temperature, or the heat capacity of the surface simultaneously with the topography, as described in chapter 3.3. Different polymer phases of a core-shell latex with, for example, a hard core and a soft shell could be detected due to their different heat capacity. An image sequence acquired with increasing temperature would allow to "follow" the different polymer phases, as they start flowing with increasing temperature.
The biggest problem in the experiments was the size, and with that the lateral resolution of the thermal tip. The thermal probes used for the experiments consist of a bent Wollaston wire, as described in chapter 3. The dimensions of the wire loop at the tip are about 5μm in diameter, with an effective contact area on a flat surface of about 30 to 300nm. This is still far too big to detect polymer particles with a diameter in the range of 50nm. The core-shell particles of interest typically had a diameter of 70nm to 110nm with a core diameter between 40nm and 80nm. Only the largest particles with a shell diameter of 320nm and a predicted core diameter of 210nm could be determined with SThM, as displayed in Figure 5.25.

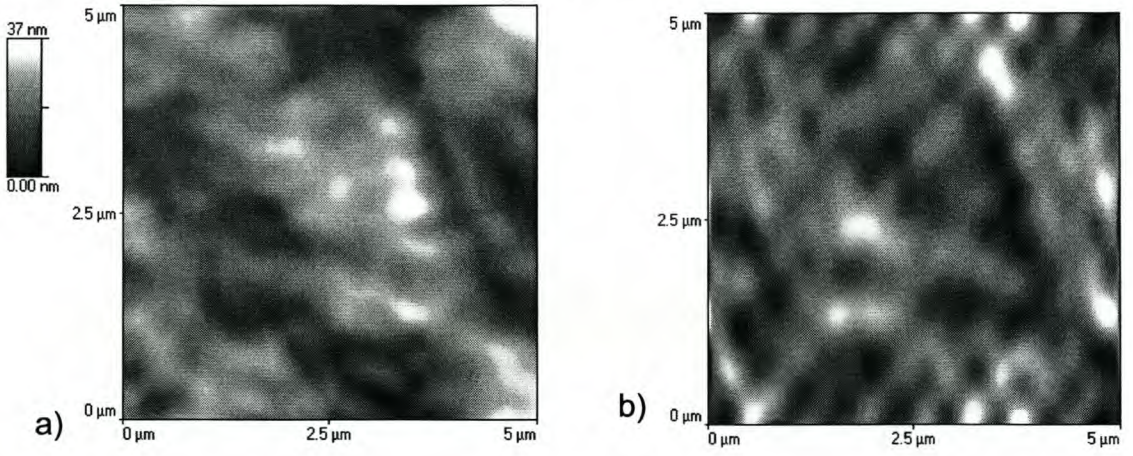

Figure 5.25: Topography (a) and heat capacity (b) of a core-shell latex CS3 with a particle diameter of 320nm at a temperature above the shell T_g (about 30°C).

It can be seen that the topography image (a) shows little indication if the visible polymer is part of the shell or the core of the latex particles. The thermal image (b), however, indicates the difference of the two polymer phases very well. The high T_g cores have a lower heat capacity than the low T_g shells; thus they appear in the thermal image as darker spots. The diameter determined from the thermal image corresponds well to the predicted diameter of 210nm.

5.3 Bibliography

[1] Pusey,P., vanMegen,W., Bartlett,P., *Physical Review Letters*, 1989, **63**, 2753
[2] Rieger,J., Haedicke,E., Lindner,P., *Physical Review Letters*, 1992, **68**, 2782
[3] Morgan,L., *Journal of Applied Polymer Science*, 1982, **27**, 2033
[4] Dillon,R., Matheson,L., Bradford,E., *Journal of Colloid Science*, 1951, **6**, 108
[5] Brown,G., *Journal of Polymer Science*, 1956, **22**, 423
[6] Kendall,K., Padget,J., *International Journal of Adhesion and Adhesives*, 1982, **July**, 149
[7] Jensen,D., Morgan,L., *Journal of Applied Polymer Science*, 1991, **42**, 2845
[8] Kan,C., *Journal of Coatings Technology*, 1999, **71**, 89
[9] Goh,C., Juhue,D., Leung,O., Wang,Y., Winnik,M., *Langmuir*, 1993, **9**, 1319
[10] Goudy,A., Gee,M., Biggs,S., Underwood,S., *Langmuir*, 1995, **11**, 4454
[11] Shay,G., *Surface Coatings International*, 1993, **11**, 446
[12] Fiege,G., Cramer,R., Balk,L., Reineke,F., *Proceedings 23rd int. symposium for testing and failure analysis*, 1997, 51

CHAPTER 6: Thermal Transitions of Polymers Measured by AFM

To test the accuracy of the AFM measuring thermal transitions and compare it with common methods to determine thermal transitions, polymers with known transition temperatures were investigated. In all cases the expected transition temperature of the sample was first calculated by the Fox equation (eq. 2.30). The glass transition temperature was then experimentally determined by DSC, in some cases also by DMA. These results were compared to the results obtained by the AFM resonance frequency method and confirm the accuracy of the new method.

6.1 Single Transitions

Single glass transition temperatures and melting temperatures of several polymers are determined.
The melting point of octadecane ($C_{18}H_{38}$), which is at about 30°C, appears in the resonance frequency measurement (RFM) as a sharp kink at 31.7°C, as displayed in Figure 6.1. This result is in good agreement with the theoretical predictions and the DSC result. The slightly higher transition temperature is due to the misplacement of the temperature sensor, which is mounted below the polymer film.

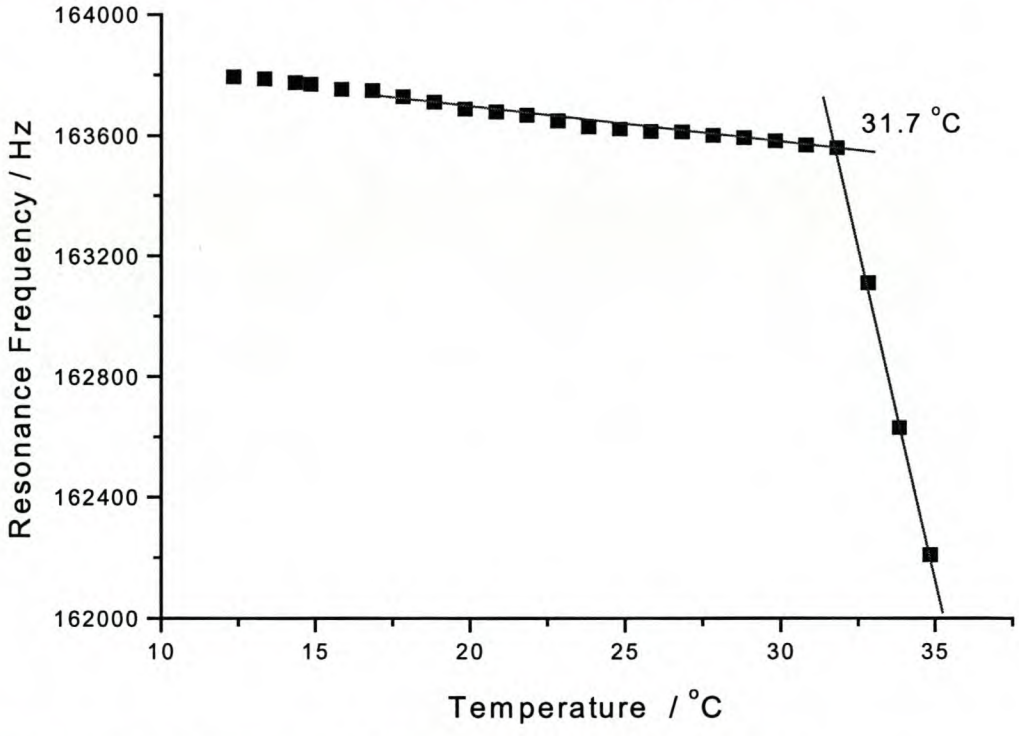

Figure 6.1: Melting temperature of octadecane determined with RFM.

The glass transition temperature of the unstructured latices UL1, UL2 and UL3 determined by AFM are displayed in Figure 6.2.

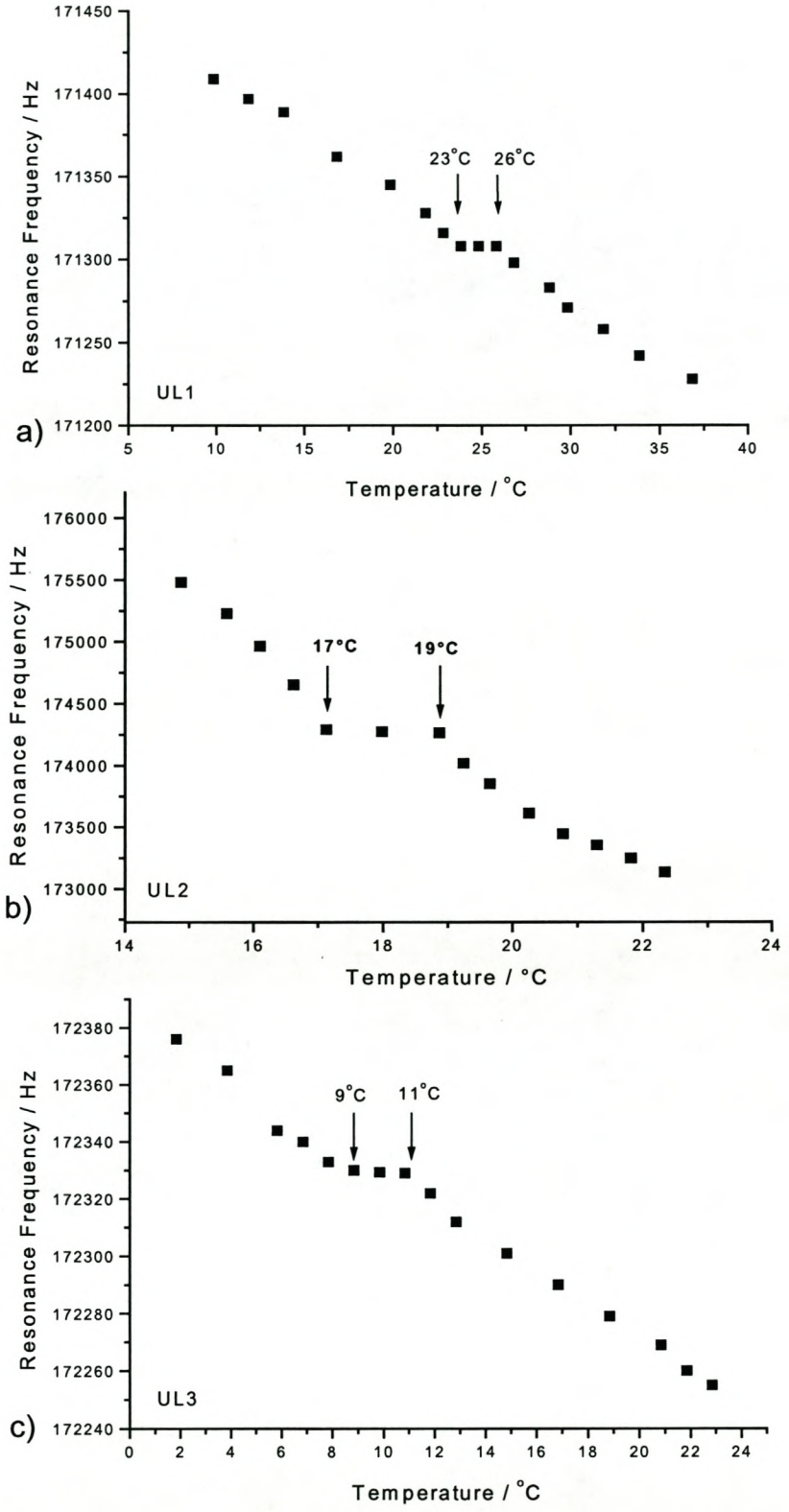

Figure 6.2: Glass transition temperatures of the unstructured latices UL1 (a), UL2 (b) and UL3 (c) determined by RFM.

The theoretically predicted glass transition temperatures are 23°C for UL1, 19°C for UL2 and 12°C for UL3.
The AFM measurements yield T_g values between 23°C and 26°C for UL1 (Figure 6.2a), 17°C to 19°C for UL2 (Figure 6.2b) and 9°C to 11°C for UL3 (Figure 6.2c). These values agree well with the predicted transition temperatures.

6.2 Multiple Transitions and Blends

Octacosane ($C_{28}H_{58}$) was used to compare the ability of resolving multiple transitions. It exists at room temperature in an orthorhombic structure and changes at 57.5°C into a rhombohedral structure with a melting point at 60.8°C [1]. DSC and RFM analyses resolve both transitions. The two peaks in the DSC curve are very close (Figure 6.3a), at 60.4°C and 62.9°C, and must be accurately measured to avoid seeing only one broad peak. The RFM curve shows two distinct kinks, at 61°C and 66°C (Figure 6.3b), which are clearly separated. The slight deviation between the transition temperatures obtained by RFM and DSC is, again due to the difference in relative proximities of the temperature sensors.

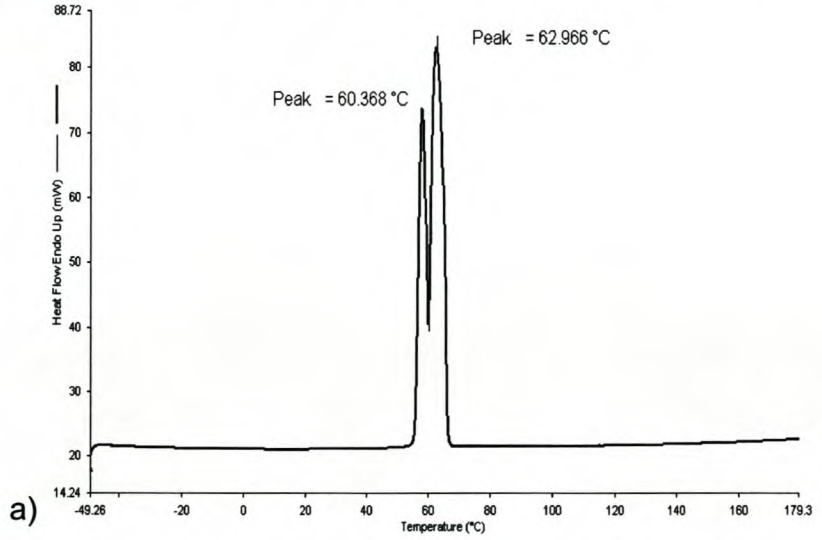

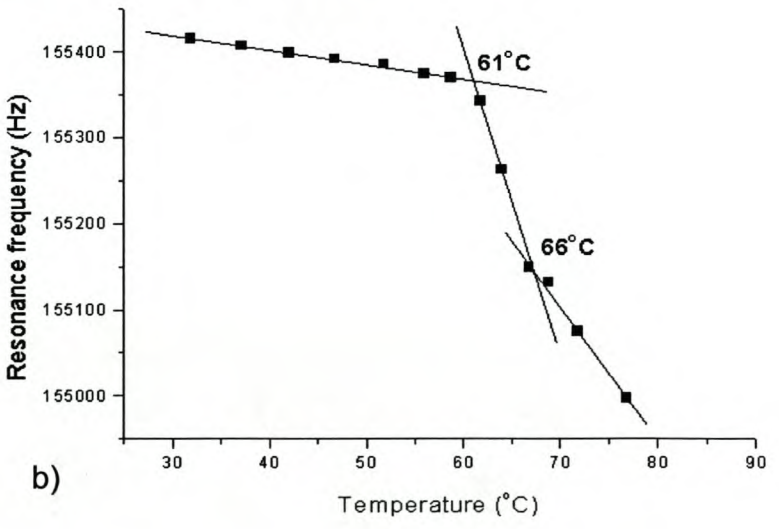

Figure 6.3: DSC (a) and RFM (b) curve showing the two transitions of octacosane.

Octadecane and octacosane were then blended in different ratios in order to compare the sensitivities of the two different analytical methods.

For the 1:1 blend both DSC and RFM analyses show the melting points of octadecane and octacosane. Both melting temperatures are observed at temperatures lower than those of the pure compounds. The DSC curve shows the transition of octacosane at 51.2°C and the more prominent octadecane peak at 28.3°C (Figure 6.4a). The RFM curve shows the octadecane transition at 29°C and the more distinct octacosane transition at 50.6°C (Figure 6.4b).

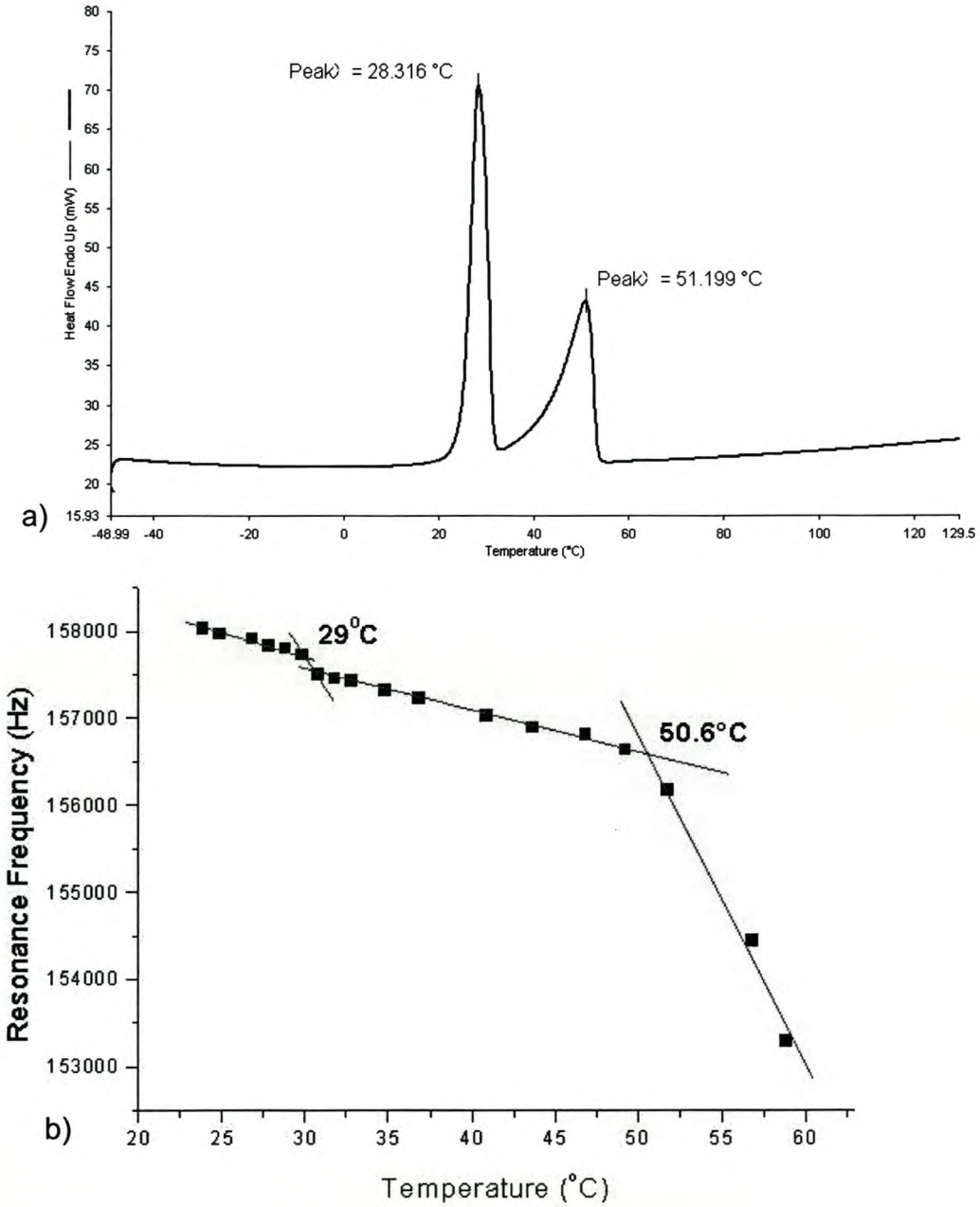

Figure 6.4: Thermal transitions of octadecane and octacosane in a 1:1 blend, measured by DSC (a) and RFM (b).

For the blend containing 5% octadecane and 95% octacosane, the DSC curve clearly shows two peaks at the expected temperatures: the melting point of octadecane is at 26.6°C, and that of octacosane is at 61.4°C (Figure 6.5a).
In the resonance frequency curve of the AFM, the melting point of octacosane at 57°C dominates (Figure 6.5b) and the octadecane transition can just be resolved.

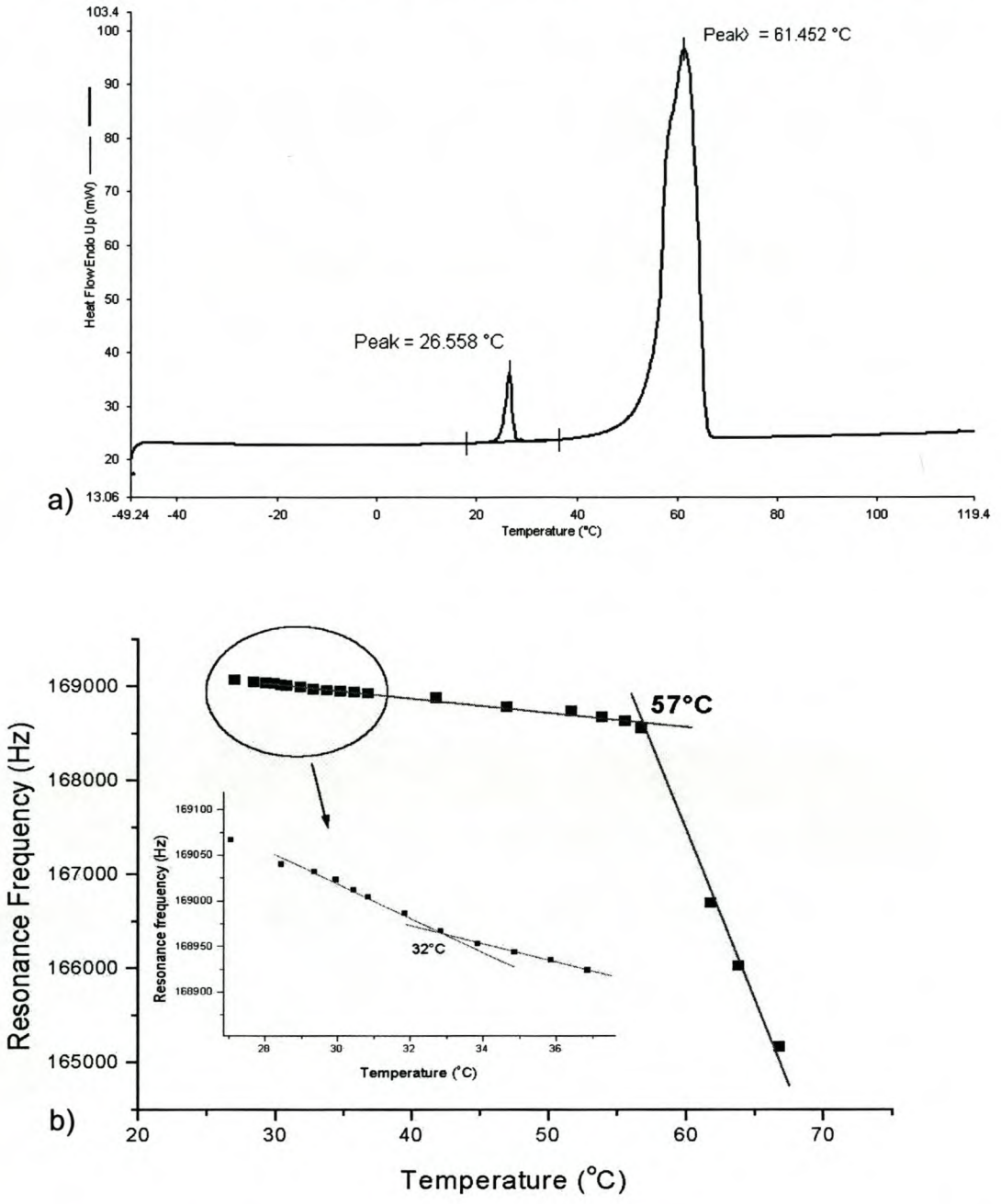

Figure 6.5: Thermal transitions of octadecane and octacosane in a 1:19 blend, measured by DSC (a) and RFM (b).

For hetero-blends of different crystalline materials, which are more or less evenly distributed over the whole sample, analysis by DSC is clearly more advantageous

than analysis by the AFM resonance frequency technique. In this case the DSC benefits from the integral measuring method.

6.3 Structured Latices

The ability of the AFM to distinguish between different polymers or polymer phases by measuring their thermal transitions on a smaller scale was investigated using structured polymers, in this case core-shell polymers.
AFM images, as shown in chapter 5.1 confirm that the polymers really do have a core-shell structure. The soft shell polymer starts flowing around the hard cores with increasing temperature. The cores become visible at the polymer surface at temperatures still below the core T_g so that the AFM tip can detect them. This explains, why the RFM method can "see" the transitions of both polymer phases, even if it is a surface sensitive method.

The first investigated sample, the core-shell latex CS2, has a soft shell, with a predicted T_g of about 3°C, and a hard core, with a predicted T_g of about 50°C.
Analysis by DSC could not resolve individual T_gs. It only shows one transition at about 20°C (Figure 6.6a), in a temperature range where no thermal transition is expected at all.
The DMA results show a shell T_g of about 19°C (onset of the first peak), which is higher than the expected shell T_g. In the DMA curve a higher temperature peak is recognizable, indicating the core polymer-phase. It is hardly possible to determine a core T_g, which is represented by the onset of the second peak, because the peaks are superposed. Extrapolation is not justified because it is not possible to determine the exact onset of the peak.

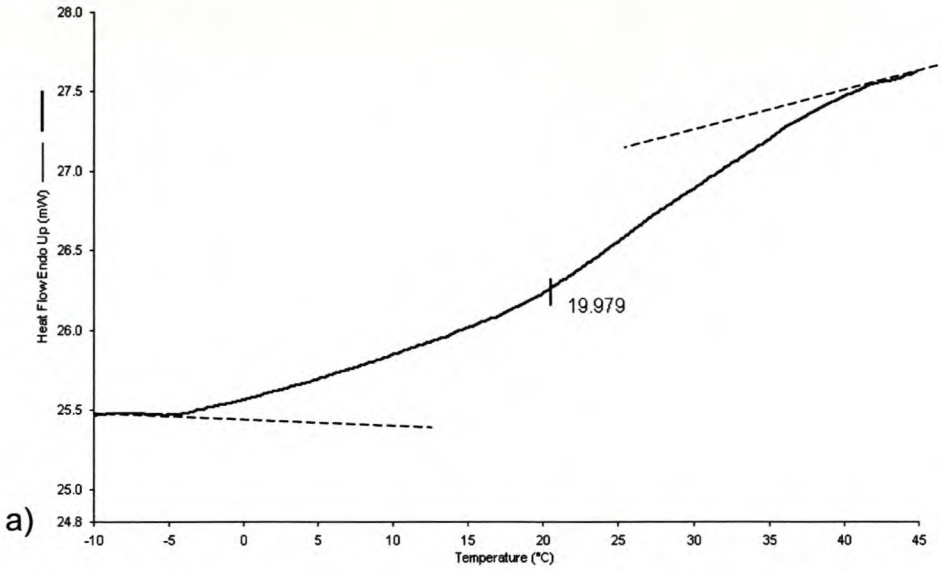

a)

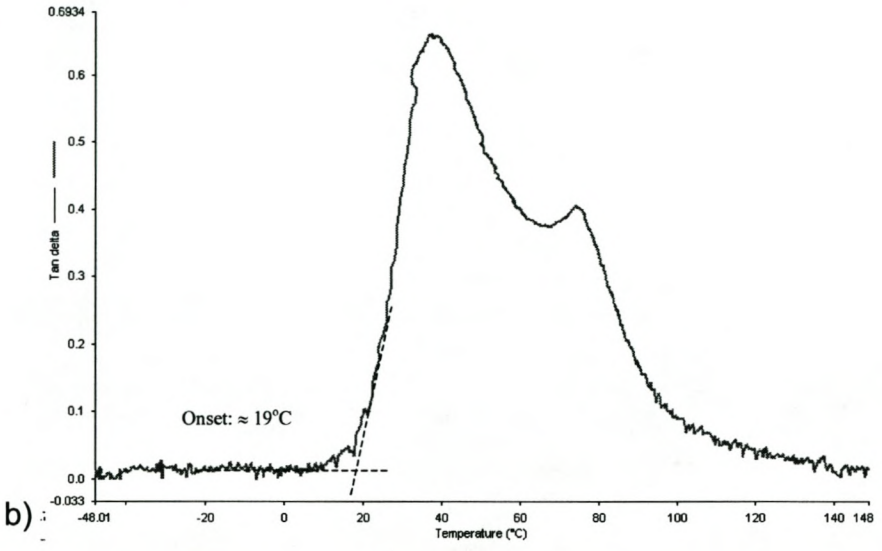

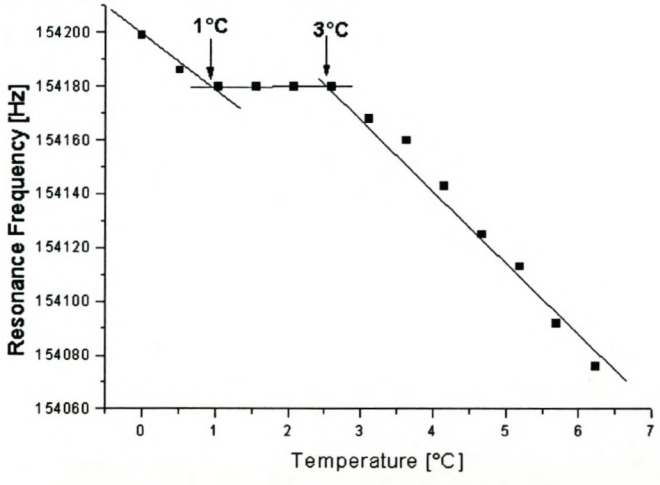

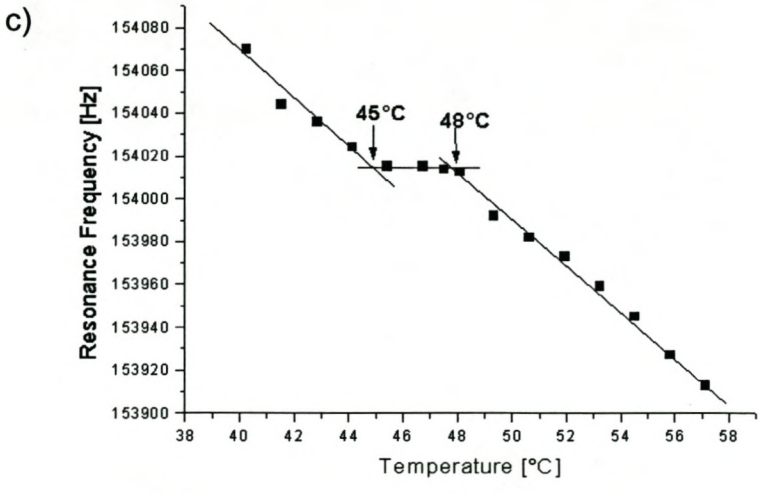

Figure 6.6: Glass transitions of the core-shell latex CS2 with a high T_g core and a low T_g shell, measured by DSC (a), DMA (b) and AFM (c).

Analysis by AFM shows two plateaus, which correspond well to the predicted glass transitions of the core and of the shell. The glass transition of the shell appeared between 1°C and 3°C and the glass transition of the core between 45°C and 48°C (Figure 6.6c). The two temperature ranges are displayed in separate graphs to emphasize the plateau regions.

To confirm these results, another core-shell polymer (CS1) with a crosslinked core and the same shell composition as before was investigated. The T_g of the shell was predicted to be about 2°C and the T_g of the core about 68°C.
The DSC shows a single transition at 20.2°C (Figure 6.7a), again in a temperature range where no transition is expected.
The transition temperatures obtained by DMA (Figure 6.7b) are not well defined. Two peaks are visible but they are, again, superposed. The onset of the lower peak is at about 10°C, which is higher than the expected shell T_g. The onset of the second peak is not visible, it cannot be extrapolated, because the second peak is hardly recognizable.

a)

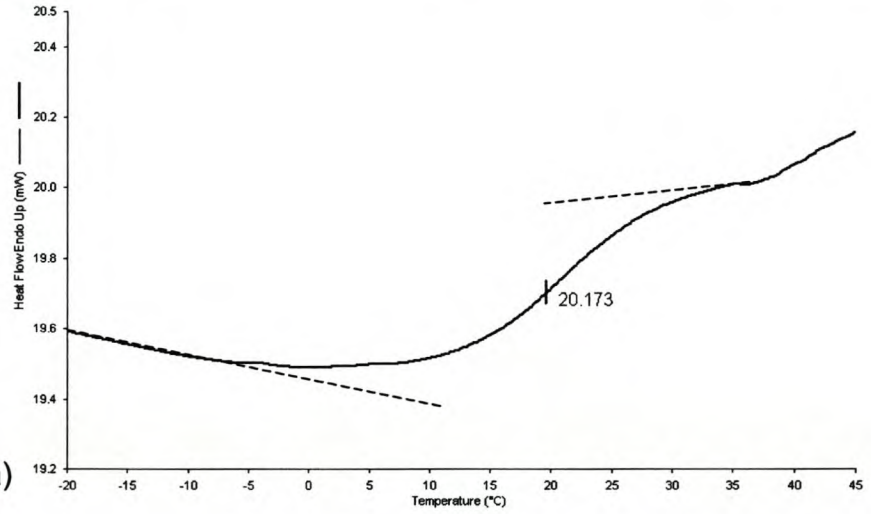

b)

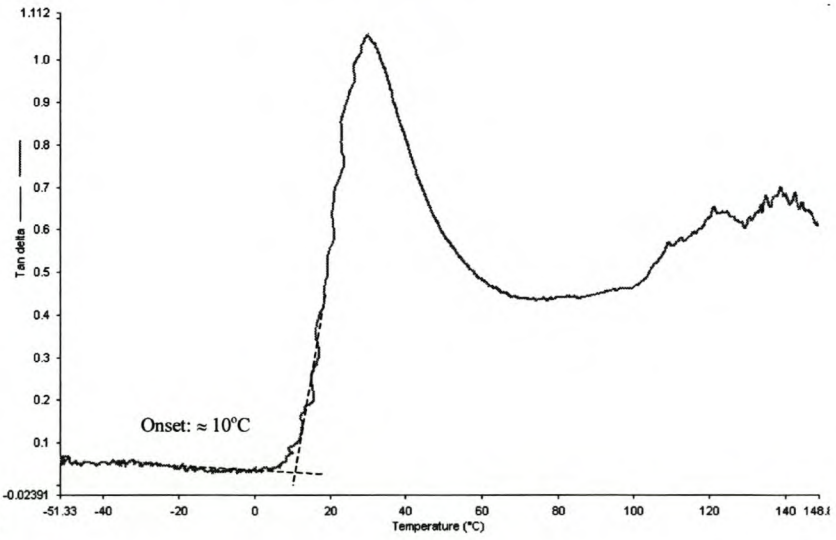

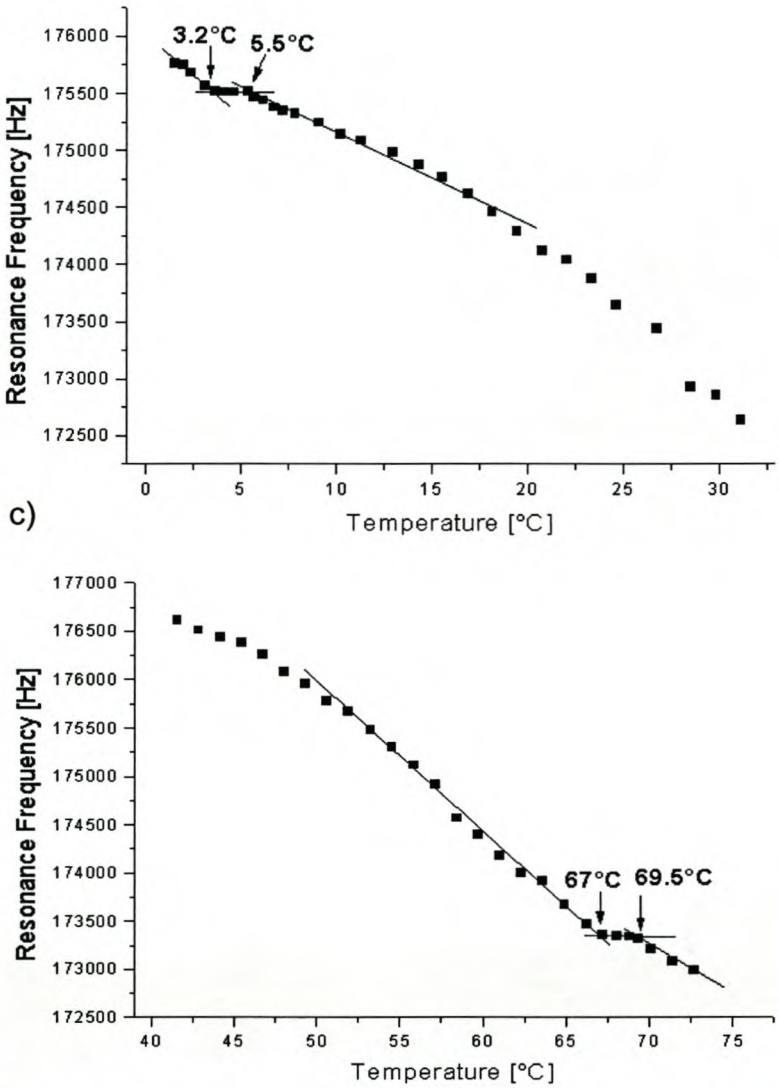

Figure 6.7: Glass transitions of the crosslinked core-shell latex CS12 with a high T_g core and a low T_g shell, measured by DSC (a), DMA (b) and RFM (c).

The frequency curve obtained by AFM shows a plateau between 3.2°C and 5.5°C and one between 67°C and 70°C (Figure 6.7b). Again the temperature ranges are in separate graphs to emphasize the plateau region. Both observed T_g values corresponding well to the predicted glass transition temperatures of the core and shell phases of the polymer as calculated with the Fox equation from synthesis data.

Furthermore, the thermal transitions of a gradient polymer were measured. This core-shell polymer has a crosslinked core and a shell consisting of a copolymer, which contents are gradually changing from the inner side to the outside. Around the core the copolymer consists of 100% PS, gradually decreasing towards the outside. At the outside the polymer consists of 100% BA gradually decreasing towards the inside. For the exact composition see Chapter 4.2.

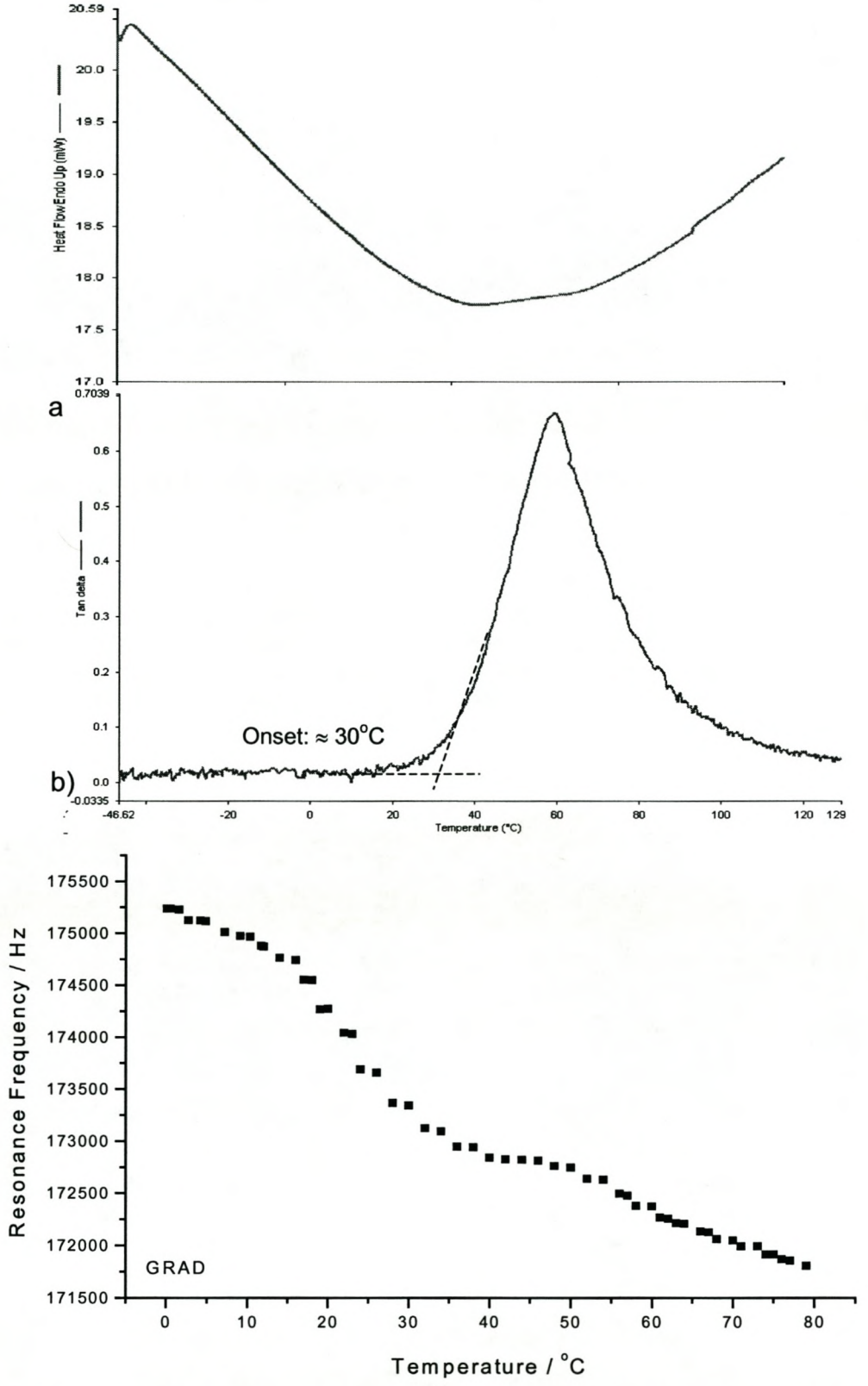

Figure 6.8: Glass transitions of a gradient latex with a crosslinked core and a gradient shell, measured by DSC (a), DMA (b) and RFM (c).

BA has a T_g of –55°C, Styrene has a T_g of about 100°C. The pure BA at the outer side of the particle can already flow and filmform at room temperature. The phase consisting of BA and PS has a higher T_g, increasing with the amount of PS.

The DSC curve shows no thermal transition at all (Figure 6.8a). The DMA curve (Figure 6.8b) shows one glass transition temperature at about 30°C. This result is not reasonable, since due to the gradient structure, no single glass transition temperature exists for the investigated latex.
The RFM curve (Figure 6.8c) however, shows plenty of little steps, or plateaus, indicating the "different", or rather gradually changing, T_gs of the shell polymer.

These results show that the AFM is not only sensitive to different polymer phases close to each other, but also to the polymer structure, which influences the glass transition temperature.
The ability to measure thermal parameters like the glass transition temperature locally is a valuable and useful method to determine, for example, if the polymer particles have the desired structure. If two different T_gs are determined for a core-shell polymer and their value is consistent with the theoretically predicted T_g this is a strong indication that the polymer has in fact a core-shell structure and exists not as a blended unstructured polymer.

6.4 Polyolefins

Other investigated polymer systems were polyolefins, which have several thermal transition temperatures, according to their structure. The investigation was focused on polyolefins with different side chain lengths. Polyolefins with long alkyl chains possess two melting points that are generally attributed to the melting of crystals formed by the side chains and the helical main chain [2]. According to Wunderlich [3] the long main chains form helices with the side chains twisting from the helical backbone. The side chains are packed in a paraffin-like manner.
According to Overberger et al. [4] and Jordan et al. [5], side chain crystallinity appears in such polymers usually when the side chains exceed a minimum of 10 to 12 carbon atoms, which would be polymers of dodecene and longer monomers.

However, two melting points are observed for poly-1- pentene in the first DSC run (Figure 6.9a) During the second heating cycle the sample shows no melting points at all, which indicates that the initial crystalline structure was destroyed during the first heating cycle.
Resonance frequency measurements with the AFM show also two transitions for poly-1-pentene, as displayed in Figure 6.9b. Henschke et al. [2] attribute the two melting points of poly-1-pentene to different crystal modifications.

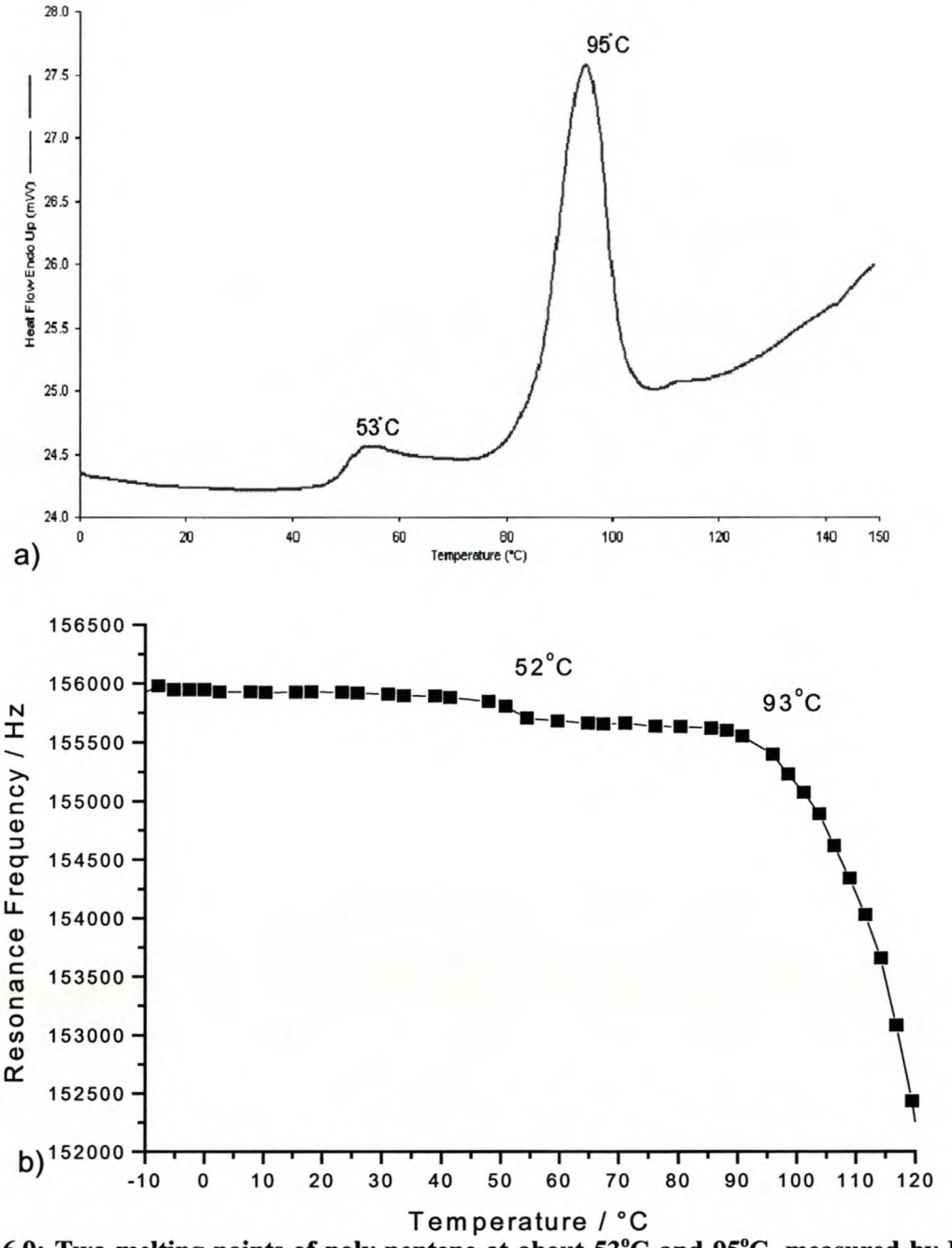

Figure 6.9: Two melting points of poly-pentene at about 53°C and 95°C, measured by DSC (a) and RFM (b).

In the case of poly-1-tetradecene with side chains of 12 carbon atoms two thermal transitions can be observed by DSC and AFM. The DSC curve (Figure 6.10a) shows a sharp peak at about 14°C and a wider peak at about 54°C. The second peak consists actually of three superpositioned peaks, with smaller humps at about 42°C and 57°C.

Like the DSC, the AFM resonance frequency curve (Figure 6.10b) shows two major transitions at about 12°C and 50°C, of which the transition at 12°C is the more pronounced. Smaller kinks are observed at about 40°C and 55°C.

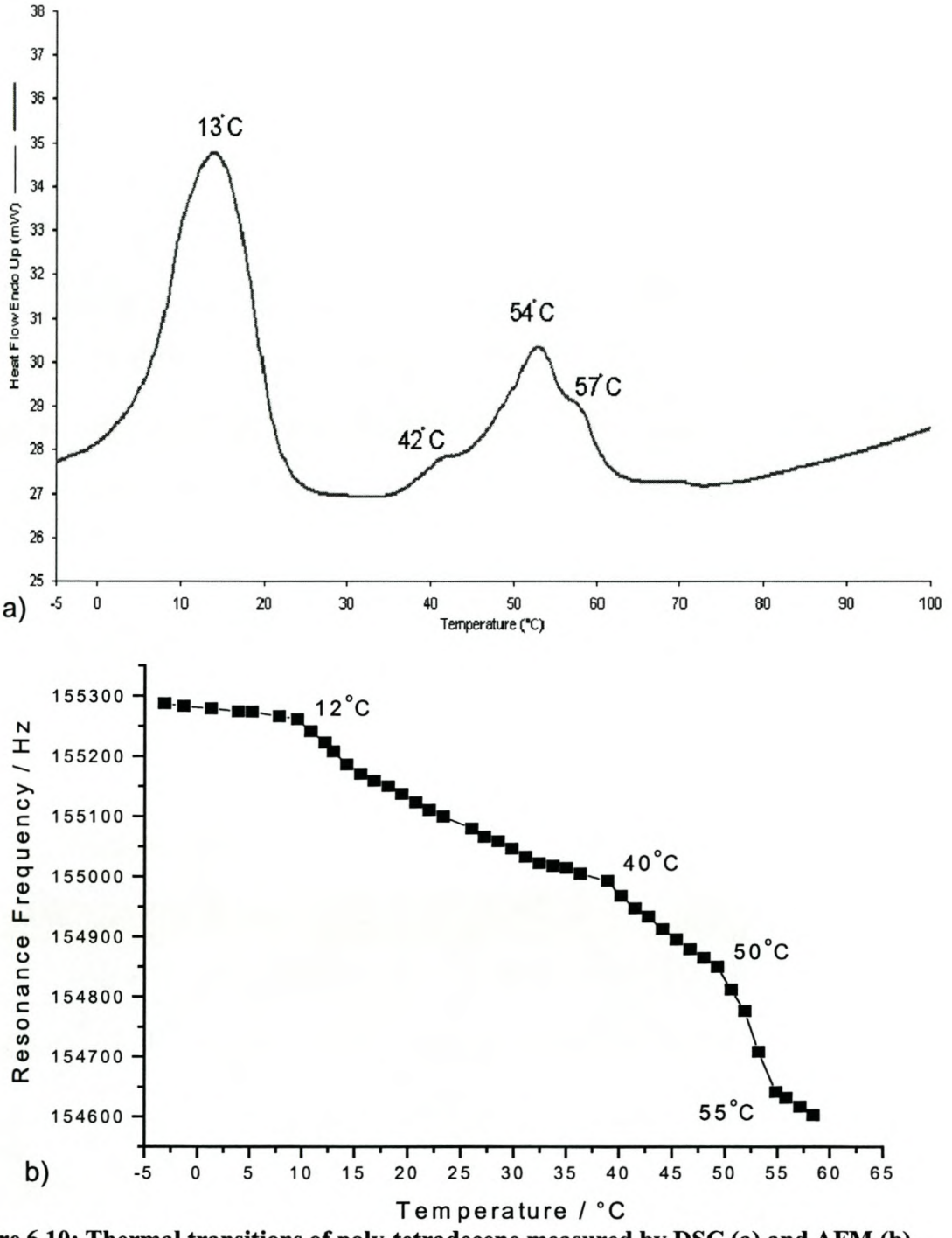

Figure 6.10: Thermal transitions of poly-tetradecene measured by DSC (a) and AFM (b).

Unlike in the DSC curve, melting points in the RFM method are represented by kinks, which makes it easier to differentiate between transitions in a close temperature range. The peaks in the DSC curve can be easily superposed and thus be regarded as only one peak.

The thermal transitions of poly-1-tetradecene can now be attributed to the main- and side-chain crystallization.

Henschke et al. assigned the less pronounced melting point to the main-chain crystallinity and claimed that the side-chain crystallinity is more dominant. Wunderlich [3] also attributes the higher crystallinity to the side chains, which are packed in a paraffin-like manner.
From the DSC curve in Figure 6.10a it is difficult to obtain information, which peak could should be assigned to which transition, especially since the peaks are nearly of the same height.
The AFM measurements, however, give an indication, which transition is related to the main-chain crystallization and which to the side-chain crystallization. Since the cantilever measures the molecular response to excitation locally, it should be more sensitive to the side-chain transition than the melting of the main-chain.
Thus it can be assumed that the transition represented by the sharper kink correlates to the side-chain melting. In this case the side-chain melting can be assigned to the low temperature transition at about 12°C, in good agreement to Henschke's findings.

Poly-1-octadecene has 16 carbon atoms in the side chain side-chains with the length of 16 carbon atoms. Again main- and side-chains form two different crystalline structures with different melting points. Figure 6.11 displays the DSC (a) and AFM (b) results.

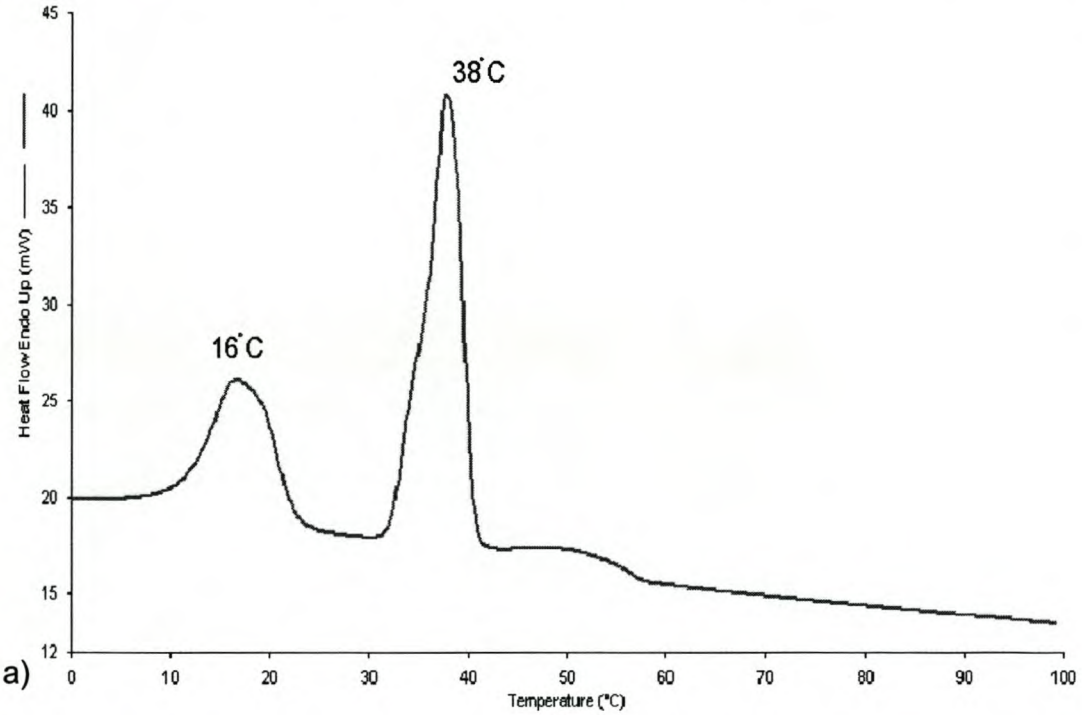

a)

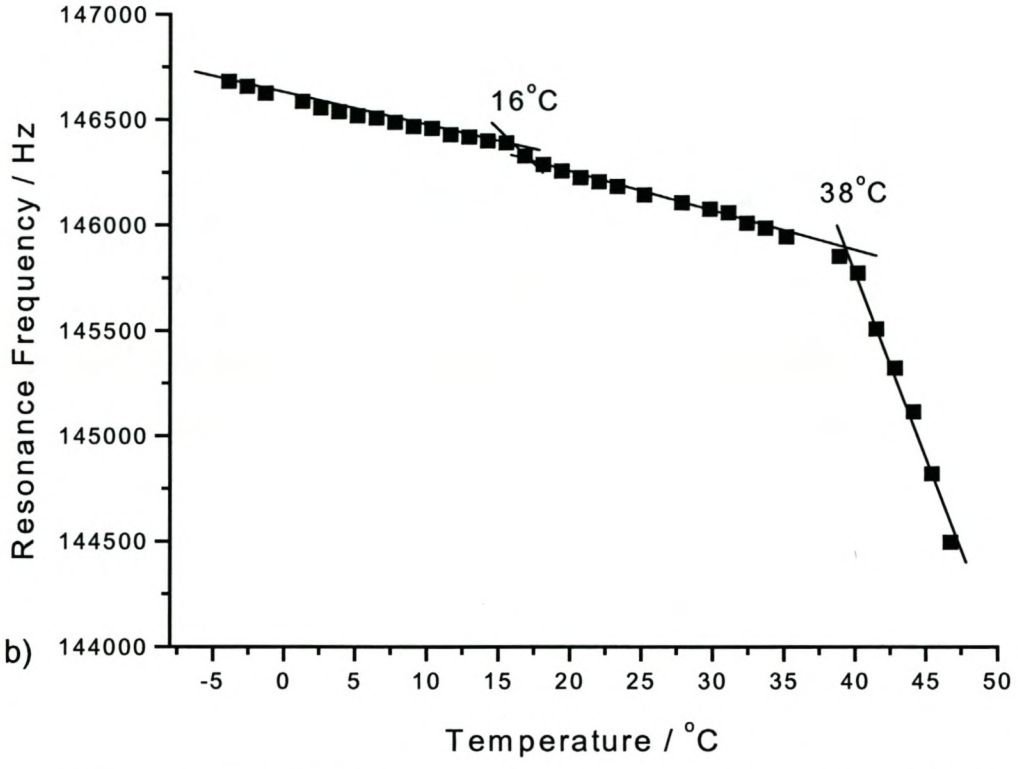

Figure 6.11: Thermal transitions of Poly-octadecene measured by DSC (a) and AFM (b).

The DSC curve shows a peak at about 16°C and a higher temperature peak at 38°C. According to Henschke the more prominent peak should be assigned to the side-chain melting, which would be the high temperature peak at 38°C.This can be confirmed by the RFM result, which shows a transition at about 16°C and a more distinct kink at 38°C.

6.5 Glass Transition of Thin Polystyrene Films

To investigate the sensitivity of the new technique towards molecular weight and film thickness of the sample, polystyrene films of different thickness and molecular weight were investigated.
The films consisted of polystyrene with a molecular weight of 22000 g/mol, 142500 g/mol and 868800 g/mol and the film thickness ranged from 120Å to 1500Å

6.5.1 Different Film Thickness

The width of the plateau in the resonance frequency plot representing the glass transition of a polymer seems to vary with the film thickness of the polymer film.

From the experimental results obtained by AFM can be seen that the plateau width increases with increasing film thickness, as displayed in Figure 6.12. Furthermore the temperature at which the plateau starts increases with increasing film thickness.

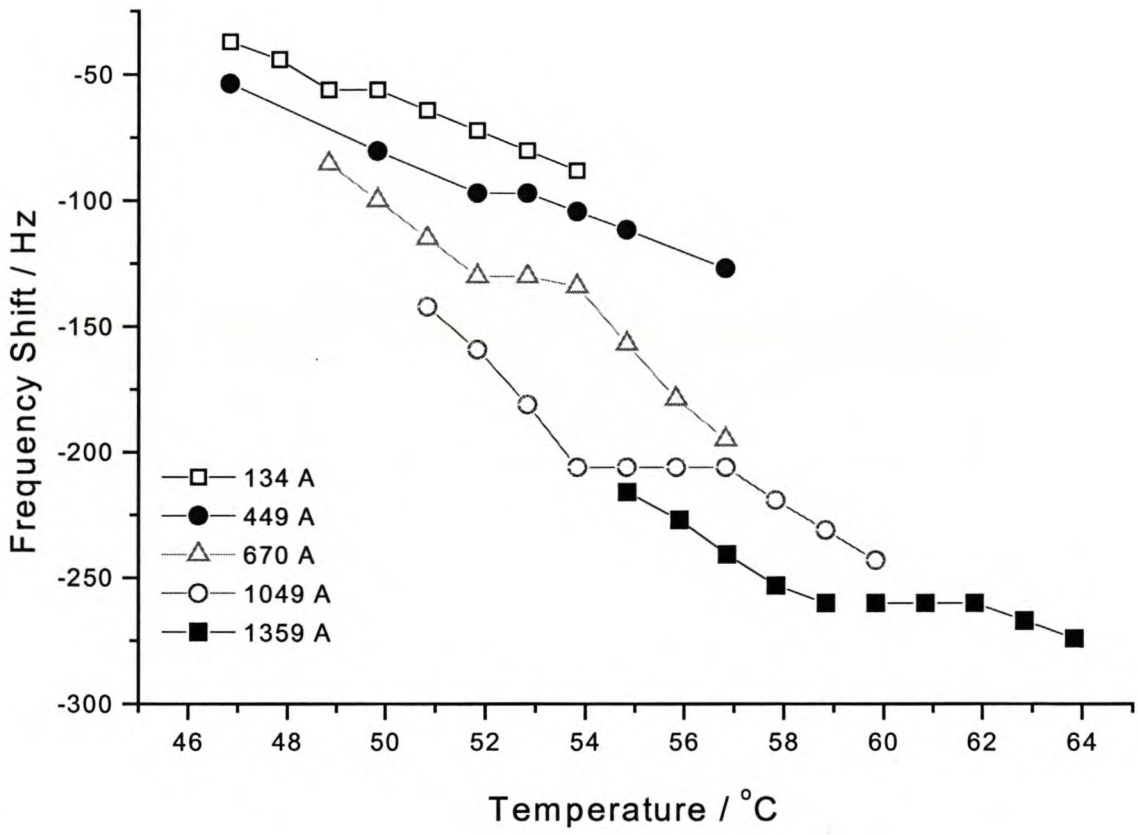

Figure 6.12: Glass transition temperatures obtained by RFM for polystyrene films of different thickness.

The investigated samples had a molecular weight of 142500 g/mol and a film thickness of 134Å (hollow square), 449Å (black circle), 670Å (hollow up-triangle),

1049Å (hollow circle) and 1359Å (black square). The curves were arbitrarily shifted on the y-scale to enable better comparison.

Figure 6.13 shows the plateau width plotted as a function of the film thickness. It becomes visible that the plateau width is increasing with increasing film thickness until it reaches a maximum value at which it levels out. In this case the maximum value is about one micrometer.

A possible explanation for the increasing plateau width is that the AFM resonance frequency method shows a certain depth sensitivity. The oscillating cantilever creates a pressure wave that is reflected at the surface and thus influences the cantilever, as described in chapter 3. At the glass transition the reflection coefficient starts to decrease and the absorption coefficient is increasing. This means the polymer is now able to absorb energy from the pressure wave and convert it into kinetic energy for chain motion. Obviously the energy will be absorbed first from the surface layer of the polymer, and chain segments can start to move.

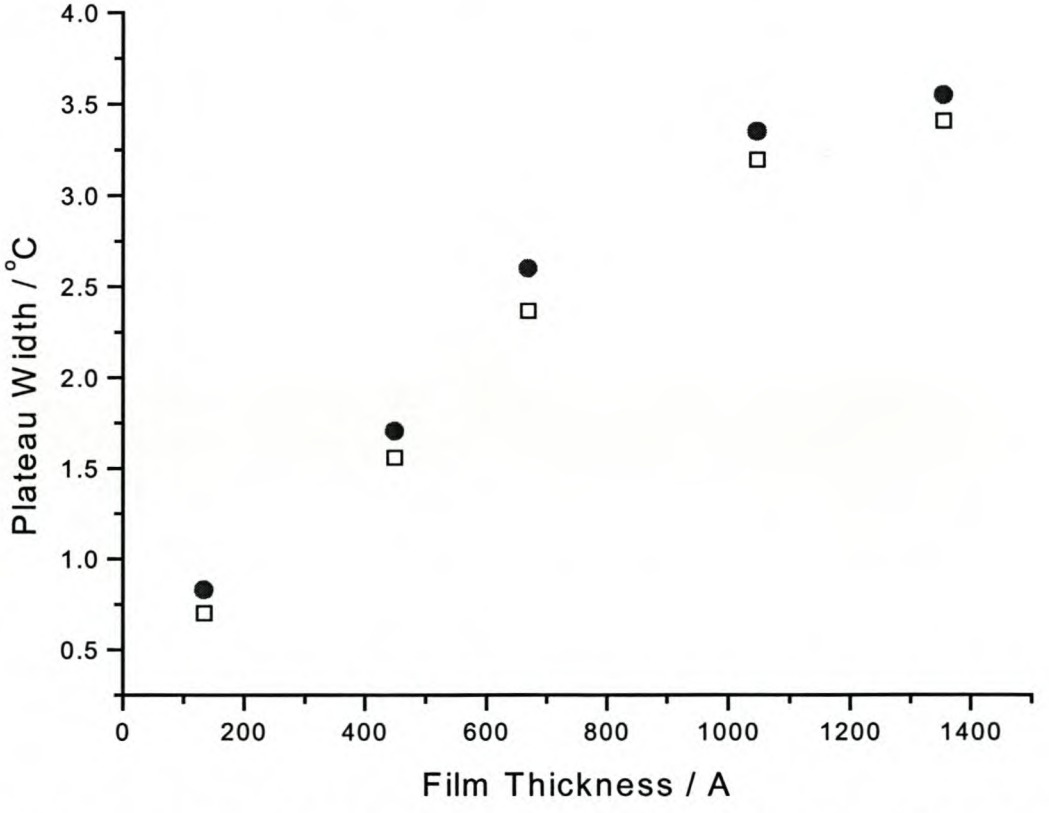

Figure 6.13: The plateau width of the RFM method as a function of the film thickness of the polystyrene film. The different symbols represent different measurements.

With increasing temperature the pressure wave "reaches" underlying layers of the polymer, which can now absorb energy as well, which leads to a further increase of the absorption coefficient and results in the resonance frequency plateau representing the glass transition of a polymer. The maximum penetration depth of the pressure wave generated by the oscillating cantilever is given by the value at which

the plateau width reaches its maximum value and levels into a constant plateau. Here the maximum penetration depth is about one micrometer.

Figure 6.14 shows that the temperature at which the glass transition starts is also a function of the film thickness of the polymer. The glass transition temperature is increasing with increasing film thickness.

The glass transition temperature, or rather the onset of the glass transition, is a linearly increasing function of the film thickness of the polymer. It can be assumed that, at a certain film thickness, larger than the investigated samples, the glass transition temperature reaches the bulk value of polystyrene of about 100°C and doesn't increase further, according to the theoretical model described by Forrest et al. [6]. Unlike the results obtained by Forrest et al. the threshold value h_0 of the film-thickness at which the bulk T_g is reached is at a film thickness larger than 1200 Å.

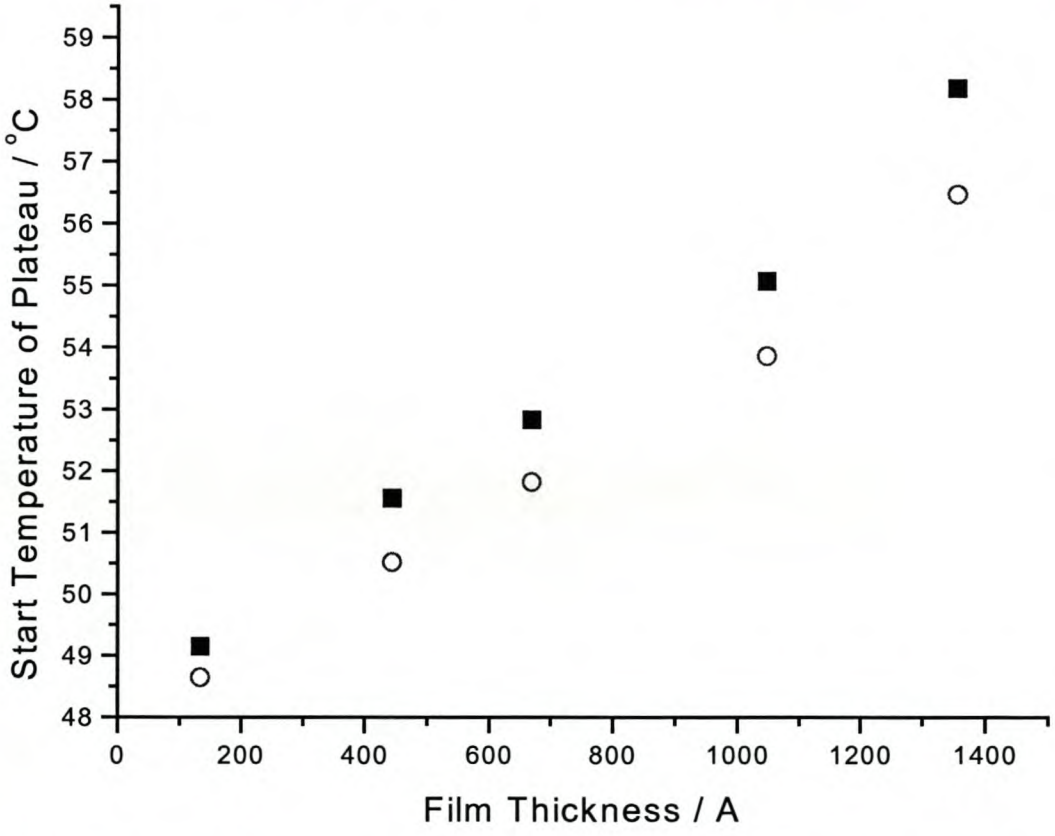

Figure 6.14: Glass transition temperature of polystyrene films with different thickness as a function of the temperature. Different symbols represent different measurements.

The fact that the values of the two different measurements are not exactly the same shows that the absolute temperature measurement of the experimental setup is not perfectly accurate. The temperature change during a measurement (for example heating to a temperature 2 degree higher than the start temperature) can be believed to be exact but the absolute temperature can only be determined within the range of a few degree.

6.5.2 Different Molecular Weights

The molecular weight is known to influence the glass transition temperature as well. T_g is decreasing with decreasing molecular weight, according to: $T_g = T_g^{(bulk)} - k/M_W$ With the material constant k. For polystyrene is $k=2x10^5$ and $T_g^{(bulk)} \approx 100°C$. The expected reduction of the bulk T_g as a function of the molecular weight is displayed in Figure 6.15:

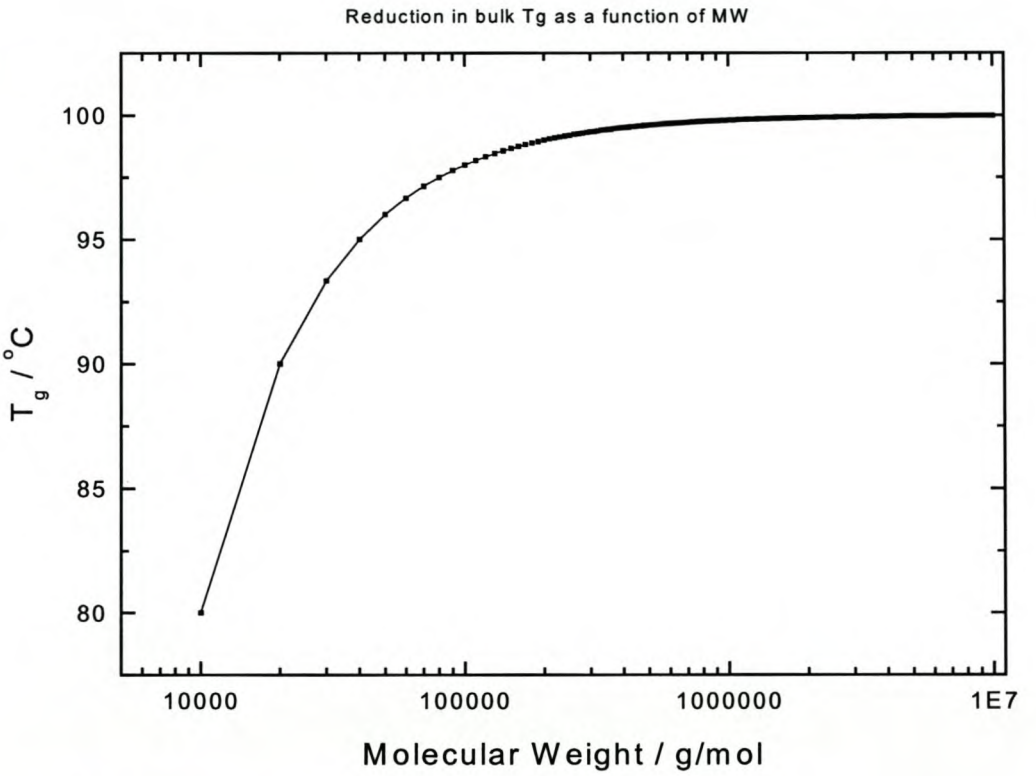

Figure 6.15: Reduction of the bulk T_g as a function of molecular weight.

The T_g of the investigated polystyrene films is reduced due to two effects: a decreasing molecular weight and the fact that they are applied as ultra-thin films with a thickness of only 450Å. As mentioned before (Figure 6.14) the film thickness influences the glass transition temperature drastically.

Three polystyrene films with a film thickness of 450Å and a molecular weight of 22000 g/mol, 142500 g/mol and 868800 g/mol have been investigated. Due to the ultra-thin film the T_g is represented by a kink rather than a plateau, as displayed in Figure 6.16:

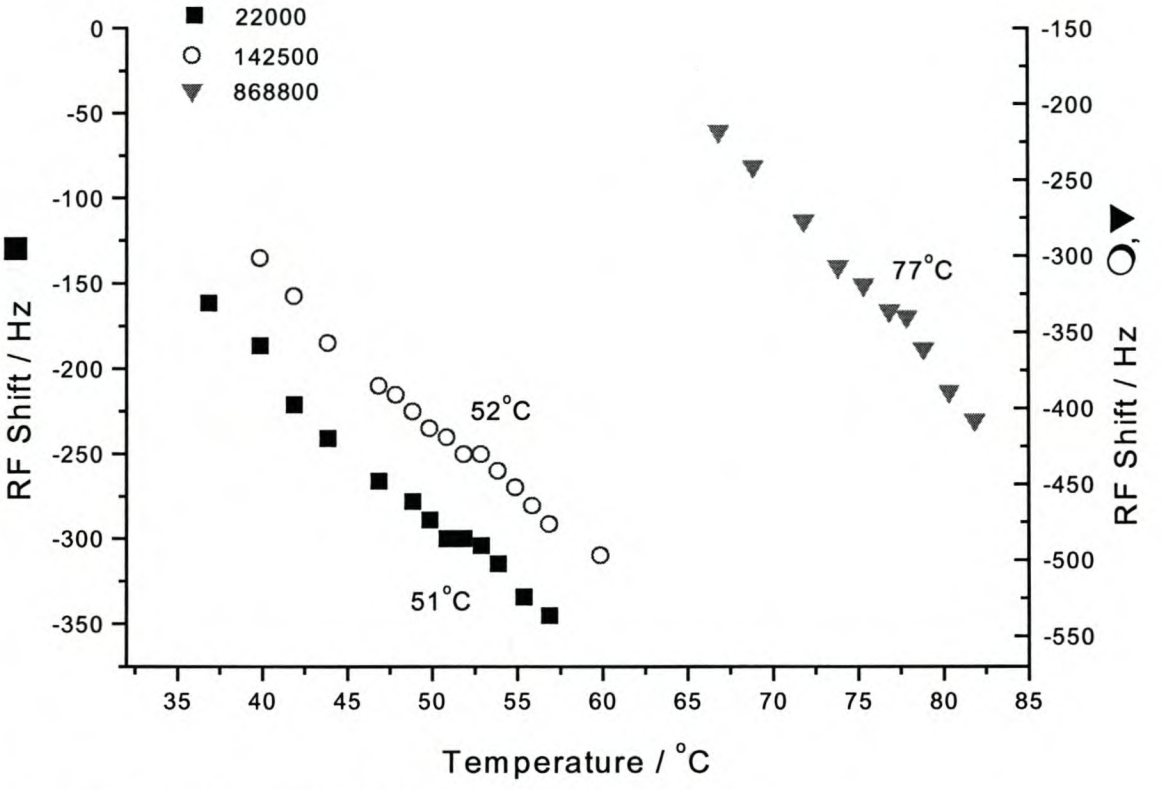

Figure 6.16: T_g reduction of thin PS film with molecular weight.

The glass transition temperature plotted as a function of molecular weight for polystyrene films of different film thickness is displayed in Figure 6.17. The T_g is lowered to about half of the bulk value, which is a considerable temperature reduction. This decrease in T_g is mostly due to the film thickness, but a general trend of changing T_g with molecular weight can be observed as well.

An interesting finding is, that the T_g value reaches a plateau towards lower molecular weight, which is not expected according to the theoretical model shown in Figure 6.15. This "minimum" glass transition temperature for the sample with a film thickness of 450 A is about 50°C. The results were reproducible. For the PS film with a thickness of 190A this minimum temperature is about 42°C and for the thickest film of 1000A the glass transition temperature seems to reach a limit between 50°C and 60°C.

This effect can be addressed to the influence of the film thickness on T_g. As displayed in Figure 6.14, the T_g of a film with the thickness of 450Å is about 50°C.

Towards higher temperatures the T_g is expected to level out to the bulk value of T_g of polystyrene, which is about 100°C, so the measurement points would follow a Boltzmann curve with a "s" shape.

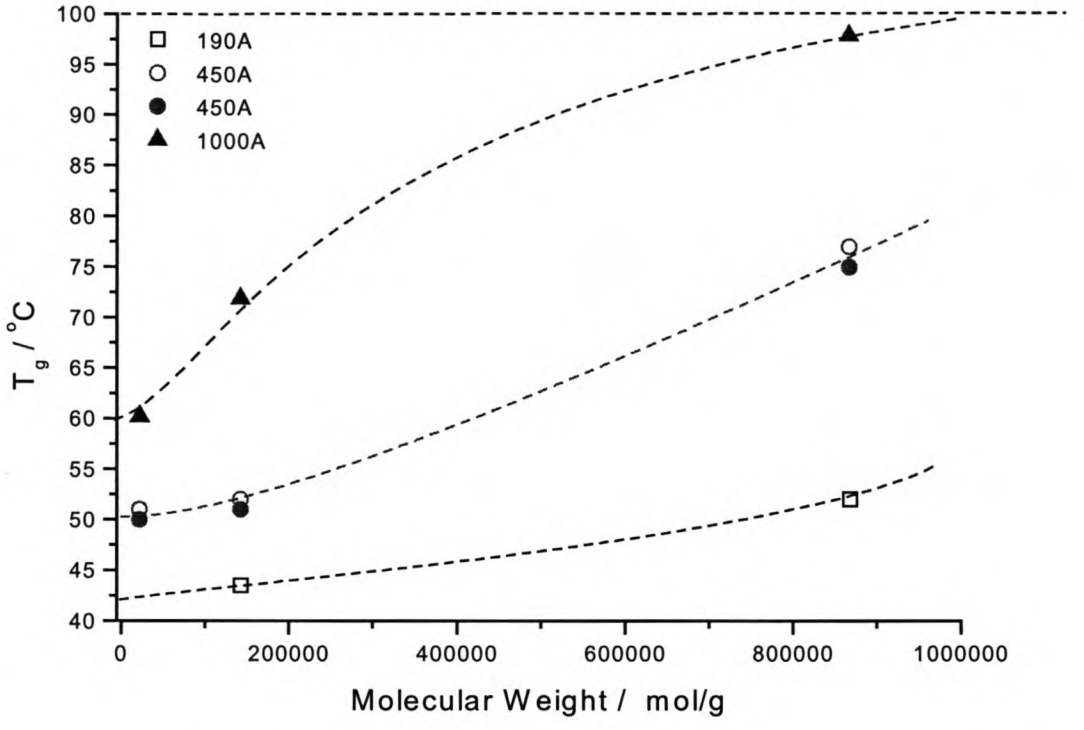

Figure 6.17: Reduction of T_g with molecular weight for polystyrene films of different film thickness measured by RFM.

6.6 Layered Systems

The depth sensitivity of the resonance frequency method has been confirmed by the investigation of layered polymer systems. Two thin polymer films were cast onto each other and the glass transition temperature(s) determined by AFM. The film thickness could unfortunately not be determined exactly. The sample was prepared in such a way, that the second film, or the upper layer, was as thin as possible.
The lower layer is the unstructured polymer UL1 with a T_g of about 24°C. The upper layer is a thin film of the polymer UL2 with a T_g of about 15°C.
The resonance frequency measurement does in fact determine both glass transition temperatures, as displayed in Figure 6.18. Different symbols represent different measurements.

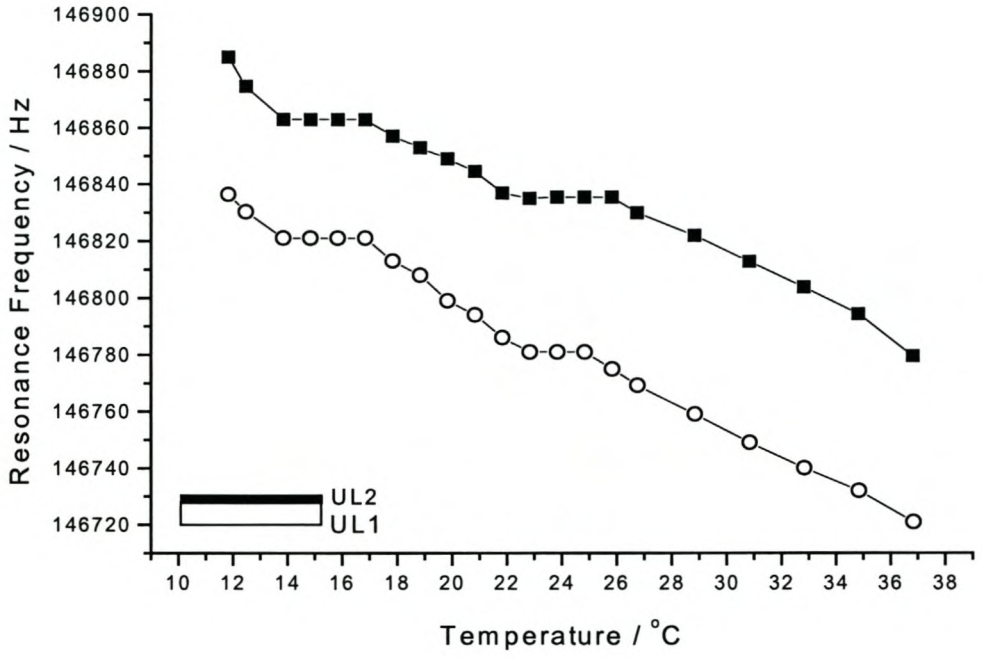

Figure 6.18: Glass transition temperatures of a layered system with the two polymers UL1 and UL2.

To confirm these measurements the polymer phases were switched around, with a lower layer of the polymer UL2 and a thin film of UL1 on top. Again the RFM determines both glass transition temperatures, as displayed in Figure 6.19 and the results are reproducible.

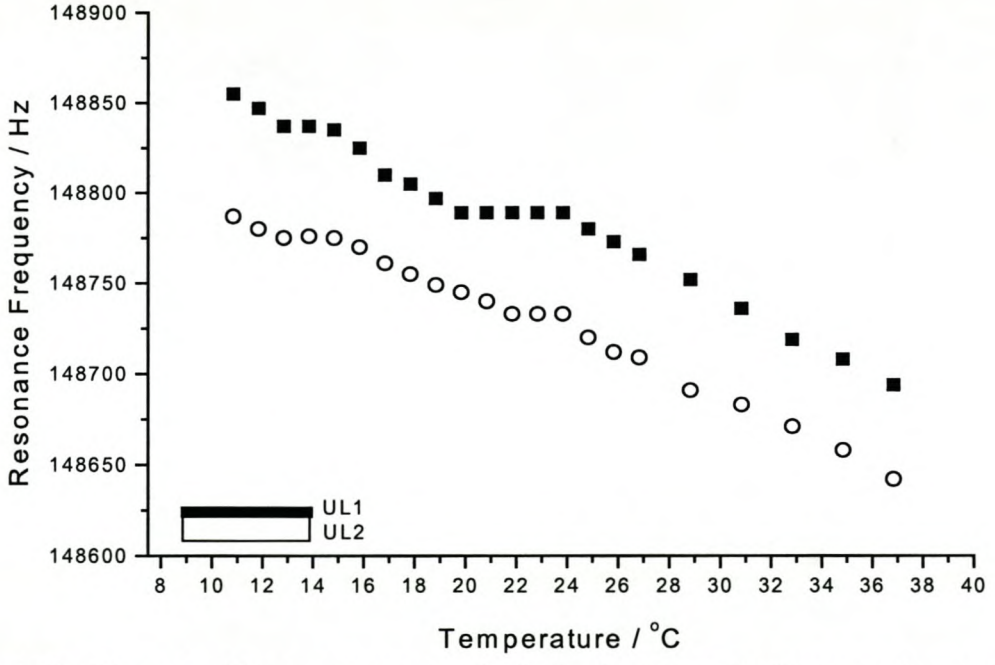

Figure 6.19: Glass transition temperatures of a layered system with the two polymers UL1 and UL2.

6.7 Lateral Resolution

With the current experimental setup it was not possible to move the tip a few nanometer and record another frequency spectrum. The sample holder and the heating stage had to be moved manually to measure at a different point on the sample. This restricted the minimum distance between two data points to several μm.

Figure 6.20 shows different frequency curves acquired at different positions on the sample surface. The sample consists of two different polymer films cast next to each other. The latices were UL3 with a theoretical T_g of 12°C and UL1 with a theoretical T_g of 23°C. Resonance frequency curves were measured at different positions around the polymer interface. This was done in order to compare the results of different positions on the surface and to determine the influence of the neighboring polymer. As mentioned before, the lateral resolution for this measurement is not very good, because the translation of the sample was performed manually.
To determine the position on the sample at which a frequency curve was acquired, an AFM image was scanned with a scan range of 60μm. The start and the end points of the tip movement as seen on the video screen of the Topometrix system determined the origin (0μm) and the 60μm position. A frequency curve was recorded at 0μm and then, by manually shifting as little as possible, roughly every 20μm (a third of the scan range, determined on the video screen).

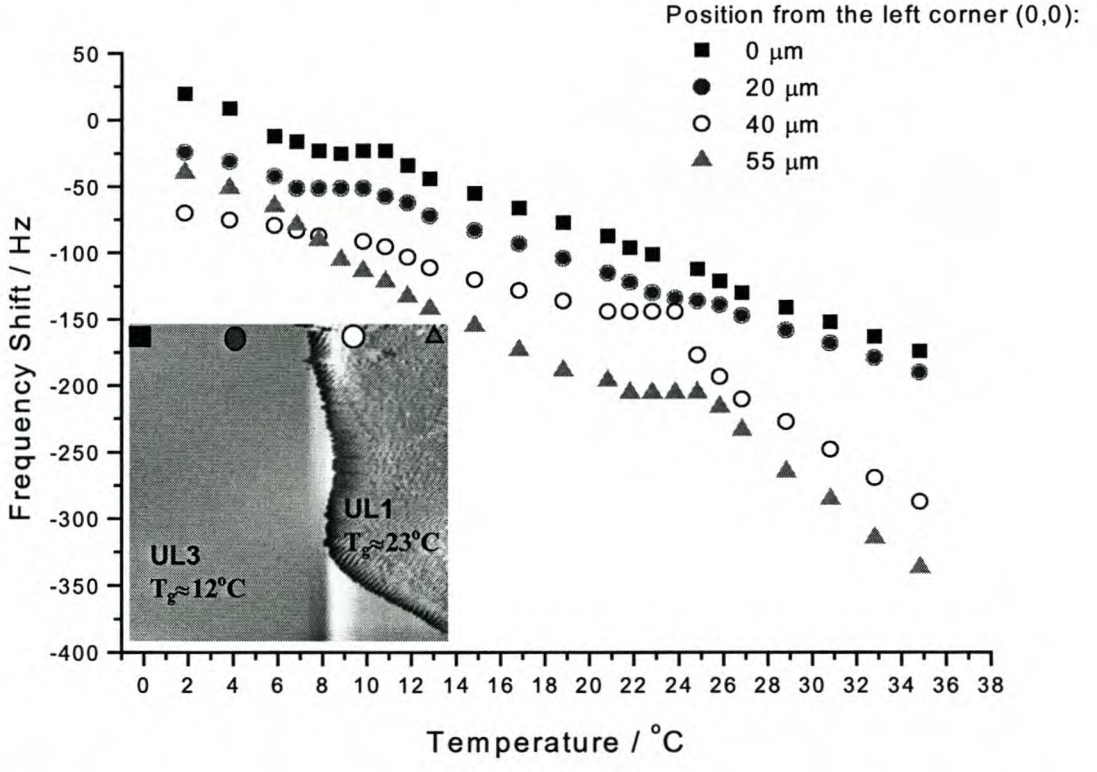

Figure 6.20: Resonance frequency curves at different positions close to the interface of the latices UL3 and UL1. The AFM image shows the different polymers and the measurement positions.

The AFM image in Figure 6.20 shows the polymer interface and the different positions at which data was acquired. The latex UL3 is on the left side and UL1 on the right side.
The two curves at 0 μm (black square) and 20 μm (black circle) show plateaus at around 10°C, which corresponds well with the T_g of UL3. The curves show at 40 μm (hollow circle) and 55 μm (black triangle) have plateaus at around 23°C, which corresponds well to the T_g of UL1. The curve at 40 μm is about 5μm away from the polymer interface and the T_g of UL3 cannot be seen in the curve. Hence the lateral resolution of this technique is definitely in the μm range.

Further developments in the control electronics will allow the implementation of the frequency measurement in the scanning process and the acquisition of datapoints only a few nm apart. This will enable us to determine the real lateral resolution of this technique.

6.8 Bibliography

[1] Provost,E., Balesdent,D., Bououkba,M., Petitjean,D., Dirand,M., *Journal of Chemistry Thermodynamics*, 1999, **31**, 1135
[2] Henschke,O., Knorr,J., Arnold,M., *Macromolecular Science, Applied Chemistry*, 1998, **A35**, 473
[3] Wunderlich,B., *Academic Press, New York*, 1980, chapter 10.3.4, 325
[4] Overberger et al., *Journal of the American Chemical Society*, 1953, **75**, 3326
[5] Jordan et al., *Journal of Applied Polymer Science*, 1969, **13**, 1777
[6] Forrest,J., Dalnoki-Veress,K., Stevens,J., Dutcher,J., *Physical Review Letters*, 1996, **77**, 2002

CHAPTER 7: Conclusions

Results of the investigations proved the AFM to be a powerful and versatile tool for the characterization of polymers close to the surface and a few layers below.

In the imaging mode the AFM was used to monitor the drying and film-formation process of different latices. Different polymer structures, core-shell polymers with different core/shell ratios and latices with different particle size were investigated.
The results, although empirical, yielded information on which polymer structure was the most suitable for a certain required film-formation behavior. Core-shell particles with a hard, high T_g core, surrounded by a soft, low T_g shell, had the best film-forming properties at ambient conditions. The optimum core/shell ratio was found to be 2/5 or smaller, and the particle size of the latex particles should be as small as possible, since the film formation behavior improved with decreasing particle diameter.

Furthermore, studies on the influence of different coalescent solvents and rheology modifiers on the film-formation behavior revealed that these solvents influenced the characteristic evaporation of interstitial water and the hardness of the film rather than on the polymer flow and particle deformation. The rheology modifiers changed the flow properties of the latex system and the topology of the polymer. A conventional thickener, for example, was found to coagulate into separate phases around the latex particles, instead of forming a three-dimensional network with the latex particles.

Additional information on the film-formation kinetics was acquired by ultrasonic shear wave (USSW) measurements and these confirmed the findings of the AFM measurements. The USSW measurements yielded information about the water evaporation from the emulsion and the hardness of the dry film, and thus completed a comprehensive description of kinetic processes taking place during film formation.

Thermal properties of the polymer surface, for example the heat conductivity of different polymer phases, were determined by SThM images. Due to the large tip diameter of the thermal tip and the low lateral resolution, only large particles with a diameter of about 320nm could be imaged.

To detect thermal parameters of a polymer locally, the AFM was used in a probing mode. The cantilever oscillated above the surface and its resonance frequency was determined as a function of increasing temperature. Thermal transitions of the polymer caused a change in the characteristic resonance frequency curve. This could be attributed to the melting points and glass transitions of the investigated polymers. Due to the local measurement, the AFM was able to determine thermal transitions of different polymer phases close by. Since the determination of the mechanical response of a polymer functions similarly to the DMA it was called "NanoDMA".
The NanoDMA could determine glass transition temperatures of core-shell polymers, for example, for the core and the shell phase individually.

The influence of the film thickness and molecular weight of the polymer samples on the glass transition temperature was also investigated.
The glass transition temperatures of thin polystyrene films with different molecular weight and film thicknesses, in the Angstrom region, were compared. The resonance frequency measurements showed a clear dependency of T_g on molecular weight and film thickness.

It was observed that the new measurement method developed in this research has a certain depth sensitivity and can determine thermal transitions of underlying layers as well as the surface T_g.
The measurements gave strong evidence that the T_g at the surface of a polymeric film is lower than its bulk T_g.

Recommendations

The film-formation studies could be continued with different polymer structures and polymers containing different additives, as used in the paint industry to enhance the film-formation properties of a latex.

The SThM work should be continued with newly developed thermal tips that are shaped like normal AFM tips but have a tip diameter of only a few nanometers. These tips are currently being developed in Wuppertal, Germany and in Loughborough, England. With these new tips it should be possible to determine the heat capacity of different polymer phases close by and image them simultaneously with the topography.

In order to use the AFM as a "NanoDMA" new, separate control electronics and software was developed by P. Lepidis, University of Wuppertal. The controller includes a frequency generator to oscillate the cantilever, a very precise Lock-In amplifier to detect the resonance frequency and the phase shift, and a temperature control. The resonance frequency and phase shift at any measured temperature are stored in a file and the frequency/phase plot is displayed graphically on the computer monitor.

First measurements were already carried out, to adjust experimental settings and parameters. With this new instrument it will be possible to automate the process to determine the resonance frequency and additionally the phase shift of the cantilever as a function of temperature, and directly feed it in a software program that displays the recorded data curves. The electronic devices are also faster and more sensitive than the components in the Topometrix setup used for experiments to date, thus the results should be more reliable than the results obtained by the present setup presented in this thesis.
The implementation of a scanning mechanism will allow for the determination of thermal transitions of different polymer phases in a two dimensional matrix across the sample surface. Experiments with this new technique could give information about

polymer blends or structured polymers by measuring their thermal transition temperatures locally.

Acknowledgements

I would first like to thank my promoter, Prof. Sanderson, for the opportunity to carry out this interesting PhD project in his group. He provided me with the opportunity to start a new research direction, in co-operation with the University of Wuppertal and to attend conferences and visit other research groups overseas.
My thanks also go to co-promoter Prof. Balk, and my colleagues P. Lepidis and G. Fiege, from the University of Wuppertal, Germany, who helped with the setup of new instruments, especially the SThM. P. Lepidis also constructed the new controller and the software for the "NanoDMA".
D. deWet-Roos and J.Engelbrecht from the Plascon Research Group, Stellenbosch, South Africa provided most of the polymer samples and supervised the research on film-formation.
The polystyrene films were prepared by J. Howse in Sheffield, England. The polyolefin samples were provided by R. Bruell and U. Wahner from the Institute for Polymer Science, Stellenbosch. They supported my PhD as good friends and encouraged my work with fruitful discussions.
I would also like to thank all my friends and colleagues at Polymer Science, who supported me throughout my PhD and helped with the writing of publications.

Funding for the project was provided by the National Research Foundation (NRF) of South Africa and the paint company Plascon, South Africa.

CHAPTER 8: Appendix

The C++ program to calculate the correlation function was written by Frank Eurich, Fakultaet fuer Physik Universitaet Konstanz, Lehrstuhl Dieterich (Statistische Physik)

```
#include <stdlib.h>
#include <stdio.h>
#include <math.h>
#include <fftw.h>

double *Sb; // Strukturfaktor S(kx,ky)
double *gb; // Korrelationsfunktion g(x,y)
double *Sr; // zirkulaer gemittelter Strukturfaktor S(kr)
double *gr; // zirkulaer gemittelte Korrelationsfunktion g(r)

double *kx;
double *ky;
double *kr;

const int Nx = 400;
const int Ny = 400;
const int N = Nx*Ny;

const double Lx = 1.0;
const double Ly = 1.0;

const double dx = Lx/double(Nx);
const double dy = Ly/double(Ny);

void Sg_new()
{
  Sb = new double[N];
  gb = new double[N];
  Sr = new double[(Nx/2)+1];
  gr = new double[(Nx/2)+1];

  kx = new double[Nx];
  ky = new double[Ny];
  kr = new double[Nx]; //
}
void delete_Sg()
{
  delete [] Sb;
  delete [] gb;
  delete [] Sr;
  delete [] gr;

  delete [] kx;
  delete [] ky;
  delete [] kr;

}
void init_k()
{
  const double Pi = 3.141592654;
  for (int i = 0; i < Nx; i++)
    {
      kx[i] = (2.0*Pi*double(i))/Lx;
      kr[i] = kx[i];
    }
  for (int j = 0; j < Ny; j++)
    {
      ky[j] = (2.0*Pi*double(j))/Ly;
    }
}
inline int idx( int x, int y ) {

  return y*Nx + x;

}
void gbulk_varN(double *g, double *S, fftwnd_plan plan){
```

```
  int i,j;

FFTW_COMPLEX fcf[Nx][Ny];

for (i = 0; i < Nx; i++){
      for (j = 0; j < Ny; j++){
         c_re(fcf[i][j]) = S[idx(i,j)];
         c_im(fcf[i][j]) = 0.0;
       }
    }

fftwnd(plan, 1, (FFTW_COMPLEX *) fcf, 1, 1, (FFTW_COMPLEX *) fcf, 1, 1);

for (i = 0; i < Nx; i++){
      for (j = 0; j < Ny; j++){
         g[idx(i,j)] = (fcf[i][j]).re/(double)(Nx*Ny);
       }
    }

}
void Sbulk_varN(double *spin, double *S, fftwnd_plan plan){
  int i,j;
  double sigmaquer;

FFTW_COMPLEX fcf[Nx][Ny];

sigmaquer = 0;
  for (i = 0; i < Nx; i++){
      for (j = 0; j < Ny; j++){
         sigmaquer = sigmaquer + spin[idx(i,j)];
       }
    }
  sigmaquer = sigmaquer/(double)(Nx*Ny);

for (i = 0; i < Nx; i++){
      for (j = 0; j < Ny; j++){
         c_re(fcf[i][j]) = spin[idx(i,j)] - sigmaquer;
         c_im(fcf[i][j]) = 0;
       }
    }

  // fuehre die FFT durch
  fftwnd(plan, 1, (FFTW_COMPLEX *) fcf, 1, 1, (FFTW_COMPLEX *) fcf, 1, 1);

  // Berechne den Strukturfaktor
  // S(kx,ky) = |fcf(kx,ky)|^2
  for (i = 0; i < Nx; i++){
      for (j = 0; j < Ny; j++){
                                                          S[idx(i,j)]                              =
(c_re(fcf[i][j])*c_re(fcf[i][j])+c_im(fcf[i][j])*c_im(fcf[i][j]))/(double)(Nx*Ny);
       }
    }

}
void zirk(double *S, double *Szirk )
{
  int i, j, n;
  int ischale, jschale;
  int norm[(Nx/2)+1]; // zaehlt die Zahl der Gitterpunkte in einer Schale

  for (i = 0; i < (Nx/2)+1; i++) {
      Szirk[i] = 0.0;
    }

  for (i = 0; i < (Nx/2)+1; i++) {
      norm[i] = 0;
    }

  for (i = 0; i < Nx; i++)
    {
      for (j = 0; j < Ny; j++)
       {
         // Berechnung in welcher "Schale" der Gitterpunkt liegt
         if (i < (Nx/2)+1)
           {ischale = i;}
         else
           {ischale = i-Nx;}
```

```
        if (j < (Ny/2)+1)
          {jschale = j;}
        else
          {jschale = j-Ny;}

        n = (int)ceil(sqrt((double)(ischale*ischale+jschale*jschale))-0.5);

        if (n < ((Nx/2)+1)) /* Beachte, dass Nx <= Ny sein sollte! */
          {
            norm[n] = norm[n]+1;
            Szirk[n] = Szirk[n] + S[idx(i,j)];
          }
      }
    }


for (i = 0; i < (Nx/2)+1; i++)
    {
      Szirk[i] = Szirk[i]/(double)norm[i];
    }

}
void eingabe(double hoehe[], char dateiname[200]) {

  double dhoehe;
  FILE *datei;
  char dstring[255];
  char dateiname_ext[300];

sprintf(dateiname_ext, "%s.txt", dateiname);
  datei = fopen(dateiname_ext, "r");

for (int i = 1; i<19; i++){
    fgets(dstring, sizeof(dstring), datei);
  }

  for (int i = 0; i < Ny; i++){
    for (int j = 0; j < Nx-1; j++){
      // je nach Format TAB oder SPC auslesen
      fscanf(datei, "%lf\t", &dhoehe);
      // fscanf(datei, "%lf ", &dhoehe);
      hoehe[idx(i,j)] = dhoehe;
    }
fscanf(datei,"%lf", &dhoehe);
    hoehe[idx(i,Nx-1)] = dhoehe;
    fscanf(datei, "\n");
  }

  fclose(datei);

} // eingabe

void Sr_ausgabe(double *Sr, double *kr, char dateiname[200])
{
  FILE *datei;
  char dateiname_ext[300];

sprintf(dateiname_ext, "%s.Sr", dateiname);
  datei = fopen(dateiname_ext, "w");

  for (int i = 0; i < (Nx/2)+1; i++){
    fprintf(datei, "%lf %lf \n",kr[i] ,Sr[i]);
  }

  fclose(datei);

}
void gr_ausgabe(double *gr, char dateiname[200])
{
  FILE *datei;
  char dateiname_ext[300];

sprintf(dateiname_ext, "%s.gr", dateiname);
  datei = fopen(dateiname_ext, "w");

  for (int i = 0; i < (Nx/2)+1; i++){
    fprintf(datei, "%lf %lf \n", dx*double(i), gr[i]);
```

```
  }

  fclose(datei);

}
void Sb_ausgabe(double *Sb, double *kx, double *ky, char dateiname[200])
{
  FILE *datei;
  char dateiname_ext[300];

sprintf(dateiname_ext, "%s.Sb", dateiname);
  datei = fopen(dateiname_ext, "w");

  for (int i = 0; i < Nx; i++){
    for (int j = 0; j < Ny; j++){
      fprintf(datei, "%lf %lf %lf \n", kx[i], ky[j], Sb[idx(i,j)]);
    }
    fprintf(datei, "\n");
  }

  fclose(datei);

}
void gb_ausgabe(double *gb, char dateiname[200])
{
  FILE *datei;
  char dateiname_ext[300];

sprintf(dateiname_ext, "%s.gb", dateiname);
  datei = fopen(dateiname_ext, "w");

  for (int i = 0; i < Nx; i++){
    for (int j = 0; j < Ny; j++){
      fprintf(datei, "%lf %lf %lf \n", dx*double(i), dy*double(j), gb[idx(i,j)]);
    }
    fprintf(datei, "\n");
  }
  fclose(datei);

}
void hoehen_ausgabe(double *hoehe, char dateiname[200])
{
  FILE *datei;
  char dateiname_ext[300];

sprintf(dateiname_ext, "%s.gnu", dateiname);

  datei = fopen(dateiname_ext, "w");

  for (int i = 0; i < Nx; i++){
    for (int j = 0; j < Ny; j++){
      fprintf(datei, "%lf %lf %lf \n", dx*double(i), dy*double(j), hoehe[idx(i,j)]);
    }
    fprintf(datei, "\n");
  }
  fclose(datei);
 }

int main(int argc, char* argv[])
{
char dateiname[200];

fftwnd_plan plan_trafo, plan_ruecktrafo;

double *hoehe;

  hoehe = new double[N];

  if (argc != 2) {
    printf("Syntax: auswertung <daten-file> \n");
    exit(1);
  }
    sprintf(dateiname, "./%s", argv[1]);

    Sg_new();

    init_k();
```

```
    plan_trafo = fftw2d_create_plan(Nx, Ny, FFTW_FORWARD, FFTW_MEASURE | FFTW_IN_PLACE);
  plan_ruecktrafo = fftw2d_create_plan(Nx, Ny, FFTW_BACKWARD, FFTW_MEASURE | FFTW_IN_PLACE);

    eingabe(hoehe, dateiname);

      Sbulk_varN(hoehe, Sb, plan_trafo);

    gbulk_varN(gb, Sb, plan_ruecktrafo);

    zirk(Sb, Sr);
  zirk(gb, gr);

  Sr_ausgabe(Sr, kr, dateiname);
  gr_ausgabe(gr, dateiname);
  Sb_ausgabe(Sb, kx, ky, dateiname);
  gb_ausgabe(gb, dateiname);

  delete_Sg();

  delete [] hoehe;

  fftwnd_destroy_plan(plan_trafo);
  fftwnd_destroy_plan(plan_ruecktrafo);
}
```